Zohre Eskandari Alughare

Gold Nanorods Functionalized with DNA Oligonucleotide Probes for Biosensing and Plasmon-Enhanced Fluorescence Detection

UNIVERSIDADE DO ALGARVE
FACULDADE DE CIÊNCIAS E TECNOLOGIA
2017

Zohre Eskandari Alughare

Gold Nanorods Functionalized with DNA Oligonucleotide Probes for Biosensing and Plasmon-Enhanced Fluorescence Detection

Erasmus Mundus MSc in Chemical Innovation and Regulation
Mestrado Erasmus Mundus em Inovação Química e Regulamentação

Trabalho efetuado sob a orientação de:

Work supervised by:

Professor Ana Rosa Garcia (Universidade do Algarve)

Dr. Pedro M. R. Paulo (Centro de Química Estrutural)

UNIVERSIDADE DO ALGARVE
FACULDADE DE CIÊNCIAS E TECNOLOGIA
2017

Zohre Eskandari Alughare

Declaration of Authorship

I declare that I am the author of this work, which is original. The work cites other authors and works, which are adequately referred in the text and are listed in the bibliography.

(Zohre Eskandari Alughare)

Zohre Eskandari Alughare

Gold Nanorods Functionalized with DNA Oligonucleotide Probes for Biosensing and Plasmon-Enhanced Fluorescence Detection

UNIVERSIDADE DO ALGARVE
Faculdade de Ciências e Tecnologia
2017

Título: Nano-bastonetes de Ouro Funcionalizados com Oligonucleotídos de ADN para Biosensores e Fluorescência Intensificada por Efeito Plasmónico

Resumo

Os nano-bastonetes de ouro são caracterizados por plasmões de superfície com frequências de ressonância bastante sensíveis ao índice de refração na proximidade da sua superfície. A funcionalização seletiva da superfície destas nanopartículas com bio-receptores é crucial para o desenvolvimento de sensores plasmónicos com resposta melhorada, pois permite a captura de analitos nas regiões mais sensíveis da nanopartícula. Em primeiro lugar foram preparadas superfícies com nano-bastonetes de ouro que depois foram funcionalizados com recetores biotina para ensaios modelo de deteção de estreptavidina. A funcionalização seletiva das extremidades dos nano-bastonetes foi conseguida através da proteção das suas paredes laterais com uma bicamada de tensioativo CTAB e usando uma biotina derivatizada com uma função tiól. O desempenho do sensor foi caracterizado por medidas da cinética de associação biotina-estreptavidina monitorizada por espectroscopia ótica de absorção. Em anos recentes, a infeção pelo vírus do Dengue DENV-2 tem sido relatada como a maior epidemia por este tipo de vírus, e a deteção precoce desta infeção poderia salvar a vida de muitos pacientes. Deste modo, foi desenhado um sensor plasmónico modelo para a deteção de sequências de ARN propostas como bio-marcadores para a infeção pelo vírus do Dengue. Para o efeito, foram funcionalizados nano-bastonetes de ouro com cadeias de oligonucleotídos de ADN complementares a uma sequência do ARN do vírus do Dengue. Como estratégia de amplificação de sinal foram usadas cadeias de oligonucleotídos alvo marcadas com biotina, de modo a ser possível num segundo passo ligar estreptavidina ou anticorpo anti-biotina com o objetivo de aumentar a resposta do plasmão de superfície dos nano-bastonetes de ouro.

A fluorescência intensificada por efeito plasmónico permite a deteção rápida e com elevado contraste de molécula única em microscopia de fluorescência. A interação entre os modos localizados de plasmão de superfície de nano-bastonetes de ouro e moléculas fluorescentes na sua proximidade pode induzir a aceleração das taxas de excitação, decaimento radiativo e não-radiativo, e conduzir a uma intensificação de fluorescência.Na terceira parte desta Dissertação, foram investigadas as interações entre nano-antenas de ouro e um cromóforo pouco fluorescente, a porfirina TMPyP. Esta interação foi mediada pela atração eletrostática entre a porfirina tetra-catiónica e o revestimento de ADN na superfície dos nano-bastonetes de ouro.

Ensaios preliminares de espectroscopia ótica foram realizados para caracterizar a interação em solução da TMPyP com sequências de ADN de cadeia simples ou duplacomplementares a uma sequência do ARN do vírus do Dengue. A constante aparente de equilíbrio para o complexo da TMPyP com as sequências de ADN de cadeia simples e dupla foram determinadas como sendo K_a= 3.9×10^7 $M^{-1}$and 4.5×10^7 M^{-1}, respetivamente. As alterações dos espectros de absorção e emissão mostram uma forte interação, provavelmente intercalação, daTMPyPcom ods-DNA,etambém com o ss-DNA, devido ao elevado conteúdo em pares GC nas sequências escolhidas. Em seguida, a fluorescência intensificada por efeito plasmónico na TMPyP induzida por nano-bastonetes de ouro foi investigada por microscopia confocal de tempos-de-vida, tendo sido realizadas medidas de intensidade e espectro de emissão de nanopartículas, espectroscopia de correlação de fluorescência, traços temporais de intensidade de emissão e de decaimento de fluorescência.Os nano-bastonetes de ouro foram imobilizados em vidro e funcionalizados com um revestimento de oligonucleotídostiolados, enquanto que as moléculas de TMPyP difundem-se em solução e podem interatuar estocasticamente com a superfície da nanopartícula. Os traços de intensidade de emissão medidos em nanopartículas individuais mostram picos de fluorescência intensos quando as moléculas de TMPyP se aproximam do nano-bastonete de ouro em resultado do efeito de nano-antena.Foram calculados os fatores de emissão intensificada por comparação com a emissão não-intensificada da TMPyP nas mesmas condições experimentais e obtiveram-se valores surpreendentemente elevados de cerca de 60000 vezes para a emissão intensificada da TMPyP. Estes fatores de intensificação são duas ordens de grandeza mais elevados do que as estimativas teóricas calculadas para a intensificação da emissão da TMPyP pelos nano-bastonetes de ouro.

Palavras Chave: Nanopartículas de ouro, biosensores plasmónicos, deteção de ácidos nucleícos, fluorescência intensificada por efeito plasmónico, fluorescência de molécula única, porfirinas

Title: Gold Nanorods Functionalized with DNA Oligonucleotide Probes for Biosensing and Plasmon-Enhanced Fluorescence Detection

Abstract

Gold nanorods display plasmon resonances that are very sensitive to the refraction index close to the particle's surface. The site-selective functionalization of Plasmon hot-spots with bioreceptors is crucial to develop plasmonic sensors with improved response bycapturing the target species at the most sensitive regions of the particle. Firstly, we used surface immobilized biotin-functionalized gold nanorods for streptavidin sensing.The selective functionalization of the nanorods' tips was achieved with a CTAB bilayer and using a thiol linker to attach the desired biotin functionality. The sensor performance was characterized by measuring binding kinetic assays. In the recent years, Dengue virus DENV-2 has been reported as the largest dengue epidemic type and early stage detection of this virus would save the life of many patients. Thus, a plasmonic model biosensor was designed for the detection of RNA sequences proposed as disease biomarkers for Dengue virus.For this purpose, we have functionalized gold nanorods with thiolated DNA oligonucleotide probes complementary to a RNA sequence of Dengue virus.As a signal amplification strategy, we have used biotin-labeled oligonucleotide target sequences, in order to bind streptavidin or anti-biotin antibody to increase the surface plasmon response.

Plasmon-enhanced fluorescence (PEF) microscopy provides fast, high-contrast, and low-background detection of single molecules. The interaction between the localized surface plasmon of gold nanorods and a fluorophore in their vicinity can induce the acceleration of excitation and decay rates thus leading to substantial fluorescence enhancements. In the third part of this Thesis, it was studied the interaction between gold nanorod antennas and a weakly fluorescence dye, TMPyP porphyrin. This interaction was mediated by electrostatic attraction between the tetracationic TMPyP and the DNA oligonucleotide coating on the nanorods' surface.

Preliminary measurements of optical spectroscopy were carried out to characterize the interaction in solution of TMPyP and single or double-stranded DNA oligonucleotides complementary to a RNA sequence of Dengue virus.The apparent equilibrium constants for the complex of TMPyP with single and double-stranded DNA were determined to be K_a= 3.9×10^7 $M^{-1}$and 4.5×10^7 M^{-1}respectively. The spectral changes show a strong specific intercalation of TMPyP with ds-DNA and ss-DNA because of GC-rich sites in the selected

sequences. Next, the plasmon-enhanced fluorescence of TMPyP induced by gold nanorods was investigated using confocal fluorescence lifetime microscopy to perform measurements of nanoparticle emission intensity and spectrum, fluorescence correlation spectroscopy, emission intensity time trace and fluorescence decay. The gold nanorods were immobilized on glass and functionalized with a thiolated oligonucleotide coating, while TMPyP molecules are diffusing in solution and stochastically interact with the rod's surface. The emission intensity traces measured on single particles show strong fluorescence bursts when TMPyP molecules come into close proximity of the nanorod. We have calculated the emission enhancement factors from a comparison with the non-enhanced emission of TMPyP in the same experimental conditions and found surprisingly large enhancement factors of around 60000-fold for TMPyP's emission.These values of enhancement are two orders of magnitude larger than our calculated highest enhanced fluorescence expected for TMPyP molecule.

Key Words: Gold nanoparticles, plasmonic biosensors, nucleic acid detection, plasmon-enhanced fluorescence, single-molecule fluorescence, porphyrins

Subject Index

Figure Index

Table Index

List of abbreviations and acronyms

A	Adenosine
AUT	11-Amino-1-Undecanethiol
C	Cytosine
CD	Circular Dichroism
CLSM	Confocal Laser Scanning Microscopy
CTAB	Cetyltrimethylammonium Bromide
DENV_2	Dengue Virus Typ II
DNA	Deoxyribonucleic acid
Ds-DNA	Double Strand Deoxyribonucleic acid
DDA	Discrete Dipole Approximation
FCS	Fluorescence correlation spectroscopy
FLIM	Fluorescence-Lifetime Imaging Microscopy
G	Guanine
GNPs	Gold Nanoparticles
GNSs	Gold Nanosphares
GNRs	Gold Nanorods
LEDs	Light-Emitting Diodes
LIF	Laser-induced fluorescence
LOD	Limit of Detection
LPB	Longitudinal Plasmon Band
LSPR	Localized Surface Plasmon Resonance
MNPs	Metal Nanometals
NSOM	Near-field scanning optical microscope
PBS	Phosphate-Buffered Saline
PEF	Plasmon-enhanced fluorescence
PEG	Polyethylene Glycol
PL	Photoluminescence
RNA	Ribonucleic acid
SA	Streptavidin
SEM	Scanning Electron Microscopy
SPR	Surface Plasmon Resonance
SMS	Single Molecule Microscopy

Ss-DNA	Single Strand Deoxyribonucleic acid
T	Thymine
TCSPC	Time-Correlated Single-Photon Counting
TEM	Transmission Electron Microscopy
$TMPyP^{4+}$	5,10,15,20-tetrakis(N-methylpyridinium-4-yl)-21H, 23H-porphyrin
TPB	Transverse Plasmon Band
TPPS	Tetraphenylporphyrin Sulfonate
Uv-Vis	UltraViolet-Visible

1. Introduction

Biosensors are being developed for many applications including clinical diagnostics, medical and pharmaceutical developments, drug detection, quality control of food and environmental [1]. In the recent years, the fields of nanotechnology and diagnostics have opened up new perspectives in biosensor development [2].

1.1 Dengue Virus Disease

Over the last decades, the discovery of biomarkers has played a prominent role for the creation of new diagnosis tools towardthe early detection of diverse diseases [3].

More than half population of the world in 100 countries suffers from the endemic Dengue disease [4-5]. Dengue is a viral mosquito-borne disease from the Flavivirus genus with four serotypes (DENV1-4) that cause fever in the patients infected with dengue virus at tropic and subtopic regionsof the earth [6]. In the recent years, DENV-2 has been reported as the largest dengue epidemic type. Early stage diagnosis of Dengue Virus allows for a better control of diseaseby giving time to prevent the disease's spread [7]. Various types of biosensors have been applied to detect biomarkers for the diagnose of dengue [8]. However, most of these methods are not adequately sensitive and specific for a stand-alone diagnostic tool, so new efforts and biosensing tools especially nanotechnology-based tools are still required [9].

1.2 Gold Nanoparticles

Nano-structured materials have different physical and chemical properties compared to the bulk materials, and these differences have paved the way for multiple applications in the fields of medicine, electronics, catalysis, etc…[10]. Nano-biotechnology is one of the fastest advanced areas of biomedical research. In recent years, nanoparticles have been successfully employed in hyperthermia or radiotherapy cancer treatments, photodynamic therapy, as drug carriers to tumors, and labels for bio-imaging [11]. Nanoparticles ofsmall size can be compared to biological molecules such as antibodies, receptors, and enzymes. Nanomaterials or nanoparticles interact with the biological environment and change the surrounding biological activity.Thestudy of these interactions can be employed for biosensor technology, diagnostic and therapeutic application. A biosensor is an analytical device that basically

consists of two components: a recognition element to attach the target analyte, and a transducer to convert the subtle biomolecular interactions into adetectable signal, mostly as electrical signal. Biosensors based on metal nanoparticles have shown an enormous growth in the recent years [12-13].

One of the most important metal nanoparticles are gold nanoparticles (GNPs). Many research and advanced applications of gold nanostructures have been developed only in the recent decades. Engineering of gold nanoparticles have been employed to developsystems of targeted delivery of drugs and imaging labels,thus overcoming many biological, biophysical, and biomedical obstacles. The historical background of gold nanoparticles comes back to the ancient Chinese and Egyptians in the fifth or fourth century B.C [16]. Some evidences have shown that the ancient Romans used gold colloids to stain glass red or mauve [17].

Gold nanostructures have specific properties interesting for different areas of applied science and technology, which comprise optical and electronic properties, a large surface-to-volume ratio, and flexibility of surface modification.These unique properties have brought intensive focus on the development of simple and effective methods in nanotechnology for diverse biomedical applications, including diagnostic assays, gene and drug delivery to target tissues or tumors and as enhancers/sensitizers of radiotherapy [18]. In recent decades, many research works have been developed to tailor the properties of GNPs for specific applications, especially in sensor development [19]. Different synthetic methodologies provide various properties such as morphology, solubility, stability and surface functionality [20-22].

Gold nanoparticles can be synthesized with a variety of shapessuch as gold nanospheres, nanorods, nanoshells, and nanocages. One of most common methods to synthesize gold nanospheres (with sizes of 2 nm to over 100 nm in diameter) is the facilereduction of an aqueous $HAuCl_4$ solution in the presence of different reducing agents under various conditions [23].

1.3 LSPR

When incident light interacts with metal nanoparticles, it launches a collective coherent oscillation of the surface conduction electrons of the metal.This phenomenon is termed Localized Surface Plasmon Resonance (LSPR). The light interaction with the metal nanoparticles causes a charge separation between the free electrons and their ionic metal core

and the strong coulomb attraction acts as the restoration force for the motion of free electrons, which results in the collective LSPR oscillation [24-25].

The strong absorption of light by the MNPs with different shapes, sizes, and compositions shows different absorption properties for LSPR and these display different colors, such as shown in Figure1.1 [26]. In this figure, aqueous solutions gold nanorods (GNRs) of varying aspect ratios show a range of different colors.

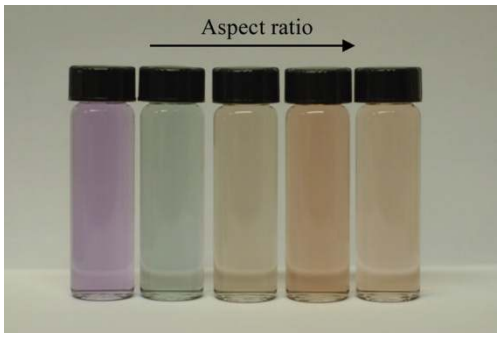

Figure 1.1 GNRs solutions with different aspect ratios that show different colors

Figure 1.2 (a) illustrates the excitation of LSPR for a spherical nanoparticle. The optical absorption spectrum of gold nanospheres (GNSs), shows only one band, Figure 1.2 (b) [26].

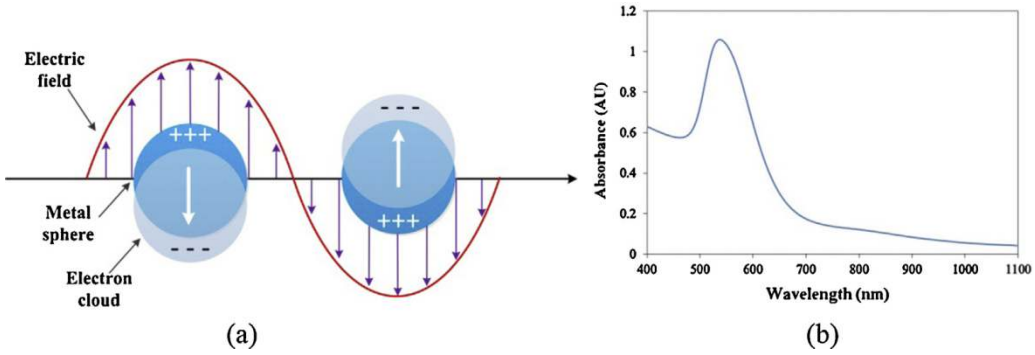

Figure 1.2 (a) Schematic illustration of LSPR excitation for GNSs;(b) A typical LSPR absorption band of GNSs

But GNRs (Figure 1.3 (a) and 1.3 (b)), have two extinctionbands including longitudinal plasmon band (LPB) and the transverse plasmon band (TPB), that are related to the electron oscillation along the long and the short axes of the GNR, respectively [26].

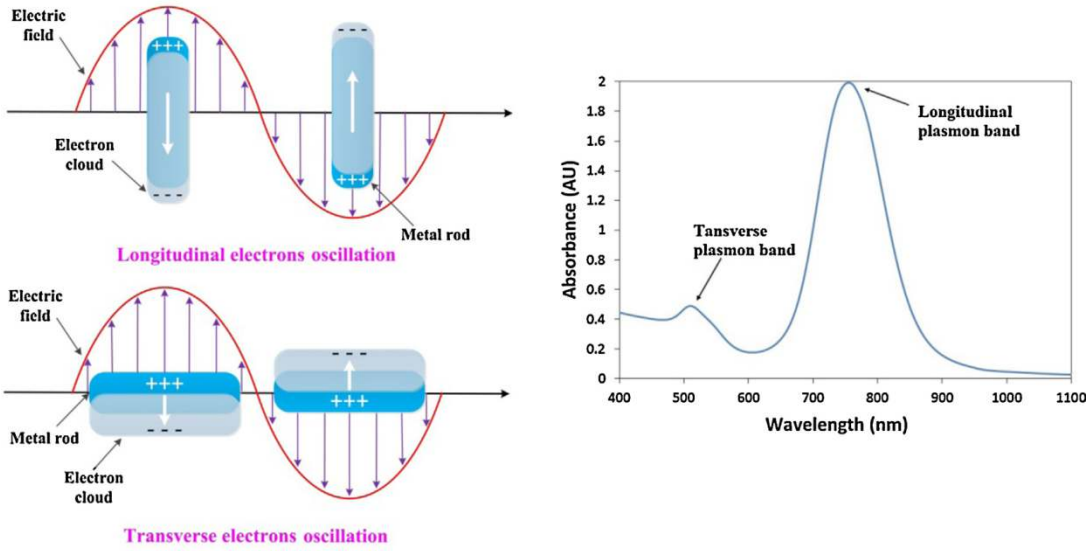

(a) (b)

Figure 1.3 (a) Schematic illustration of LSPR excitation for GNRs; (b) LSPR absorption bands of GNRs: longitudinal and transverse plasmon bands

The LPB resonance wavelength of GNRs is the most sensitive to the surrounding refractive index.Moreover, by increasing the aspect ratio of GNRs, the LPB shows a red-shift and of the sensitivity to the local refractive index also increases. Consequently, the properties of the LSPR are dependent on the size, shape and dielectric propertiesof the metal, as well as those of the local surrounding medium [27-30]. The sensitivityof LSPR to the change of refractive index in the surrounding environment can give useful information about binding of analytes to the surface of nanoparticle. In many sensor schemes, the change of the peak wavelength in the optical spectrum of MNPs is used to signal molecular recognition events [31-32].

Light absorption by LSPR ofspherical MNPs can be theoretically describedby the Mie solution to Maxwell's equations. According to Mie theory for well separated spherical nanoparticles with a radius R (this being much smaller than the wavelength of light, $R/\lambda < 0.1$), the extinction cross-section, C_{ext}, can be expressed as:

$$C_{ext} = (1/\lambda)\,(24\pi^2 R^3 N \varepsilon_m^{3/2})\,[\varepsilon_i/((\varepsilon_r + 2\varepsilon_m)^2 + \varepsilon_i^2)] \qquad \textbf{Equation 1}$$

In this formula, ε_m is the dielectric constant of the surrounding environment, ε_r is the real part, and $\varepsilon_i$is the imaginary part of metal's dielectric function, and N is the number of spheres per

unit volume. As indicated by Eq. 1, the plasmon resonance wavelength occurs when εr= −2εm. For gold and silver spherical nanoparticles, their plasmon absorption bands are located in the visible region, making these materials particularly suitable for many sensor applications.

In accordance to the Mie theory, when radius (R) of spherical particles is smaller than the wavelength of light (λ), the magnitude of the scattering cross-section will be proportional to R^6, and that of the absorption will be proportional to R^3. So due to these prefactors, the LSPR extinction of small particles is dominated by absorption, and upon increasing theparticle size, then scattering takes over.

The sensitivity of metal nanoparticles to the refractive index is dependent not only to the material composition and particle size, but also on the aspect ratio. Elongated nanoparticles such as gold nanorods and gold nano-bipyramids are well-described by spheroidal models, for example, in gold nanorods with radius of 10 nm, the sensitivity increases from 157 to 497 nm/RIU when aspect ratio increases from 1.0 (spheres) to 3.4. For nanorods with the same aspect ratio but different sizes, the larger nanorods have higher refractive index sensitivity [33-34].

LSPR sensors have the flexible design with the low cost in terms of sensor fabrication and it does not require prisms or other optical components. In addition, LSPR sensors can either be fabricated by immobilizing MNPs on a hard substrate, such as glass slide or an optical fiber, or soft flexible substrate such as paper or by suspending MNPs in solution to form a solution-phase based LSPR sensor [35-40]. Moreover, LSPR sensors can even be fabricated based on single nanoparticle, because LSPR is highly localized at each individual MNPs. There are some LSPR biosensors that have superior sensitivity compared to the traditional bulk metal film based SPR biosensors. These advantages of LSPR biosensors over SPR have significantly prompted effort to develop sensitive LSPR biosensors and numerous promising LSPR biosensor designs continue to be reported in the literature [41-42].

1.4 Gold Nanorods

Because of the easy synthesis of spherical gold nanoparticles and their high sensitivity to localrefractive index, many LSPR biosensor had been focused on the GNS, however, the recent developments in LSPR are based on other shapes of MNPs to reach higher

sensitivities. Gold nanorods (GNRs) have demonstrated unique optical properties, such as higher refractive index sensitivity and a tunable longitudinal plasmon band that show excellent characteristics as LSPR biosensors [26]. Moreover, GNRs have also been applied in many other fields such as SERS sensing, chemical imaging and in cancer therapy [43-45].

1.4.1 Site-selective Functionalization of Plasmon Hot-Spots

The tips of gold nanorods are hot-spots of plasmon field enhancement for the longitudinal LSPR mode. The sensitivity to local refractive index is much higher at the plasmon hot-spots. This unique property can be used for designing of plasmonic model sensor in which tip functionalization of nanorods with receptor provides more sensitivity and selectivity for the target sensing [46-47]. Figure 1.4, demonstrates plasmon near field using the method of Discrete Dipole approximation from simulation of a gold nanorod of 10 nm irradiated at the LSPR wavelength (~700 nm) that is much higher than for a gold nanorod 25 nm irradiated at the LSPR wavelength (~650 nm). As it can be concluded these hot spots are also dependent onthe aspect ratio of nanorods, which can be tunedto enhance the sensitivity of model sensor [48-49].

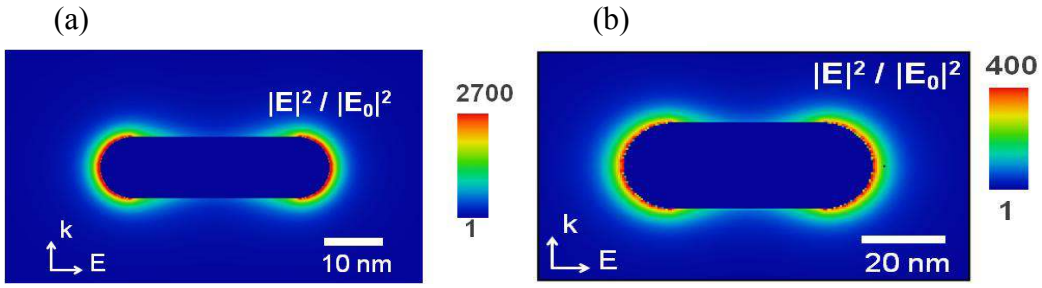

Figure 1.4 (a) Plasmon near field (top) from simulation of a gold nanorod 30 nm × 10 nm irradiated at the LSPR wavelength; (b) Plasmon near field (top) from simulation of a gold nanorod 60 nm × 25 nm irradiated at the LSPR wavelength (~650 nm) using the method of Discrete Dipole approximation.

1.5 SPR

SPR (surface plasmon resonance) is similar to LSPR, but instead of localized plasmon modes, it is based on surface plasmon polaritons on a gold film.The SPR sensitivity to thelocal refractive index is probed by a change in reflected laser light passed through a prism and reflected off from the back of the film. SPR is an important surface analytical technique

because it allows detecting sub monolayer quantities of analyte at the gold film surface and it also allows to measure kinetics data through continuous optical measurements [50]. However, one disadvantage of SPR sensors is lack of localized sensing volume, consequently, it usually needed a thick polymer layer or matrix to cover the gold film surface that must be functionalized with the capture antibodyor other similar bio-receptor. Even though SPR is widely used to study the biomolecular interactions especially for antibody screening regarding to diagnostic and therapeutic applications, it is not widely used in clinical immunoassays or other non-research applications, because it has a lower sensitivity compared to other techniques, and it requires complex optical instrumentation and precise temperature control [51-53].

1.5.1 LSPR and SPR comparison

LSPR sensing with nanoparticle substrates have considerable advantages over the SPR such as simple optical extinction measurement, no temperature sensitivity and requiring common simple laboratory equipment that greatly broaden the scientific and technological applications of LSPR compared to SPR[16]. In addition, nanoparticles have a highly LSPR sensing volume, so LSPR does not need a polymer matrix to trap molecule of interest in contrast to SPR (Table 1.1) [54].

Table 1.1 Overall Comparison of SPR and LSPR sensors

Comparison Parameter	LSPR	SPR
Bulk dielectric Sensitvity (nm/RIU)	10^2	10^6
Sensing Distance (nm)	10	1000
Temperature Sensitive	No	Yes
Simple Instrument	Yes	No

1.6 Biotin-Streptavidin

Biotin−streptavidin linkages are useful tool in nanobiotechnology because the association of streptavidin with biotin is among the strongest known noncovalent protein-ligand interactions ($2.5 \times l0^{13}$ M^{-1}) with exceptionally low dissociation rate [55]. This extremely high binding

affinity of the noncovalent interaction isused for many diagnostic assays that require the formation of an irreversible and specific linkage between biological macromolecules [56]. Although the nature of the biotin-streptavidin interaction is not fully understood. Many research works based the structural and biophysical analysis of the biotin-streptavidin system reveal that the high affinity between Biotin and Streptavidin is due to the multiple hydrogen-bonding interactions, coupled with a deep hydrophobic pocket formed by aromatic residues [57-59]. For example, six H-bonds between the biotin's bicyclic frame and streptavidin,as well as five contacts with the urea functionality and one with thethioether has been determined, in addition, four tryptophan aromatic rings make up the biotin-binding site and shape a deep hydrophobic pocket in streptavidin.

Another reason for importance of streptavidin-biotin couple is thatstreptavidin (SA) has four equivalent sites to bind with biotin (two biotin can interact on one side of the protein and two on the opposite). These sites can be used to link streptavidin irreversibly to up to four biotinylated molecules. The biotin bindinghas minimal impact on the biological properties (recognition specificity, catalytic activity, etc.) of the secondary molecules. So, streptavidin has been identified as a molecular linker in many assays, sensors, purifications and in biotechnology [60].

Site-directed mutagenesis techniques are a new way to alter most of the direct binding contacts to biotin, in which off-rates increase with lower binding affinities making facile capture and release properties compared to the native streptavidin.This strategy is useful for delivering cancer therapeutics through the faster dissociation kinetics and exchange of blocking endogenous biotin with the biotinylated therapeutic [61]. Moreover, these sites are useful for immobilizing secondary molecules chemically modified with biotin without impact on the biological activity (e.g., specificity) of the immobilized molecules. Biotin-streptavidin is especially used in LSPR sensing because biotin with small volume is binded to the nanoparticle surface and after interaction with the larger streptavidin protein it can be detected through the contrast of refractive index. Many LSPR assays of biotin strepatividin interactions have been published, namely, biotin-containing binary alkylthiolate monolayers (BTMs) on gold surfaces immobilize SA with high coverage, specificity, and activity. This makes these SA monolayers as convenient substrates for the development of advanced biosensors [16].

The detected concentrations of streptavidinare in broad range of picomolar to micromolar concentrations because of variations in the observed K_{eq} of the dose response curves due to different affinity obtained upon different experimental conditions. In solution, binding constant of the biotin streptavidin is on the order of $10^{14}M^{-1}$ that in principle it would provide femto molar sensitivities. The reduction of affinity can be related to the effects of conjugation of biotin to the nanoparticle surface such as steric hindrance and limited mobility. However, biotin- functionalized nanorods do not show any plasmonic response upon exposure to non specific targets such as bovine serum albumin, antibodies, and biotin-saturated streptavidin which demonstrates the specificity of this sensing system. Streptavidin detection has also been tested in serum and dilute blood as shown in Figure 1.5 [62-63].

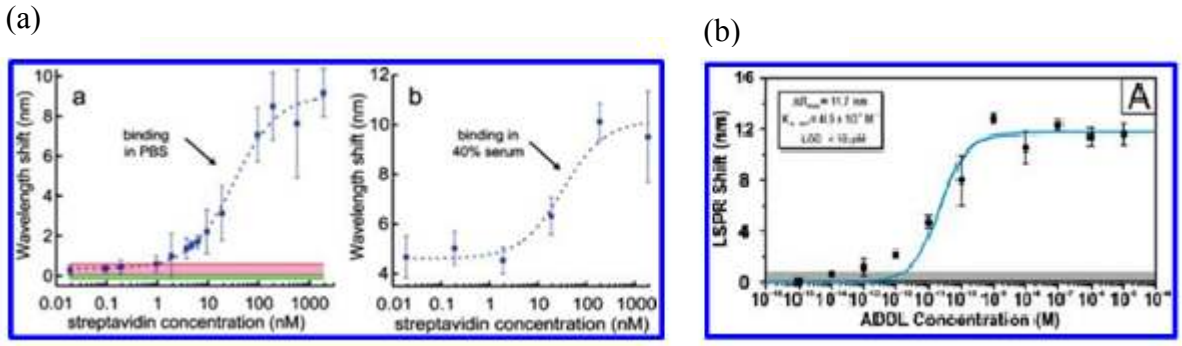

Figure 1.5 (a) The dose_response curve for streptavidin detection with biotin-functionalized gold nanorods in PBS and 40% Human Serum; (b) The dose response curve for ADDL (a marker for Alzheimer's disease) against NP-anti ADDL.

1.7 Label-Free Sensing

One advantage of LSPR sensing make it more interesting for the biological and biomedical assays is that it can performed in label-free conditions. In a LSPR sensor, the target molecule is directly detected because of the target's refractive index [64-67]. This is in contrast to the wide majority of biological sensors based on labels to amplify the target signal [69]. Label-free techniques provide kinetics data but label-based techniques are necessarily carried out as end point assays in that the target is detected through a signal measured before and after analyte exposure. However, labeling strategies for sensors provide biologists considerable signal from small amounts of sample through great amplification and for this purpose many different kind of dye molecules are previously activated for targeting proteins. In labeled sensors, the labels can be radioisotopes, fluorophores, or enzymes [70-71]. In terms of

immunoassays, label-based methods usually require two or more antibodies to the target molecule, whereas label-free assays require only one.

1.8 LSPR in nucleic acid sensing

Nucleic acid sensing finds interest in various fields of life science such as pathology, genetics, clinical diagnosis, the food & drug industry, and environmental monitoring.The specific feature is a robust and specific interaction between complementary nucleic acid sequences [72-73]. In recent decade noble metal nanoparticles have been using broadly for nucleic acid detection along with nucleic acid-controlled self-assembly [74]. For the detection ofbiomarker, gold nanoparticles interact with biomolecules, such as nucleic acids, antibodies, proteins and make a stable and benign nanoparticle bioconjugates, while keeping their optical characteristics [75-76]. GNPs coupled to Deoxyribonucleic acid (DNA) or Ribonucleic acid (RNA) probes are well known as platforms for designing of new advanced DNA and RNA sensors, because of biocompatibility, easy functionalization, and stability in many solutions including the biological matrices. Additionally, these particles are useful for enhancement of the precision and accuracy down to single biomolecule sensitivity.As a consequence, a new generation of nucleic acid sensors based on these nanoparticles have been developed [77-80].

These nanosensors have been designed based on different kind of detection techniques encompassing plasmonic scattering, Raman scattering, colorimetric, luminescence, and electronic detections of nucleic acid [81].

In fact, the nanoparticles are used to act as a light source to modulate energy transfer to/from biomolecules closed the particle's surface. Importantly, the plasmons of gold nanoparticles (AuNP) can behave as an energy sink to account for the hybridization of target DNA or RNA [82-85].

Three common sensing platforms using the LSPR of noble metal nanoparticlesthathave been developed consist of colloidal homogeneous sensing, surface-confined heterogeneous array sensing, and surface-confined heterogeneous single nanoparticle sensing. Each method has its own advantages over the others. For example, colloidal methods are fast and simple, while single plasmon biosensors increase the limit of detection (LOD) and make possible the study of biological process at the molecular level [40].

There are three main sensing categories based on the application of LSPR of metallic nanoparticles in nucleic acid detection, comprise detection by absorbance, scattering, and LSPR energy. In all of three categories, the main factors that greatly influence on the detection efficiency are types of plasmonic nanoparticles, the nucleic acids, the recognition length, as well as the buffers. The detection efficiency is described by the detection time, lowest sensing concentration (LOD), to assess thesensitivity, and single-base mismatch (SBM), to assessselectivity [86].

1.9 Porphyrins

Porphyrins and related families are unique and stable organic modules containing macrocyclic tetra-pyrrole connected by the methine bridges. Porphyrins show rapid tautomerism due to the two inner pyrrolic protons delocalizing in four pyrole rings (Figure1.6 (a)). Most of these aromatic macrocycles are purple powders and have visible colour in solutions (Figure1.6 (b)). They are usually synthesized by acid-catalyzed condensation of pyrrole and aldehyde building blocks followed by oxidative treatment [87].

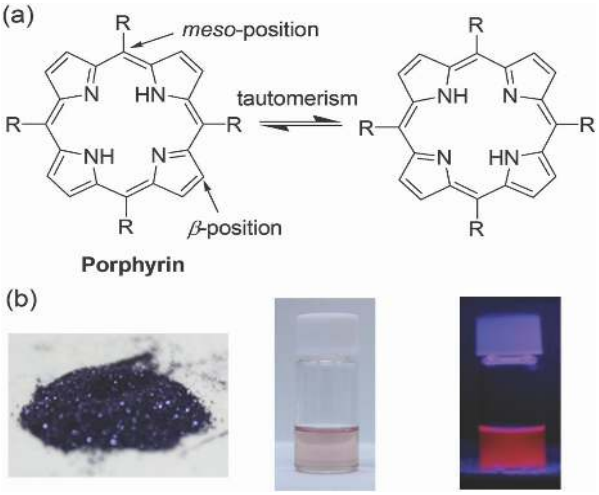

Figure 1.6 (a) Structure of porphyrin and tautomerism;(b) Porphyrin's powder and solution.

Modification of the porphyrin core with various functional groups and other elements provide them unique optical, electronic and magnetic properties making them interesting moleculesto focus on their interactions with other molecules and external stimuli, especially for the sensing applications [88]. Among several porphyrin families, the water-soluble cationic porphyrin, 5,10,15,20-tetrakis(N-methylpyridinium-4-yl)-21H,23H-porphyrin ($TMPyP^{4+}$)

(Figure 1.7) has been used in diverse fields because of its physicochemical properties [89-91].

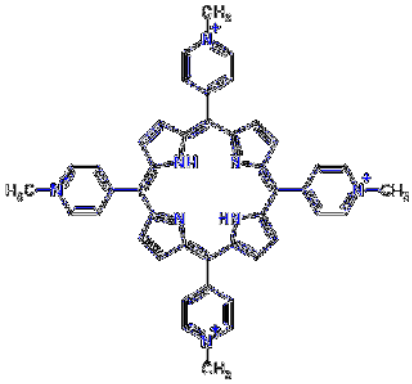

Figure 1.7 Chemical structure of 5,10,15,20-tetrakis(N-methylpyridinium-4-yl)-21H,23H-porphyrin ($TMPyP^{4+}$)

The optical spectrum of porphyrins showa sharp and intensive absorption band around 400–500 nm corresponding to a π–π* transitions with molar extinction coefficients $4\times 10^{5}M^{-1}cm^{-1}$. This absorption band is named Soret or B-band, as shown in Figure 1.8. Moreover, there is a set ofother **e**lectronic absorption bands with weak intensity in the range of 500–700 nm known as Q-bands. For free-base porphyrins,four Q-bands are found in absorption spectrum because of D_{2h}symmetry ofits macrocyclic structure, but in the case of metalloporphyrins, usually there are only twoQ-bands, due to an increase to D_{4h}symmetry. The Soret and Q-bands both arise from π–π* transitions based on the four molecular orbitals (HOMO and LUMO orbitals). These absorption bonds can change in terms of both location and intensity with many parameters such as kind of interactions with other moleculeswhich can be hydrogen bonding, donor–acceptor, coordination bonds and interactions at the macrocyclic **c**ore and periphery.Some examples of these interactions are assembly/disassembly of porphyrins, tautomerization, and/or physical properties of surrounding environment comprising temperature, pH and solvent polarity. The influence of these parameters on porphyrins structure can be can be assayed by the UV-Vis spectroscopy that is very useful for sensing applications [92].

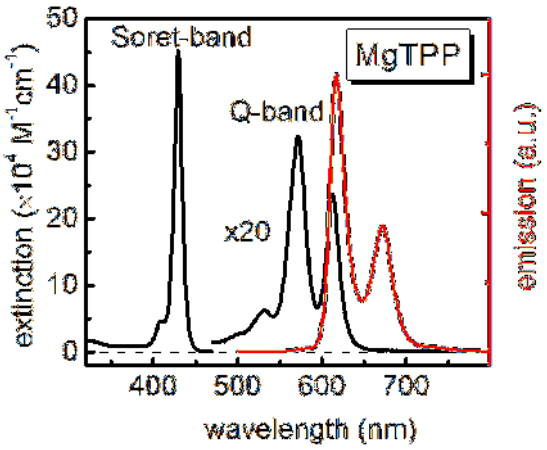

Figure 1.8 Soret bond and Q-bonds of Porphyrinchange to free base example in absorption spectra

1.9.1 Porphyrin-DNA Interactions

The DNA hybridization technique is widely used in diagnostic laboratories for biosensing of infectious disease pathogens and genetic variations.The use of DNA technologies for sensing applications provides sensitive, easy-to-use, fast, inexpensive, and miniaturized analytical devices. Moreover, the characterization of organic moleculesthat specifically interact with DNA and their molecular mechanisms underlying the machinery of living cells could be highly relevant fordrug design [93-94]. Porphyrin have been increasingly used as water soluble cationic porphyrin studied for optical DNA diagnostics and many research workhas been focused on Porphyrin-DNA interactions. In this regard,cationic porphyrin, 5,10,15,20-tetrakis(N-methylpyridinium-4-yl)-21H,23H-porphyrin ($TMPyP^{4+}$) (Figure 1.7) has received substantial interest, because of its specificity in DNA binding, as well as its potential applicability in photodynamic therapy [95-99]. For example, many reports in the literature strongly support the specific intercalation of $TMPyP^{4+}$which binds to the major groove of Adenosine (A)-Thymine (T)-rich DNA through electrostatic interaction between positively charged N-methyl pyridinium moieties of $TMPyP^{4+}$ and negatively charged phosphodiester backbone of AT pairs of DNA [100-105].

A simple binding strategy to DNA through electrostatic interactions between the ionic side groups of DNA and water soluble cationic conjugated polymers is of considerable importance to gain an insight for drug design as well as the biosensor systems that benefit from the light harvesting properties along the conjugatedpolymer backbone.

The porphyrin is a multifunctional anchor that can act as an electron and/or energy transfer component and as a ligand docking site for potential coordination interactions. Furthermore, the size, shape, and hydrophobicity of porphyrins are quite similar to cholesterol, suggesting similar physical interaction for these two molecules in the lipid membrane [106-107]. Porphyrins have been covalently attached to DNA: at the 3' or 5' group of the sugar; on the phosphate backbone; on an adenine base; and as a base replacement. Circular dichroism (CD) has been the method of choice to study these chiral porphyrin systems [108-110].

1.9.2 Porphyrin-metal nanoparticles Interactions

Metal nanoparticles and chromophores have been widely studied as components of thin film hybrid materials for photovoltaic, optoelectronic, and bioanalytical applications. Different chromophores, for example, pyrenes and porphyrins, have been assembled on the surfaces of gold nanoparticles [111-115]. The process following the excitation of the chromophore can be energy or charge transfer to the gold nanoparticles [116-118]. Besides changing the nonradiative decay rate, the proximity of nanoparticles can also change the radiative decay rate of the chromophore [119]. The relaxation path of the excited chromophore depends: on the distance between the chromophore and the gold nanoparticle; on the orientation of the molecular transition dipole moment of the chromophore relative to the gold nanoparticle surface; and on the gold nanoparticle size [120-123]. The excited gold nanoparticles can also act as energy donors to chromophores. The preparation of chromophore-functionalized gold nanoparticles requires modification of the chromophore with a linker for covalent attachment to the gold nanoparticle surface [124-126]. Alternative ways to assemble chromophores in close contact with gold nanoparticle surfaces are, for example, spin coating and Langmuir-Blodgett methods [127]. Langmuir films of gold nanoparticles have been transferred to solid substrates, and they form ordered structures. Solid devices combining gold nanoparticles and chromophores have been already built, for example, for photovoltaic devices and light-emitting diodes (LEDs) [128-131]. The optimization of these solid devices requiresunderstanding the interaction mechanism between chromophores and gold nanoparticles in solid assemblies and, thus, is an important issue to investigate [132-133]. Many optical instruments and techniques, such as steady-state fluorescence, time-resolved fluorescence (nanosecond time scale), and transient absorption (picoseconds and microsecond time scales) provide beneficial details about the charge and energy transfer processes between

porphyrin and gold nanoparticle films. Two important points for this approachthat should be taken into account are, firstly, the film composition of porphyrins and gold nanoparticles, for the successful film deposition and, secondly, the molecular density to obtain a strong interaction. The usual mechanism of fluorescence quenching of chromophores by gold nanoparticles is energy transfer, and thus, it can be expected that energy transfer plays also a role in films of porphyrins and gold nanoparticles [134-139].

In addition to solid films, many research works about chromophore-functionalized gold nanoparticles have been performedin solution, in which the fluorescence of the chromophore can be quenched by either energy or electron transfer. The life time enhancement of fluorescence in chromophore is induced by changes both in the radiative and non-radiative decay rates [92].

1.10 Single Molecule Spectroscopy (SMS)

In recent years, advances in ultrasensitive optical instrumentation have opened a new experimental window for single-molecule detection [140-153]. The first single molecules were studied by absorption [154] and fluorescence excitation [155] made high photostability as well as the absorption cross-section provided the recording of both excitation and emission spectra of individual molecules [156-158].
Optical detection of single molecules comprises both frequency-modulated absorption and laser-induced fluorescence.

A single molecule emits the fluorescence in four-step cycle including [159]:

1. Transition of electron from the ground state to an excited state;
2. Internal relaxation within the vibration states in the excited state;
3. Relaxation from the excited state to the ground state through radiative or nonradiative decay that is measured as the excited-state lifetime. The excited-state lifetime and the absorption time been determined in the short range of sub-nano to nanosecond.
4. Internal relaxation in the ground state through the both vibrational and rotational relaxations which for small molecules in the condensed phase usually are in the range of picosecond nanosecond range.

The Jablonski diagram (Figure 1.9) shows the mechanism of fluorescence based on the relaxation of a molecule's excited-state [160].

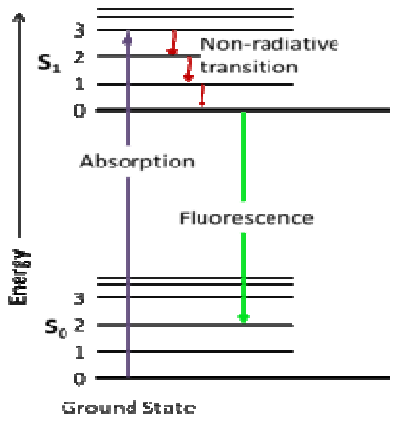

Figure 1.9 Jablonski diagram, when an electron absorbs a high energy, then the electron relaxes fluoresces with a longer wavelength.

For weak excitation powers, the frequency of absorption events and the intensity of fluorescence will depend linearly on thelaser excitation power. For intermediate excitation powers, thefrequency of absorption events begins to become limited by the excited-state lifetime, thus leading to the onset of optical saturation, and the intensity of fluorescence becomes weakly dependent on laser power. Finally, when the excitation of power is high, the absorption time is shorter than the excited-state lifetime, consequently, the signal of fluorescence is determined by the excited-state lifetime, and so it will not depend on the laser power. For example, the optical excitation-emission cycle rates for many fluorescent dyes are about 10^7–10^8 per second with 1.0 mW laser beam focused to the diffraction limit [161-162].

1.11 Confocal Microscopy

Among the various single-molecule technologies, the detection with optical methods standsout because of its advantages, such as greater sensitivity, electrical passiveness, and robustness. Moreover, the optical detection of single molecules can also be used over a wide range of concentrations. There are several optical methods have been developed to study single molecules [163].Confocal microscopy have employed for imaging and time-resolved microscopy of single molecules at a polymer-air/liquid interface, this technique have been extended to study single-molecule dynamics at room temperature especially for analysis of

protein-DNA interactions to study biological mechanisms and biomolecular science [159, 164-169].

Scanning Confocal Fluorescence microscopy is particularly attractive since high detection sensitivity and sufficient reduction of background signal allow the observation of individual fluorescent molecules. In addition, with a single scan, multiple fluorescence emission wavelengths from specificmolecules can be detected at the same time. With this procedure, the molecules of interestare not influenced by physical interaction with a scanning probe. In contrast, other single molecule techniques, like Atomic Force Microscopy (AFM) (170-172) or Near-field scanning optical microscope NSOM (173-174), require a probe in very close proximity to the sample, which may result in undesirable interactions. Another advantage of single molecule studies using scanning confocal microscopy is that samples can be prepared in such a way that equilibrium reaction conditions are maintained during scanning [175-176].

The main issue in these methods is the isolation of single molecules for detection. The method of single molecule detection can be categorized in three regimes including detection on dry surface, detection in solution with very law concentration, and in solution with high concentration (native physiological condition).

Single molecule detection in solutions with high concentration of native physiological conditions is very difficult for optical detection so the isolation of individual molecule on a surface or in dilute solution are more convenient methods. Particularly, optical detection of single molecules on a dry surface or in solution can be enhanced using nanostructures that enhance the fluorescence and modify the radiation direction because spatially separated from each other in the area or volume probed by a laser beam [177-178]

Confocal microscopes work by, principally, selecting the excitation wavelength, then discriminating between excitation and fluorescence emission and finally restricting the emission wavelengths detected. A confocal microscope incorporatesa pinhole located between specimen and detector that select information from a single focal plane, and makes a sharply focused optical slice through the specimen, and finally it takes a series of optical slices atdifferent focus depthin the specimen to generate a 3D data set. In the setup used, there is a piezo-element on which the microscope's objective is mounted that raster scans a point of laser light across the specimen (epi-illumination) (Figure 1.10) [179-181].

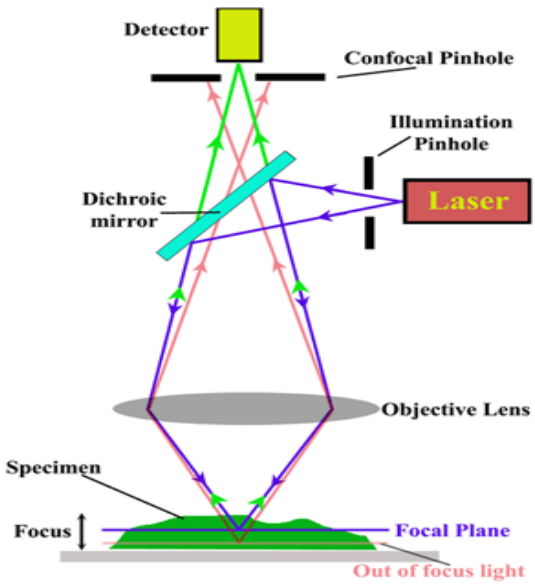

Figure 1.10. Principle of confocal microscopy [159]

1.11.1 Laser-induced fluorescence (LIF)

Fluorescence spectroscopy plays an important role today for single molecule detection [182-184]. Fluorescence have two unique advantages useful for molecular detections encompasses high intrinsic optical efficiency and principally make it possible to reach many useful information about the molecular environment and structure through different ways such as brightness [185], lifetime [186-190] abbreviated as FLIM (Fluorescence Lifetime Imaging Microscopy), anisotropy [191-193] or spectrum [194].

Compared to many spectroscopes have been applying in disease detection, Laser-induced fluorescence (LIF) is one of the most practical spectroscopic methods as a powerful analytical technique fortumorous diagnosis [195-197]. There are several advantages known for the diagnosis of diversified diseases by the LIF consist of high sensitivity, short testingtime, low sample consumption, safety and in situ testing,high sensitivity and specificity, in addition of the low concentration limit around 10^{-13} mol/L and even single molecule level for the fluorescent probe with high fluorescence efficiency [198-200].

1.11.1.1 Data analysis of Lifetime in FLIM

Fluorescence relaxation from S_1 to S_0 transition can be characterized through three quantitative properties comprising fluorescence spectrum that provides fluorescence intensity as a function of a wavelength, quantum yield (Φ) defined as the ratio of the total number of

emitted photons per number of absorbed photons, and fluorescence lifetime (τ) which is the average time of the excited molecule remains in the excited state. To make the image in FLIM, the lifetime of the fluorophore signal is the more important feature rather than its intensity and this is an advantage because of minimizing the effect of photon scattering in thick layers of sample.

In general, the fluorescence lifetime image is calculated by sorting all photons corresponding to one pixel into a histogram. In FLIM image, the fluorescence is a function of time. The resulting data of all pixels is stored as a matrix in that each column demonstrates the fluorescence decay associated with a single pixel x, such that I (ti ,xj) that is the fluorescence intensity at time ti in pixel xj . Then it is fitted to an exponential decay function to extract the lifetime information. This treatment is then repeated for every pixel in the image.

The fluorescence decay should be convolved with the instrumental response function (IRF), which is either obtained from a scattering sample or from a single fluorescence-lifetime standard. The figure 1.11 shows time-correlated single-photon counting (TCSPC) histogram.

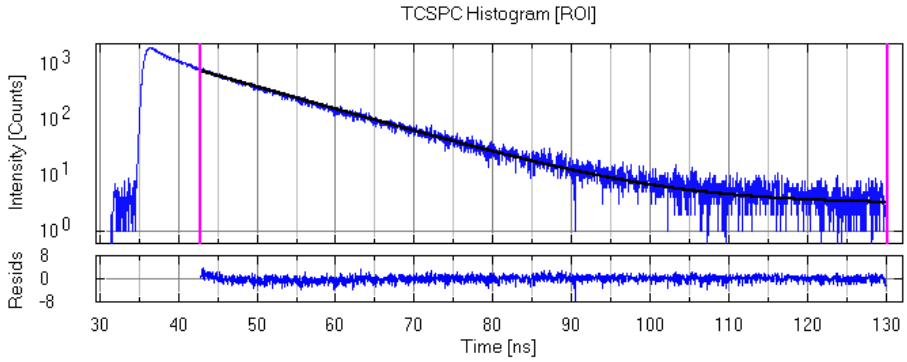

Figure 1.11 TCSPC histogram [201]

1.11.2 Plasmon-enhanced fluorescence (PEF)

Single-molecule spectroscopy based on laser-induced fluorescence provides fast, high-contrast, and low-background detection of single molecules especially in cell biology [202].
In fact, most of strongly absorbing molecules such as biologically relevant proteins and metal complexes have very weak fluorescence because of the low fluorescence quantum yield or a long fluorescence lifetime, that makes it difficult to detect them by single-molecule spectroscopy [203-204]. The enhancement of fluorescence rate in weak emitters can lead to a broad spectrum of new advanced applications. Plasmonic nanostructures are known to enhance the fluorescence emission rate of weak emitters [205-206].

In recent years, research works focusing on Plasmon-enhanced fluorescence (PEF) have grown exponentially due to the extremely productive symbiosis of plasmonics and spectroscopy to achievecontrol over spontaneous emission. In addition, PEF not only enhances emissions and cause decreasing of lifetimes, but also it provides a way toward imaging with a resolution considerably better than the diffraction limit [207-211]. Through the combination of metal nanostructures and quantum emitters a new class of photostable probes canbe created with high emission brightness [212-215]. This novel feature is derived from the large optical extinction cross section (that comprises both absorption and scattering) in plasmonic nanostructures, which isseveral orders of magnitude larger than that of molecular fluorophores.Consequently, through coupling of fluorophores and localized surface plasmons in the vicinity of metal nanostructures, it can be achieves a large increase in the excitation and decay rates of the fluorophore. This coupling improves brightness of molecular emission, thus, leading to an increase in detection sensitivity. Figure 1.12 shows a simple schematic of plasmon enhanced Fluoresence [217].

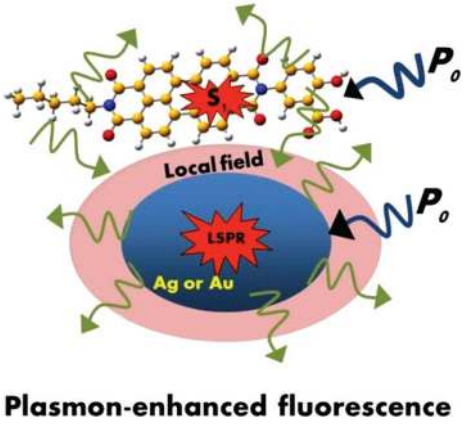

Figure 1.12 Schematic simplified showing plasmon enhanced fluorescence [217].

Mechanistically, it can be perceived as if the plasmonic nanoparticle focuses the electromagnetic field of incident light close to its surface, thereby increasing the light absorption by the fluorescent molecule near the particle [218-220]. On the other hands, the nanoparticle affects the radiative and nonradiative decay rates of a molecule near its surface and it can cause efficient fluorescence enhancement. The aforementioned factors are dependent on the plasmonic resonances of the nanoparticle, where and how the molecule is oriented relative to the nanoparticle, and on the spectral overlap between the nanoparticle and molecule [217, 221-222].

Based on many experimental researches, the overlap between the molecular absorption and emission spectra of the fluorophore and the LSPR of a metal nanoparticle produce the highest fluorescence enhancement factor that occurs when the former is slightly red-shifted relatively to the LSPR of the particle [225-226].

1.11.2.1 Engineering of Plasmon-enhanced fluorescence

There are several investigations for engineering of plasmonic nano probes to obtain more stable and stronger flouresence signal response. For example, nanostructures with edges, such as gold nanorods, gold nano-bipyramids and gold nanocubes can show enhanced quantum yield of photoluminescence (PL) because of the "lightning-rodeffect" (Figure 1.13) [217] and GNRs have been extensively used for the luminescence of one-photon and two-photon by coupling the excitation laser wavelength and longitudinal LSPR energy [227-229].

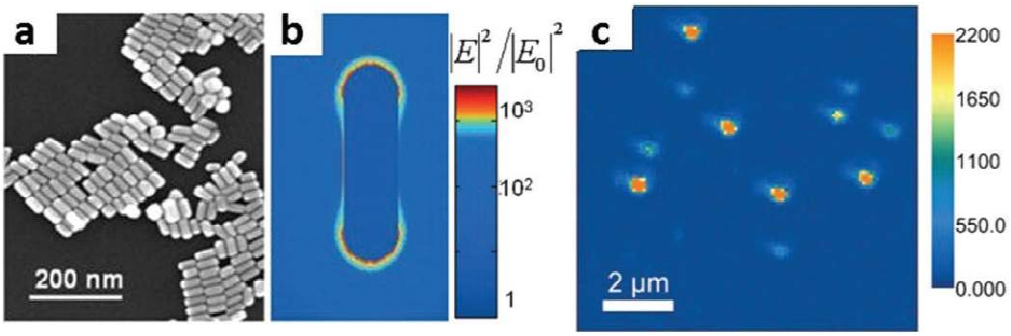

Figure1.13 (a) SEM image of gold nanorods; (b) Simulation of near field around a single nanorod; (c) Fluorescence imaging of single molecule detction that enhanced bynanorods

In the recent years, using silica or human serum albumin make a spacer layer between metal nanoparticles (GNS or GNR) and fluorophore to increase the flouresence intensity [230-235]. Low porous silica spacers have rigidity property and provide very good control of distance between metal and fluorophore, effectively avoiding metal-fluorophore contact, and protecting the metal from ions present in biological media. Other advantages of using a silica layer are their robustness, chemical stability, and versatility of surface modification, for example, for the conjugation of biomolecules or dyes [237-238].

Another strategy suggests a gold core covered by an interstitial nanoscale silica layer and then another shell layer of gold that covers this silica layer. This novelty provides much higher flouresence enhancement or quenching of the fluorescence emission from the fluorophores dispersed within the internal dielectric layer [241].

As a consequence of MEF dependence on the distance between the flourophore and the metal surface, different flexible kinds of spacer materials such as peptides, DNA [242-243] and [244-246] have been developed that are greatly considered for biosensing as biomarkers to detect disease in early stages. Recently plasmonic chips trough the MEF detections have been integrated to the conventional antibody−antigen sandwich assay and caused∼100-fold enhancement in the sensitivity detection of target biomarkers. This method can also be applied for sensing approaches in microarray of the different types of cells by MEF-baseddetection on a single chip [247].

However, there is a disadvantage for DNA and polymers as spacers corresponding their flexibility that make it difficult to have completely controlling on the flourophore–metal distance and consequently, sometimes they cause emission quenching.

2. Experimental

2.1 Materials and Instruments

Gold nanorods stabilized with CTAB andof size approx. 10 nm × 30 nm were purchased from Nanopartz Inc, as aqueous suspensions with an optical density of 1 or 100 (product # A12-10-700 or A12C-10-700). Reagents for the synthesis of thiolated biotin linker including EZ-Link™NHS- Biotin and EZ-Link™ NHS-PEG4-Biotin were purchased from Fisher Scientific and used as received. Cysteamine (purity above 98%), (3-Mercaptopropyl)trimethoxysilane (purity of 95%), Hexadecyltrimethylammonium bromide or CTAB (BioXtra grade),Biotin (purity above 99%), and Streptavidin extracted from Streptomyces avidinii, purified and lyophilizedfrom 10 mM potassium phosphate, were all acquired from Sigma. Methyl-PEG4-thiol reagent was purchased from Fisher Scientific and used as received. Solid Phosphate buffer saline (PBS) tablets from Sigma were dissolved in Milli-Q (Merck Millipore) deionized water. Ethanol absolute was from Panreac. Rectangular glass slides with thicknesses 1 and 1.5 shapewere acquired from Menzel-Gläser or Deltalab. The surfaces of glasses were cleaned in a UV/Ozone chamber model PSD-UV3 from Novascan. Absorption spectra were measured in a Perkin-Elmer Lambda 35 UV/vis spectrophotometer, and emission spectrawere measured in a Fluorolog Tau-3 spectrofluorimeter Fluorescence Lifetime Imaging Microscopy, FLIM, measurements were obtained with a time-resolved confocal microscope (MicroTime 200, PicoQuant GmbH).

2.2 Preparation of glass immobilized-gold nanorods

Glass coverslips with dimension of 24 × 60 mm and thickness # 1.5 were cleaned through several steps: firstly, by UV/ozone treatment for 90 min; secondly,by immersing in HCl solution (1 mM) during 1 hr;thirdly, by rinsingthoroughly withwater; and, in a final step, it was cleaned by sonication in both waterand methanolfor 10 min and N_2blow dried after each sonication. In order to prepare the glass surface for the immobilization of gold nanorods, the coverslips were silanized by immersion in a solution of (3-Mercaptopropyl)trimethoxysilane, 5% (v/v) in ethanol, then rinsed with ethanol,and finally submitted to sonication in methanol for 10 min.The activated glass provides thiol groups to react covalently with the gold nanorods ensuring their immobilization for the subsequent chemical modification.

The gold nanorodswere centrifuged three times and after each centrifugation step, the supernatant was replaced with an aqueous solution of CTAB (0.10 μM) in order to wash down CTAB concentration from stock solution. The suspension of gold nanorods was dispensed on the silanized glasssurfaces by placing a drop of approx. 200 μL on a surface area of 1cm^2 and letting it stay for 20 min, followed by rinsing with water and blow drying with N_2. In order to reach the desired particle density of gold nanorods corresponding to approximately an O.D. of 0.003 to 0.010, this step repeated 2-3 times.

2.3 Tip-specific functionalization of gold nanorods with biotin receptors

In order to attach biotin receptors on the particle's surface, a thiol linker was used. The biotin thiol linker was synthesized by the reaction of EZ-Link™ precursor (10 mM) with cysteamine (1 mM) in PBS buffer for 30 min. This thiol linker hasa length of four oligoethylene glycol spacer and we named it PEG-4. After the preparation of coverslips, as described in section 2.2, the tip functionalization step was carried out by incubation of the area where rods were immobilized with a CTAB solution (ca. 1 mM) for about 30 min. Then, the CTAB solution was removed from the surface and replaced with a solution of biotin thiol linker (1, 10 or 100 μM) and CTAB ca. 1 mM) for 90 min. The CTAB molecules act as a barrier against the attachment of thiolated biotin receptor in the sides of gold nanorods by making a bilayer coating that is more compact over the side of the rods than on the tip area. Consequently, thiolated biotin attaches preferentially at the tips of gold nanorods. In a final step, after rinsing with water, the coverslips were left in PBS buffer during the night to remove any reactant residues. Complete removal of CTAB surfactant is a critical point in the following experiments to avoid any interference during the sensing assays. Another method of functionalization, named here full functionalization, consists of fully coating of gold nanorods on the glass surface with thiolated biotin receptors.

2.4 LSPR Sensing of Streptavidin with Biotin-functionalized Gold Nanorods

A liquid cell was prepared by attaching the cover slip of immobilized gold nanorods and functionalized with biotin receptor (PEG-4) over a clean glass slide using melted Parafilm M with an approximate thickness of 1 mm to produce a liquid cell. The liquid cells have a volume of approximately 500 μL for the sample solution. To remove any residuals from

liquid cell assembly, the liquid cellswere left in PBS buffer for overnight. For the sensing assay, a solution of streptavidin was prepared with concentrations of 100 nM and 1000 nM in PBS buffer from a protein stock solution prepared by dissolving 1mg of protein in 1 mL of PBS.

Firstly, the transmission spectra of the immobilized gold nanorods in the liquid cell filled with PBS was measured by optical spectroscopy to determine the peak wavelength of the longitudinal surface plasmon (LSP) band. After that, the PBS buffer was replaced with the streptavidin solution with concentration of 100 nM, and transmission spectra were measured over a wavelength span of 100 nm around the peak position at a speed of 120nm/min during 90 min. After this first kinetic binding assay, the solution in the liquid cell was replaced by streptavidin solution with a higher concentration of 1000 nm, and transmission spectra were measured at speed of 120nm/min for 60 min.

All spectra acquired were fitted with a Gaussian function to precisely determine the peak wavelength. Kinetic time traces were obtained from plotting the peak wavelength change over time. The kinetic traces were fitted by a single exponential or astretched exponential function and to judge the quality of the fits it was used the residuals plot. The longitudinal plasmon resonance (LSP) shift was calculated from the difference between the end value of the fitted exponential function and the initial peak positionof the kinetic assay.

2.5 Nucleic Acid Hybridization and Dengue Virus RNA Biosensing

The direct refractometric detection of the target oligonucleotides was attempted first with gold nanorods fully-functionalized with complementary DNA probe sequences. The increase of local refraction index upon hybridization on the nanorods' surface was expected to red-shift their plasmon resonance. The plasmon red-shift detected by optical spectroscopy was used as a readout signal for the detection of target nucleic acids. In view of the short sequences targeted, it was devised a strategy for DNA-directed bio macromolecule or nanoparticle assembly, in order to amplify the plasmon responses.

Three examples of biosensing assays were carried out:

1) tip functionalization of gold nanorods was performed using CTAB bilayer to attach a thiolated ss-DNA probe sequence, and then hybridization with a biotinylated Dengue virus RNA target sequence was monitored by optical absorption spectroscopy. After that, the

samples were exposed to streptavidin, in order to promote its binding to the nucleic acid hybrids on the nanorod surface toward an amplified plasmonic response;

2) full functionalization of gold nanorods with a thiolated ss-DNA probe sequence, and then hybridization with a biotinylated Dengue virus RNA target sequence was monitored. After that, the samples were exposed to streptavidin, in order to amplify the plasmonic response;

3) full functionalization of gold nanorod with a mixed monolayer of a thiolated nucleic acid hybrid (obtained from the probe DNA and the target Dengue virus RNA sequences) and a thiolated PEG-4 molecule used as a spacer between nucleic acid chains on the nanorod's surface. After that, the samples were exposed to antibiotin anti-body (1μ dilute 1000 times), in order to further amplify the plasmonic response, due to the larger volume of this antibody when compared to streptavidin.

The detection of nucleic acids was performed with gold nanorod model sensors immobilized on a solid surface, which has advantages in terms of particle colloidal stability but, on the other side, this approach is prone to interferences by non-specific surface interactions. The immobilization of the core nanorod on a solid surface limits the satellite assembly to one layer, but it opens up the possibility of carrying single-particle spectroscopy studies.

2.6 Interaction of Dengue Virus DNA and TMPyP Porphyrin in solution

Studies on the interaction oftetracationic TMPyP with polyanion single or doublestrand DNA have shown specific interactions depending on the DNA sites, sequences and concentration. These interactions can be monitored from their influence on the porphyrin's structure and electronic properties by UV-Vis spectroscopy. For this purpose, solutions with different concentration ratios of single strand Dengue Virus DNA and TMPyP of 0.02, 0.01, 0.1, 0.2, 0.5, 1, 2 were prepared in PBS buffer at room temperature and left to equilibrate for 20 min. In order to investigate the interaction of double strand Dengue virus with TMPyP, first a solution of Dengue Virus DNA sequence with its complementary was prepared in PBS buffer solutions and allowed to hybridize for 20 min. Then, a series of solutions with concentration ratios of 0.02, 0.01, 0.1, 0.2, 0.5, 1, 2) between double strand Dengue virus DNA and TMPyP were prepared at room temperature and allowed to equilibrate for 20 min. The absorption spectra of all solutions were measured by UV/Vis Spectroscopy in the range of 220-850 nm at a speed rate of 240 nm/min.

The porphyrin can act as an electron and/or energy transfer component respective to DNA, which can be used to monitor the interaction between these species by fluorescence spectroscopic techniques. So, the fluorescence emission intensity and lifetime decay for all samples were also measured.

It should be noted that Circular Dichroism is another technique that may afford information about Porphyrin-DNA complexation, and for this reason, it was also employed here.

2.7 Single-Particle Spectroscopy of Gold Nanorods

2.7.1 Sample preparation

Gold nanorods were immobilized on a glass cover slip surface that had been previously coated with (3-Mercaptopropyl)trimethoxysilane. For this purpose, gold nanorods from stock solution were washed three times and finally reconstituted to give a suspension with an approximate OD of 2. In order to obtain single particles dispersed on the activated glass surface, a drop of a dilute solution of gold nanorods was placed on the surface for 20 min and removed before its evaporation. The gold nanorods were functionalized with thiolated DNA oligonucleotides using the full functionalization procedure previously described. The plasmonic detection of the target sequences was performed at single-particle detection level using a confocal microscopy. The one-photon photoluminescence of gold nanorods was used to monitor the longitudinal surface plasmon resonance in response to hybridization with the Dengue virus DNA-analogue sequence. The ability to resolve the optical signal from single objects was used to study heterogeneity in the gold nanorod sensor response, which is typically averaged in ensemble measurements.

2.7.2 Confocal Fluorescence Lifetime Microscopy

For single molecule detection, a confocal microscope was used, as described in section 2.1. The prepared sample was placed in the microscope sample holder that is perpendicular to the excitation light. A small drop of PBS buffer solution or water (5 μL) was placed on top of the area where individual gold nanorods are present. The light propagates through the bottom of the sample in the inverted microscope configuration. A pulsed picosecond diode laser was

used to excite the sample at a wavelength of 482 nm. A high numerical aperture objective makes it possible to focus the light into a small volume (of only a few femtoliters of excitation volume) inside the sample. The scanning of the objective is performed with a X,Y,Z–piezo driven device. After sample emission, the light collected travels in the reverse pathway and it passes, firstly, through a dichroic mirror; secondly, through an emission filter, either a long pass for wavelengths above 510 nm, or a band pass of 55 nm centered at 695 nm; and, thirdly, through a 50 μM pinhole that eliminates out-of-focus light providing confocal detection. The fluorescence is detected using two single-photon counting avalanche diodes (SPAD) (PerkinElmer) and the signal is processed by Time Harp 200 TC-SPC PC board (PicoQuant) working in the time-tagged time-resolved (TTTR) operation mode.

2.7.2.1 Single gold nanorods interaction with TMPyP porphyrin

In order to achieve fluorescence enhancement (Plasmon-enhanced fluorescence, PEF), gold nanorods were used as optical antennas to enhanced the emission of TMPyP porphyrin in solution. The TMPyP molecules are free to diffuse and explore the enhanced local field from the localized surface plasmon modes of gold nanorods that are surface-immobilized. Depending orientation and distance of fluorophore relative to the metal nanostructure, the enhancement effect can vary significantly.

Fluorescence enhancement experiments were performed by placing a small droplet of TMPyP porphyrin in water or PBS buffer solution with a concentration of 100 nM (volume 5 μL) for 30 min at room temperature. Glycerol was also used, as a more viscous solvent, in order to slow down the diffusion of porphyrin molecules and allow for longer interaction times with the particle's surface, consequently, increasing the probability to be detected fluorescence enhancement.

2.7.2.2 Gold nanorods functionalized with Dengue virus ss-DNA analogue sequence

Gold nanorods were functionalized with thiolated Dengue virus ss-DNA analogue sequence. The DNA coating on the rod's surface promotes its interaction with TMPyP molecules and extends the residence time on the particle's surface, thereby increasing the probability to detect fluorescence enhancement. Functionalization of glass-immobilized gold nanorods was performed at room temperature by placing a small droplet of thiolated ss-DNA

oligonucleotide in PBS buffer solution with concentration of 100 nM (volume 5 μL) for 30 min at room temperature. After measuring washing away the DNA solution thoroughly, it was replaced with a TMPyP solution in PBS buffer solution with concentrations of 20 nM. At this porphyrin concentration, approximately 30 molecules are present in the focal volume.

2.7.2.3 Gold nanorods functionalized with Dengue virus ds-DNA analogue sequence

Functionalization of glass-immobilized gold nanorods system was also performed with a Dengue virus ds-DNA analogue sequence. This functionalization was performed at room temperature by placing a small droplet of thiolated ds-DNA solution in PBS buffer with a concentration of 100 nM (volume 5 μL) for 30 min at room temperature. After washing away the DNA solution, thoroughly, it was replaced with a TMPyP solution in PBS buffer with concentrations of 20 nM. At this porphyrin concentration, approximately 30 molecules are present in the focal volume.

Alternatively, a solution of thiolated Dengue virus ds-DNA(100 nM) was prepared by hybridization of Dengue Virus ss-DNA analogue with its complementary sequence RNA and it was added to a TMPyP solution (20 nM) in PBS buffer at room temperature and left to equilibrate to make a complex solution for 20 min. Functionalization of glass-immobilized individual gold nanorods system was performed at room temperature by placing a small droplet of PBS solution containing the porphyrin-DNA complex for 30 min at room temperature.

2.7.2.4 Gold nanorods functionalized with AUT interaction with TPPS porphyrin

For comparison purposes, we investigated another system comprising glass-immobilized gold nanorods functionalized with a positively-charged coating of 11-amino-1-undecanethiol (AUT), and a negative porphyrin derivative named tetraphenylporphyrin sulfonate (TPPS) that has a similar core structure to TMPyP porphyrin. Functionalization of glass-immobilized individual gold nanorods system was performed at room temperature by placing a small droplet of PBS solution containing AUT (100 nM) for 30 min. After washing away AUT solution, thoroughly, it was replaced with a TPPS solution in PBS buffer solution with concentrations of 10 or 100 nM.

3. Results and Discussion

3.1 Localized Surface Plasmon Resonance Sensing of Streptavidin using Biotin-Functionalized Gold Nanorods

Gold nanorods display two optically active plasmon bands: the longitudinal plasmon band (LPB) and the transverse plasmon band (TPB). The LPB is more sensitive to the local refractive index than the TBP, and it can display a peak wavelength red-shift of several hundred nm per unit of refractive index. Moreover, the site-selective functionalization of plasmon hot-spots with bioreceptors results in sensors with improved response by capturing the target species at the most sensitive regions of the particle. Glass-immobilized gold nanorods were tip-functionalized with thiolated-biotin receptor with a concentration of 1μM. When exposed to streptavidin, the LPB showeda red-shift over time in response to a targetconcentration of 100 nM and 1000 nM, respectively (Fig. 3.1).

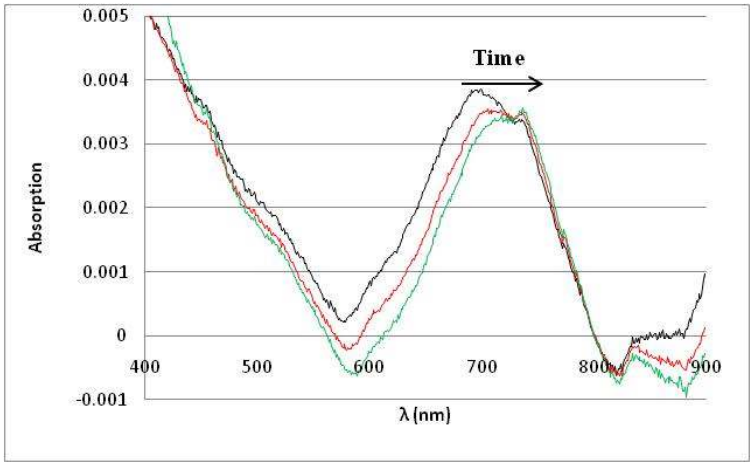

Figure 3.1 (a) Absorption spectra of biotin-functionalized gold nanorods (30 nm × 10 nm) with PEG-4 linker(1 μM) in PBS before binding assay with streptavidin (black curve); (b) the same sample after binding assay with streptavidin solution of 100 nM concentration (red curve),and; (c) after binding assay with streptavidin solution of 1000 nM concentration (green curve) – spectra have been subtracted froman offset.

The kinetic curve from a binding assay of biotin-functionalized gold nanorods with a streptavidin solution with 100 nM concentration show the gradual change in the LPB position over time (Figure 3.2 A). As it can be seen, firstly, there is a red shift in the LPB peak

wavelength and, after some minutes, the peak shift slows down andeventually it stabilizes meaning thata dynamic equilibrium has been established between free and bound streptavidin.

In the second kinetic binding assay, the concentration of streptavidin protein increased to 1000 nM (Figure 3.2 B). Plasmon bond shows more rapidly red shift when the protein concentration increases from 100 nM to 1000 nM because unsaturated biotin receptors binds immediately with more available target protein near the surface of gold naorods on the glass. The kinetic results are approximately exponential at low protein concentration (100nM), but for higher concentration of streptavidin (1000 nM) shows considerably deviation from first order kinetics that can be explained by the mass transition reason. It means because of higher protein concentration at which diffusion becomes efficient to deliver it to the surface on the time interval of our assays.

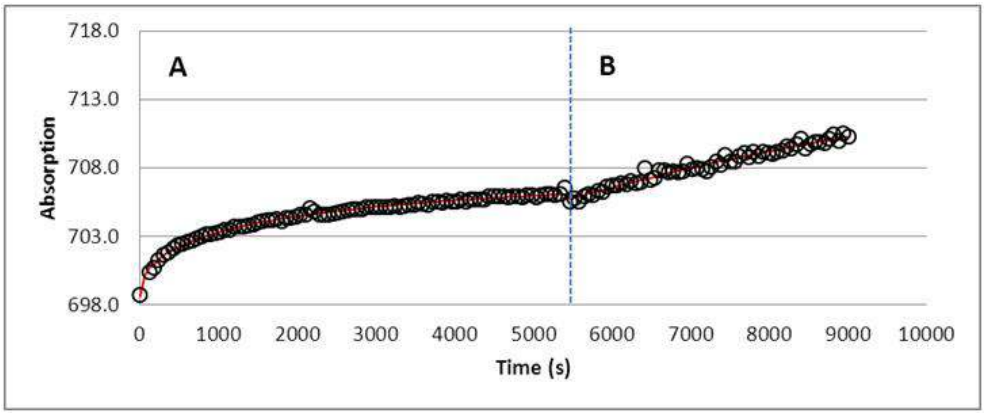

Figure 3.2 A) Binding kinetic curve of biotin-functionalized gold nanorods (30 nm × 10 nm) with PEG-4 linker (1 μM) with streptavidin solution 100 nM (black symbols) and fitted curve using a stretched-exponential (red color); B) Binding kinetic curve after increasing streptavidin concentration to 1000 nM (black symbols).

3.1.1 Localized Surface Plasmon Resonance Sensing of Streptavidin using Bare Gold Nanorods

In the same conditions, a kinetic assay was performed to monitor binding of streptavidin to bare gold nanorods. The LPB showed a peak shift of about 1.5 nm, which is significantly smaller when compared to the peak shift for biotin-functionalized gold nanorods. It can be concluded from this control experiment that the localized surface plasmon response obtained in biotin-functionalized nanorods corresponds to specific adsorption mediated by the strong

biotin-streptavidin interactions, while in bare nanorods, the measured response is only that from non-specific adsorption of strepatvidin on the particle's surface.

3.1.2 The Effect of Biotin Receptor Density in the Plasmonic Sensor Model

The effect of biotin density on the localized surface plasmon peak shift of gold nanorods was investigated by using different concentration of the PEG-4 linker (1µM, 10µM, and 100µM) in the functionalization step of the tip-specific procedure.The gold nanorods functionalized under different biotin concentrations were used to sense two concentrations of streptavidin, 100 nM and 1000 nM, during 90 min and 60 min respectively. Each transmission spectrum in a time series was fitted with a Gaussian function to find the peak wavelength. The final localized surface plasmon (LSP) peak shift was calculated from the difference between the value at the end of the kinetic assay and the initial peak position.The error bars represent the standard deviation for at least three independent bindingassays for a streptavidin concentration of 100 nM and for at least two or three independent assays for a concentration of 1000 nM (Table3.1). The complete set of kinetic curves of the 9 samples and table of results are presented in the Annex A.

Table 3.1 Plasmon peak shifts with standard deviations for streptavidin sensing with gold nanorods functionalized with different concentration of PEG-4 linker

		ΔλLSPR	SD	ΔλLSPR	SD
Sample	PEG-4 (mM)	SA. 100nM	+/-	SA. 1000nM	+/-
1	1				
2	1				
3	1	9	1	12	1
4	10				
5	10				
6	10	10.4	0.2	12	1
7	100				
8	100				
9	100	11	0.8	14	1

In this experiment, the effect of biotin density on plasmon response of gold nanorods functionalized with biotin was followed by using different concentration of the PEG-4 linker (1µM, 10µM, and 100µM) in the functionalization step of the tip-specific procedure (Fig. 3.3). For this purpose, binding kinetic assays were performed firstly with 100 nM of streptavidin during 90 min.

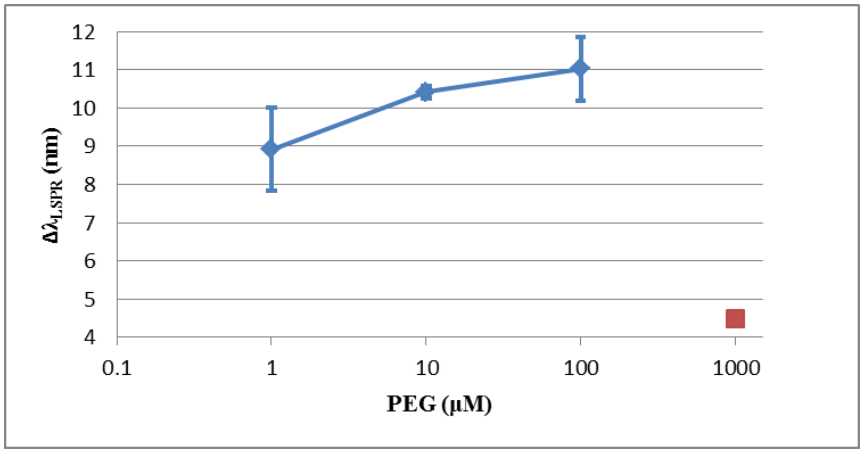

Figure 3.3 Plasmon peak shift for streptavidin sensing with gold nanorods functionalized with PEG-4 versus the linker concentration used in tip-specific functionalization and also for full functionalization, as reported in reference [248]. The error bars represent the standard deviation for at least three independent measurements

In general, the difference of plasmon responses for different concentration of biotin receprtor comprising 1, 10, and 100 µM are not significant. At low concentration of PEG-4 linker (1 µM), the full sensor response is slightly smaller (9$\pm$ 1) because the density of biotin receptors on the gold nanorod is probably lower. When the concentration of PEG-4 linker is 10 µM, the plasmon response shows a slight increase (10$\pm$ 0.2) because morethiolated-biotin receptors are attached onto the rods'surface, thus providing more interaction sites for the protein. At 100 µM concentration of PEG-4 linker, the plasmon response still shows a marginal increment (11.0 $\pm$ 0.8) which suggests that saturation of the rod's surface area for attachment of thiolated-biotin receptor was not yet reached. In order to maximize the sensor response regarding the biotin receptor density, the optimum concentration of PEG-4 linker in the functionalization step is related to a compromise between the number of biotin receptors per gold nanorod and the emergence of steric hindrance at high biotin densities. In other studies, it has been reported that steric hindrance on plane substrates can significantly decrease the saturation coverage of streptavidin in SAMs of biotin by 1.5 to 4-fold.

The effect of biotin density in plasmonic sensor model was also studied in the presence of 1000 nM concentration of streptatvidin target for 60 mins (Figure 3.4).

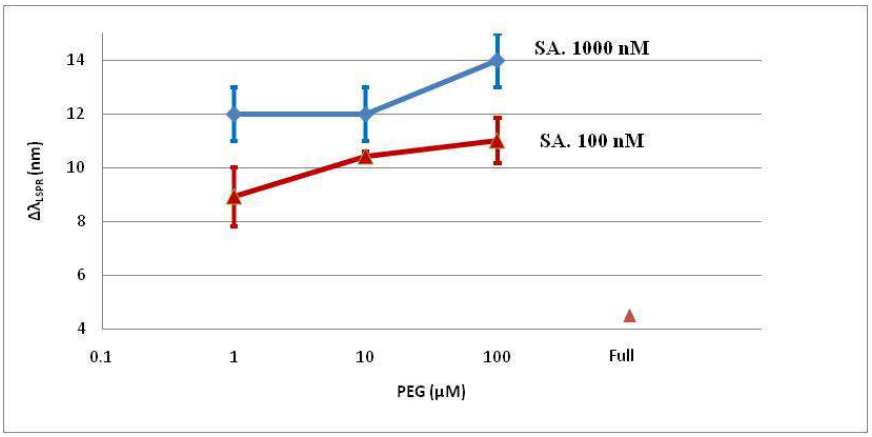

Figure 3.4 Plasmon peak shift for streptavidin sensing with gold nanorods functionalized with PEG-4 versus the linker concentrations used in tip-specific functionalization and also for full functionalization, as reported in reference [248], The error bars represent the standard deviationfor at least two or three independent measurements.

As it can be seen in Figure 3.4, the plasmon response in presence of 1000 nM of streptavidin is higher than response obtained in the presense of 100 nM (Figure 3.3), which means that biotin receptors are not saturated at streptavidin concentration of 100 nM. It also can mentioned, that at higher protein concentration, the diffusion becomes more efficient to deliver it to the surface on the time interval of assays. However, when the concentration of PEG-4 linker, increases from 1µM to 10 µM, almost no change is observed in the peak position of the plasmon band for sensing of 1000 nM of streptavidin. It is hypothesized that steric hindrance due to interaction between binding sites does not allow for more streptavidin molecules to come near and bind to biotin receptors at the rod's surface. However, this does not seem to be the case as there is still an increase of plasmon response (14$\pm$ 1) when the PEG-4 concentration is increased to 100 µM. This result suggests that because of the sparse density ofbiotin linkers in tip functionalization, it probably still allows for more streptavidin to approach the rod's surface and to interact with biotin, thus leading to an increase in plasmon response.

The sensor performance based on tip functionalization of gold nanorods with biotin was compared to results of full functionalization of gold nanorods in the same conditions, as reported in reference [248]**.** The bindingkinetic assays of streptavidinonto fully functionalized gold nanorods with thiolated-biotin have shown peak shits of about 5 nm, which suggest that molecular packing of biotin receptor on the gold nanorod prevents the streptavidin protein to interact with biotin on the rod's surface. This comparison clearly demonstrates that tip-

functionalized rods have a better sensor performancerelatively to fully functionalized rods, which indicates that position and density of bio-receptors are important variables in the design of plasmonic sensors.

3.2 Interaction of Dengue Virus DNAand $TMPyP^{+4}$ in solution

3.2.1 Single-strand Dengue Virus DNA oligonucleotide

A series of solutions containing a single strand Dengue Virus DNA oligonucleotide and TMPyP at various concentrations for DNA-to-porphyrin ratios of 0.02, 0.01, 0.1, 0.2, 0.5, 1, 2 were prepared in PBS buffer solution (1mM, PH 7.0), and allowed to stabilize at room temperature for 20 min. The absorption spectra of these solutions were measured in the range of 220-850 nm at a speed rate of 240nm/min (Figure 3.5, 3.6).

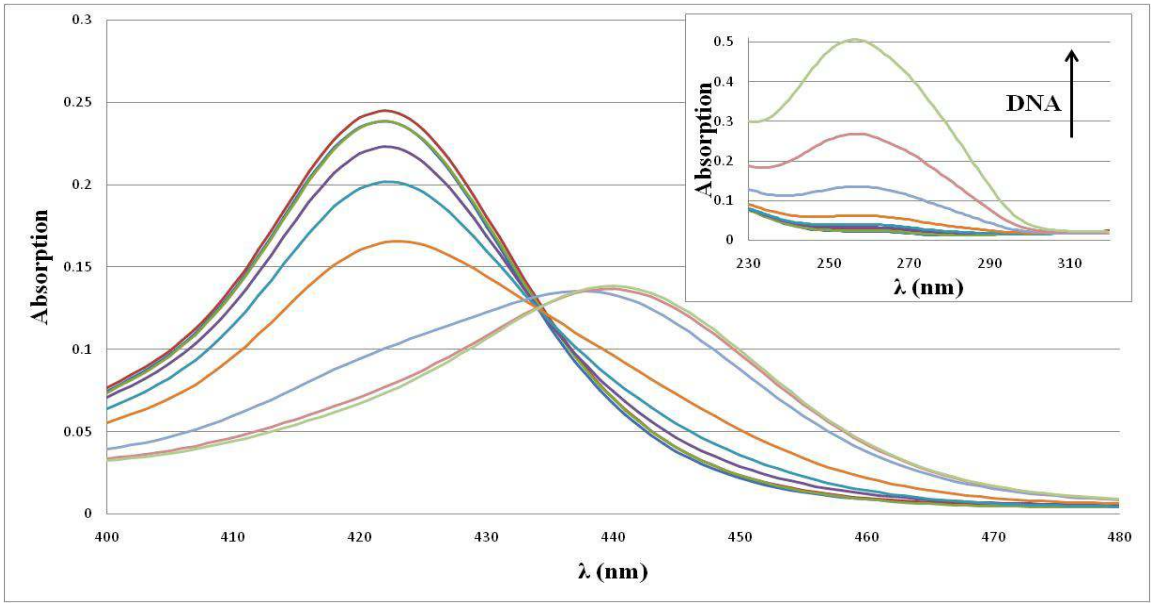

Figure 3.5 Absorption spectra in the Soret band region of TMPyP in the presence of Dengue Virus ss-DNA oligonucleotidefor concentration ratios of 0.02, 0.01, 0.1, 0.2, 0.5, 1, 2 compared to the absorption spectrum of a TMPyP solution with 1μM concentration in PBS buffer solution.

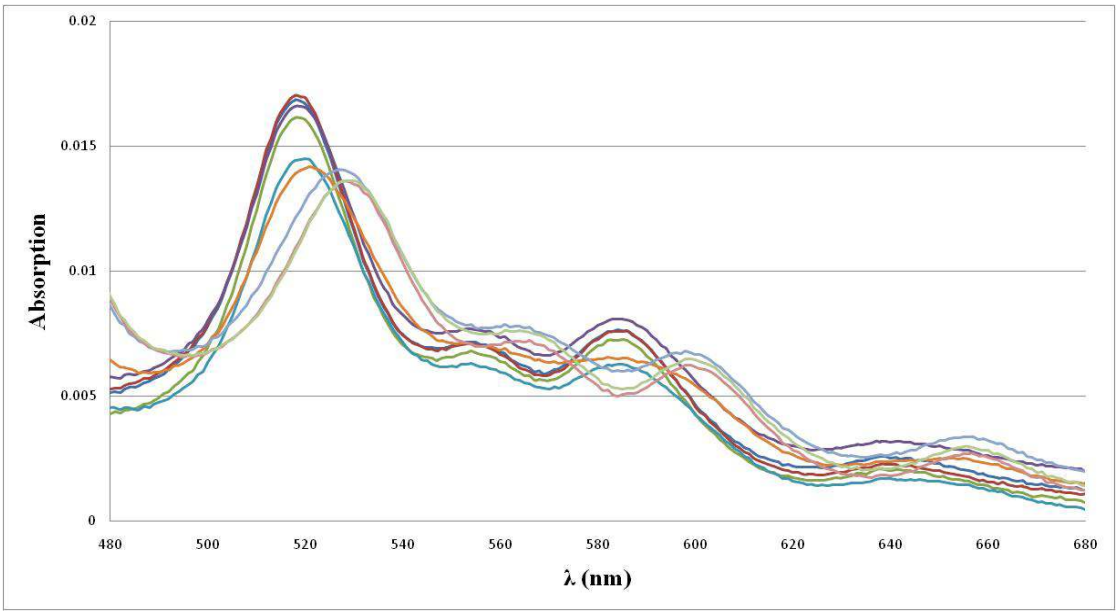

Figure 3.6 Absorption spectra in the Q bands region for TMPyP in the presence of Dengue Virus ss-DNA oligonucleotide for concentration ratios of 0.02, 0.01, 0.1, 0.2, 0.5, 1, 2 compared to absorption spectrum of a TMPyP solution with 1μM concentration in PBS buffer solution.

The absorption spectra of TMPyP alone was measured in buffer solution at the same concentration of the solutions with Dengue Virus to allow for a visual comparison of spectral changes**.** As it can be seen in figures 3.5 and 3.6, TMPyP exhibits an intense Soret band at λ_{max}=421 nm and four weak Q-bonds in range of 480-680 nm.

3.2.2 Double-strand Dengue Virus DNA oligonucleotide

To investigate the interaction of TMPyP with double-strand Dengue virus DNA, in the first place, a solution of single strand Dengue Virus DNA was mixed with its complementary ss-DNA sequence and allowed to hybridize at room temperature for 20 min. Then, it was prepared a series of solutions with varying concentration ratios of DNA-to-porphyrin (0.02, 0.01, 0.1, 0.2, 0.5, 1, 2) that were allowed to stabilize also at room temperature for 20 min. After this time, the absorption spectrum of those solutions was measured (Figure 3.7, 3.8).

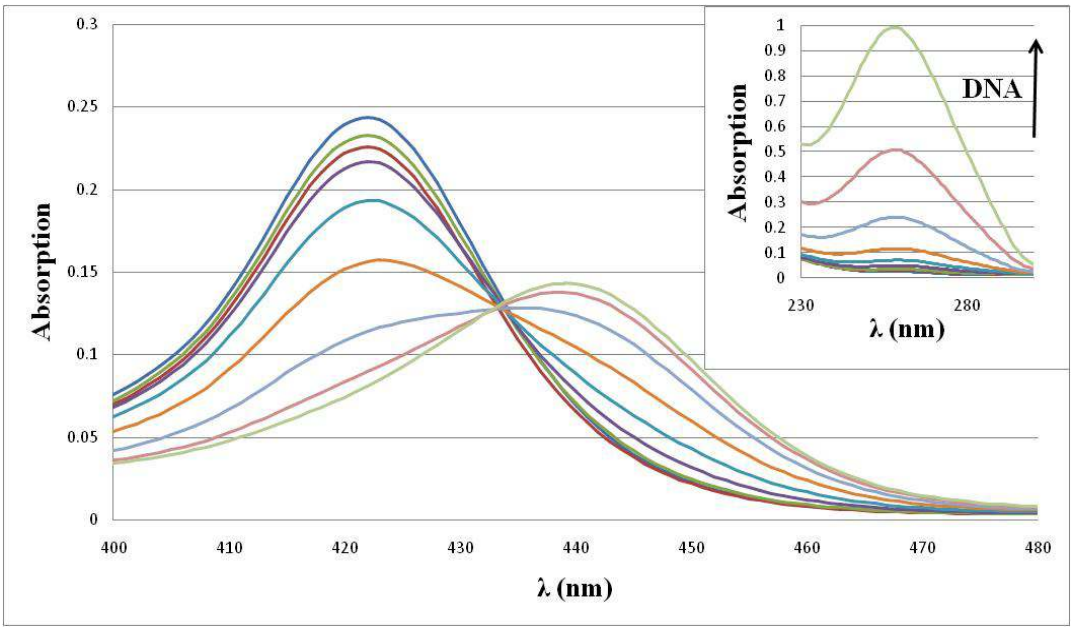

Figure 3.7 Absorption spectra in the Soret band region of TMPyP in the presence of Dengue Virus ds-DNA for concentration ratios of 0.02, 0.01, 0.1, 0.2, 0.5, 1, 2 compared to absorption spectrum of a TMPyP solution with 1μM concentration in PBS buffer solution.

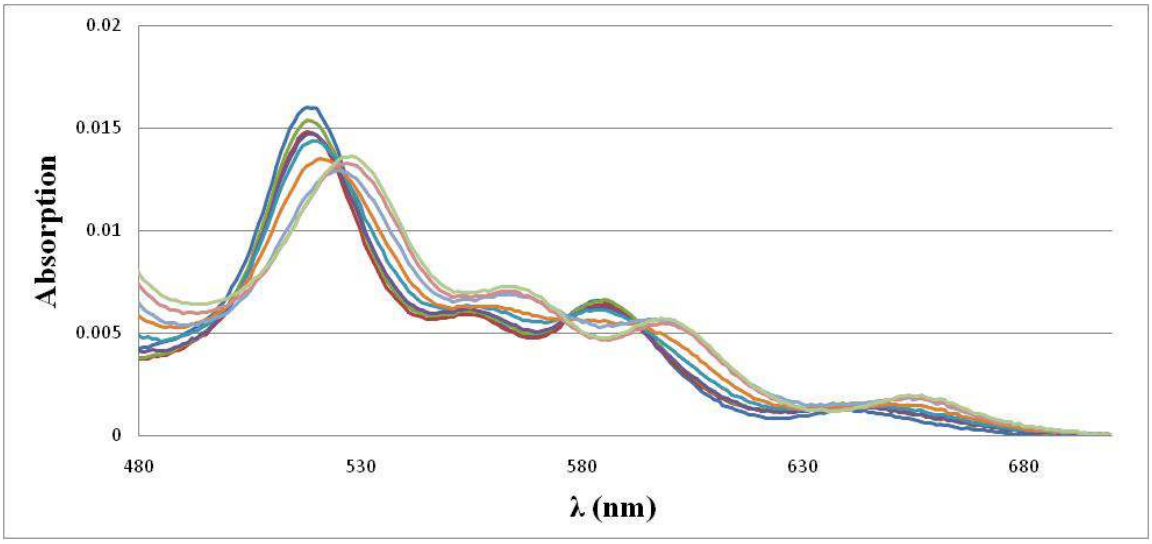

Figure 3.8 Absorption spectra in the Q-bands' region of TmPyP in the presence of Dengue Virus ds-DNA at concentration ratios of 0.02, 0.01, 0.1, 0.2, 0.5, 1, 2 compared to absorption spectrum of a TMPyP solution with 1μM concentration in PBS buffer solution.

The interaction between ds-DNA and TMPyP shows an isobestic point that indicates the existence of an equilibrium between free prophyrin and a complexed form with ds-DNA.

Based on a simple 1:1 association model, it was fitted an apparent equilibrium constant with a value around 10 $^{7}M^{-1}$, which shows a strong interaction that most likely it is an intercalation type of binding occurring between DNA and TMPyP.

There are several kinds of interaction forms between porphyrin and DNA, which consist of intercalation, outside-binding, and groove binding. For example, the flat porphyrin free-base usually intercalate with DNA containing the GC-rich nucleotide base regions [100], or groove binding typically occurs with AT-rich DNA at low porphyrin-to-DNA base ratio. However, the majority of prophyrins stack outside of the DNA through electrostatic interactions with negatively charged phosphate groups in the DNA backbone.

At low concentration of DNA, for ratios ranging from 0.02 to 0.2, the porphyrin most likely interacts with the outside of DNA which agrees with the small shifts observed in Soret and Q-bands. However, upon increasing the concentration ratio to values from 0.5 to 2, the interaction becomes stronger because of GC-rich sites in the Dengue Virus DNA (almost 50%), and probably intercalation happens, and consequently, obvious clear large shift to longer wavelengths is seen for both Soret and Q- bands.

The fluorescence emission spectra were also measured for these samples (Figure 3.9 and 3.10).

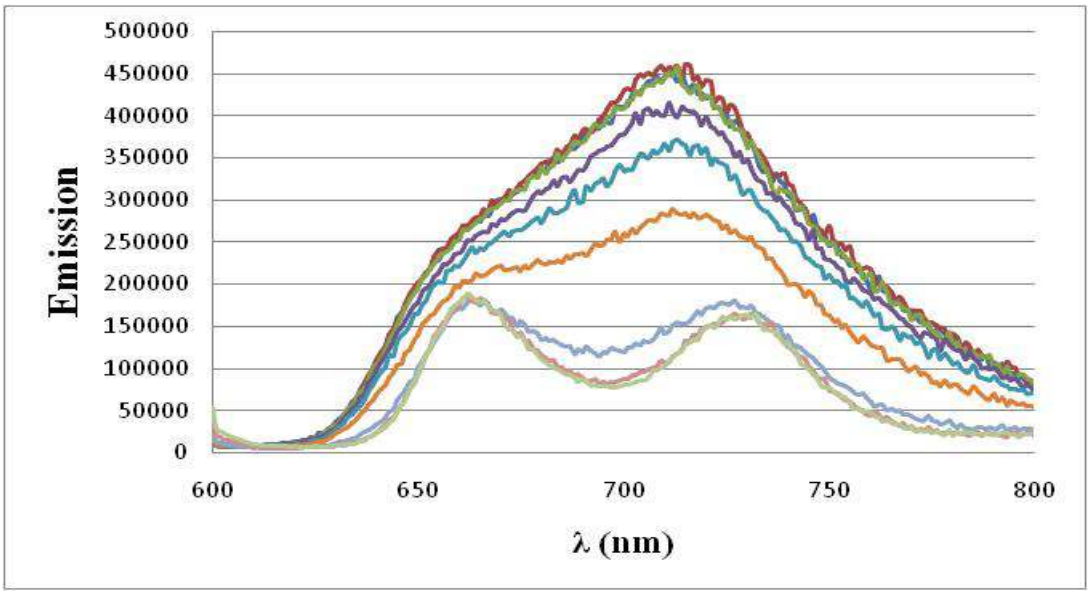

Figure 3.9 Emission spectra excited at 590 wavelength fluorescence emission of TMPyP in the TMPyP-Dengue-ss-DNA solutions with different concentration ratio of 0.02, 0.01, 0.1, 0.2, 0.5, 1, 2 compared to emission spectra of TMPyP solution with 1μM concentration in PBS buffer solution.

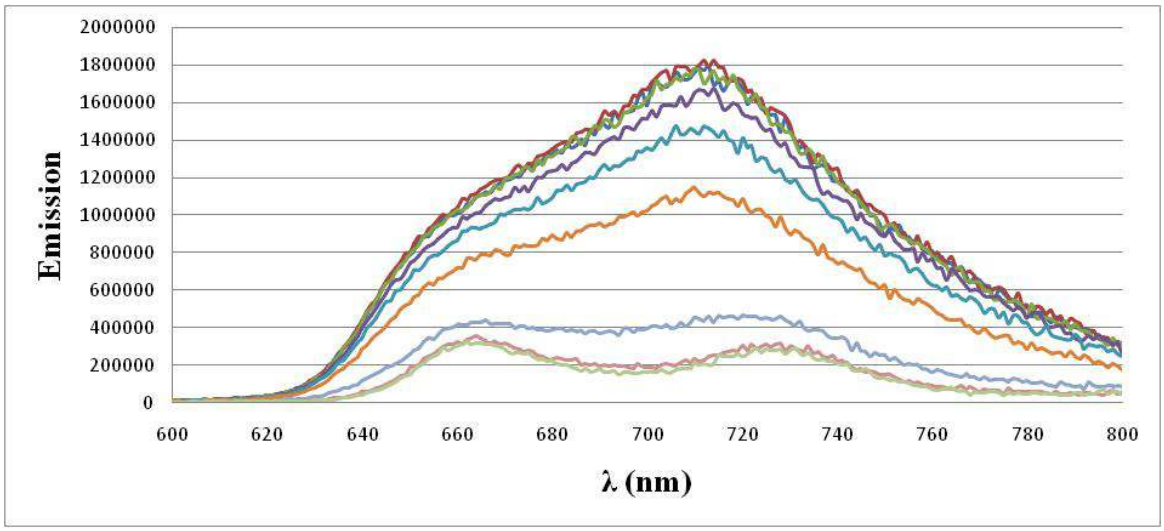

Figure 3.10 Emission spectra excited at 410 wavelength fluorescence emission of TmPyP in the TMPyP-Dengue-ss-DNA solutions with different concentration ratio of 0.02, 0.01, 0.1, 0.2, 0.5, 1, 2 compared to emission spectra of TMPyP solution with 1μM concentration in PBS buffer solution.

Based results obtained from fluorescence emissions of single standard Dengue DNA and TMPyP soultions, the emission spectra of TMPyP changed significantly with increasing the concentration ratio. As it can be seen in the emission spectra of the vibrational structure of TmPyP is strongly masked because of band broadening and the Q(0.0) emission band observed as a shoulder relative to the more intense Q(0.1) bond. It can be suggested mixing S1 state of TMPyP protein with a nearby charge-transfer (CT) mediated by the librational motion of pyridinium groups in TmPyP. So, the CT state is destabilized, precluding its electronic coupling with the first excitation state (S1). A strong fluorescence quenching effect was observed for TmPyP with Dengue Virus DNA in ratio concentrations of 1 and 2. Moreover, an obvious increasing in the vibronic definition of the spectrum was obtained (Figure 3.9, 3.10).

Similar approaches have been taken to investigate for double standard Dengue DNA and TMPyP solutions (Figure 3.11, 3.12).

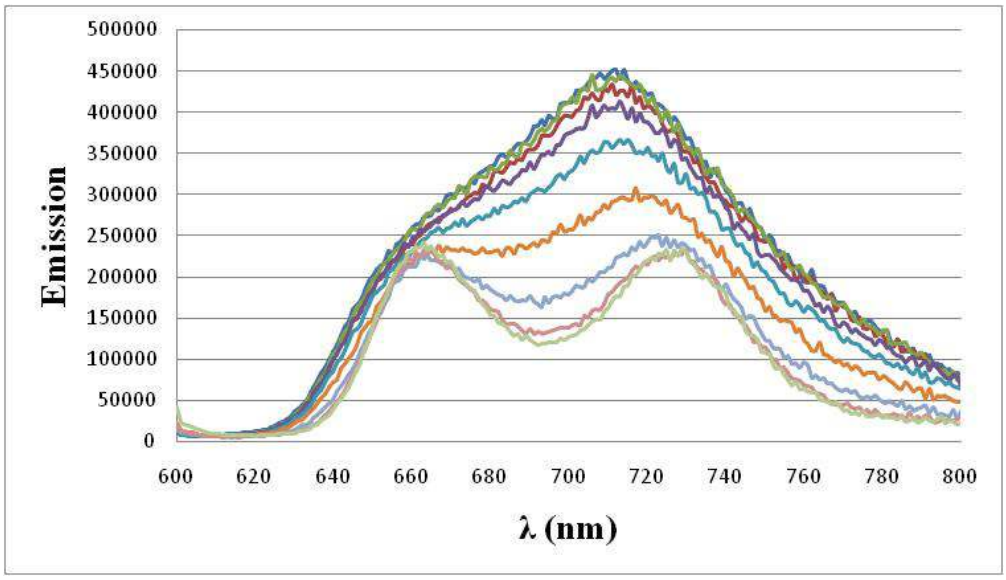

Figure 3.11 Emission spectra excited at 590 wavelength fluorescence emission of TMPyP in the TMPyP-Dengue-ds-DNA solutions with different concentration ratio of 0.02, 0.01, 0.1, 0.2, 0.5, 1, 2 compared to emission spectra of TMPyP solution with 1μM concentration in PBS buffer solution.

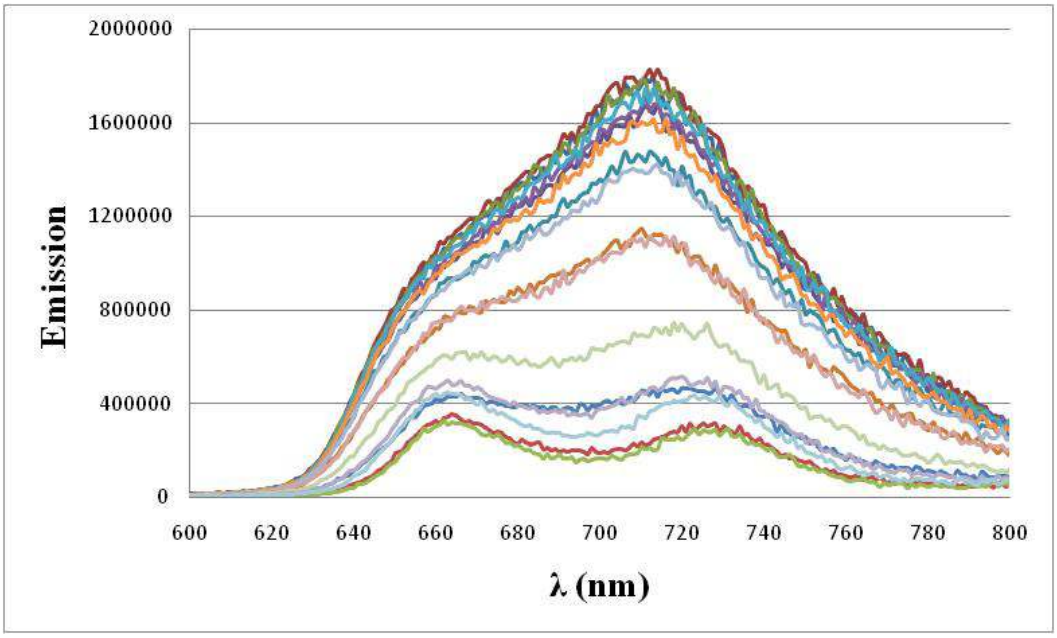

Figure 3.12 Emission spectra excited at 410 wavelength fluorescence emission of TMPyP in the TMPyP-Dengue-ds-DNA solutions with different concentration ratio of 0.02, 0.01, 0.1, 0.2, 0.5, 1, 2 compared to emission spectra of TMPyP solution with 1μM concentration in PBS buffer solution.

3.2.3 Determination of association constant of TMPyP with Dengue Virus DNA

The absorbance of sample solutions at 260 nm versus the DNA concentrations shows linearity as expected from the fact that at this wavelength light absorption is mostly due to DNA and it follows Lambert-Beer law.

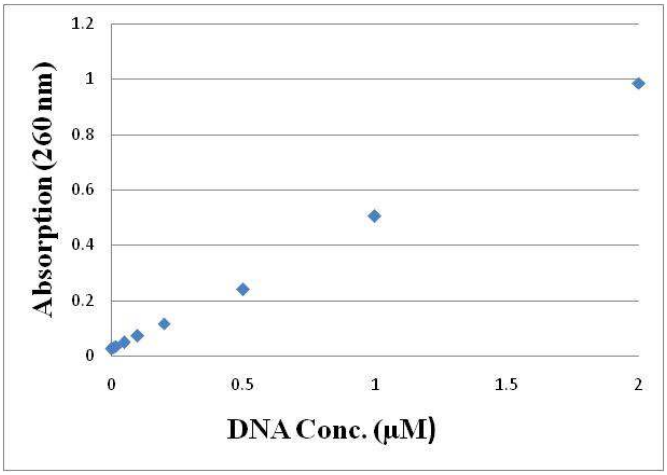

Figure 3.13 Absorbance at 260 nm versus the DNA concentration in Dengue-ds-DNA solutions with TMPyP at different ratios of 0.02, 0.01, 0.1, 0.2, 0.5, 1, 2.

The absorbance at 420 nm and 440 nm versus the DNA concentration in Dengue-ds-DNA solutions with TMPyP, at different ratios of 0.02, 0.01, 0.1, 0.2, 0.5, 1, 2 (Fig. 3.14), shows the conversion from free TMPyP to the DNA-complexed form. The apparent binding constant was calculated from an association model based on a 1:1 chemical equilibrium between free and DNA complexed forms of TMPyP (red symbols in Fig. 3.14). The apparent equilibrium constant was calculated to be $K_a = 4.53 \times 10^7\ M^{-1}$. Moreover, based on the literature [249], this value of the equilibrium constant shows an intercalation of TMPyP with ds-DNA at these concentrations. The apparent equilibrium constant was also calculated for the Dengue-ss-DNA to be $K_a = 3.90 \times 10^7\ M^{-1}$ (Figure 3.15)

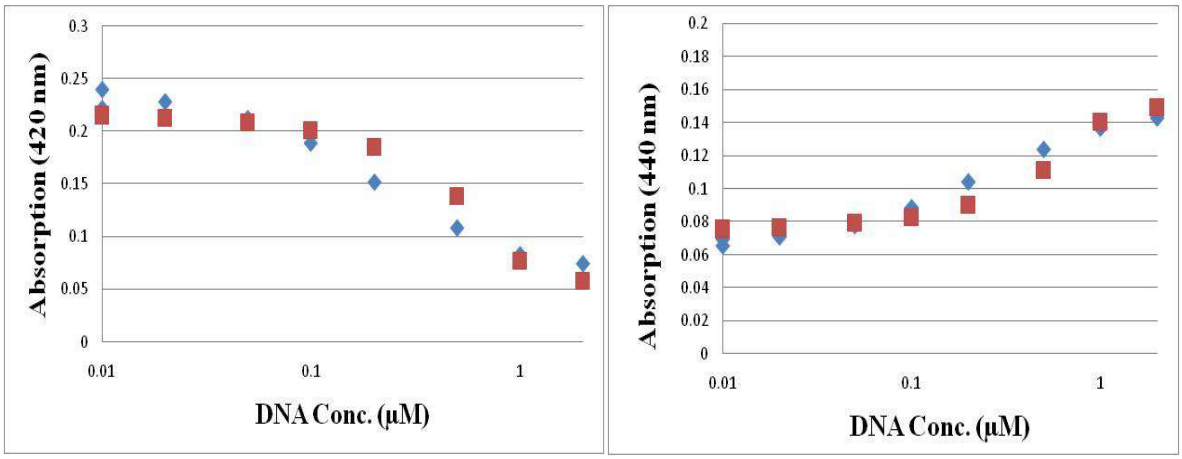

Figure 3.14 Absorbance at 420 nm and 440 nm versus the DNA concentration in Dengue-ds-DNA solutions with TMPyP at different ratios of 0.02, 0.01, 0.1, 0.2, 0.5, 1, and 2.

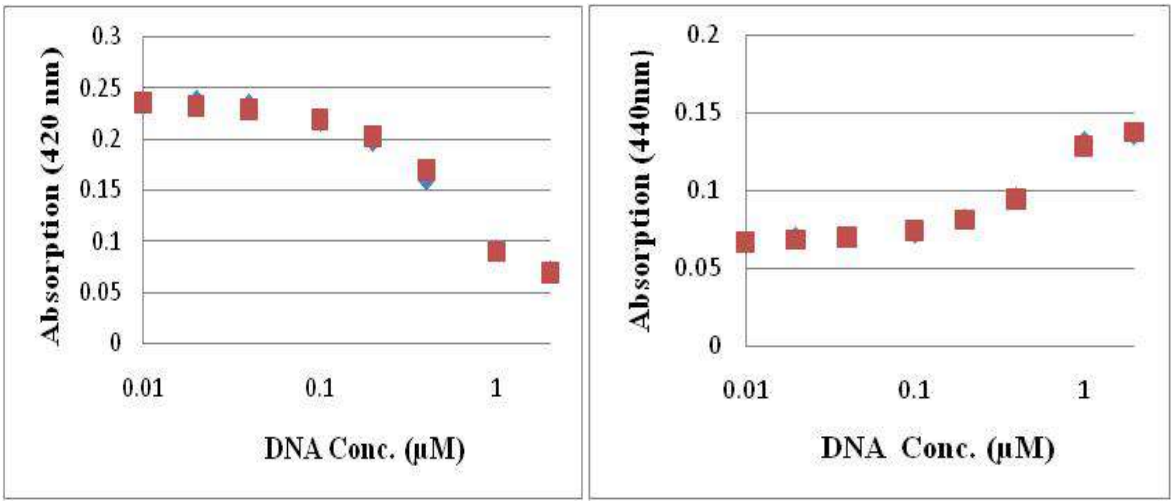

Figure 3.15 Absorbance at 420 nm and 440 nm versus the DNA concentration in Dengue-ss-DNA solutions with TMPyP at different ratios of 0.02, 0.01, 0.1, 0.2, 0.5, 1, and 2.

3.2.4 Time-Resolved Optical Spectroscopy of TMPyP interaction with Dengue Virus DNA in solution

The interaction of TMPyP with Dengue-ds-DNA in solution results in a longer lifetime component of 10.3 ns, when compared to its complex with ss-DNA (8.6 ns), and both complexes have a longer decay component than free TMPyP in solution (5.7 ns) because of the specific interactions occur between ds- and ss-DNA analogue sequences from Dengue Virus with TMPyP (Table 3.2 and Figure 3.16).

Table 3.2 Comparison of fluorescence life time decay of free TMPyP solution with complex-ss-DNA-TMPyP and complex-ds-DNA-TMPyP in solution.

System	Life Time 1 (Percentage)	Life Time 2 (Percentage)	Life Time 3 (Percentage)
$TMPyP^{+4}$ (1μM) in solution	5.7 ns (42.7%)	2.3 ns (53.9%)	0.1 ns (3.4%)
Complex-ds-DNA-TMPyP in solution	10.3 (36.9%)	3.5 (52.6%)	0.58 (10.5%)
Complex-ss-DNA-TMPyP in solution	8.6 (32.9%)	3.0 (53.3%)	0.58 (13.8%)

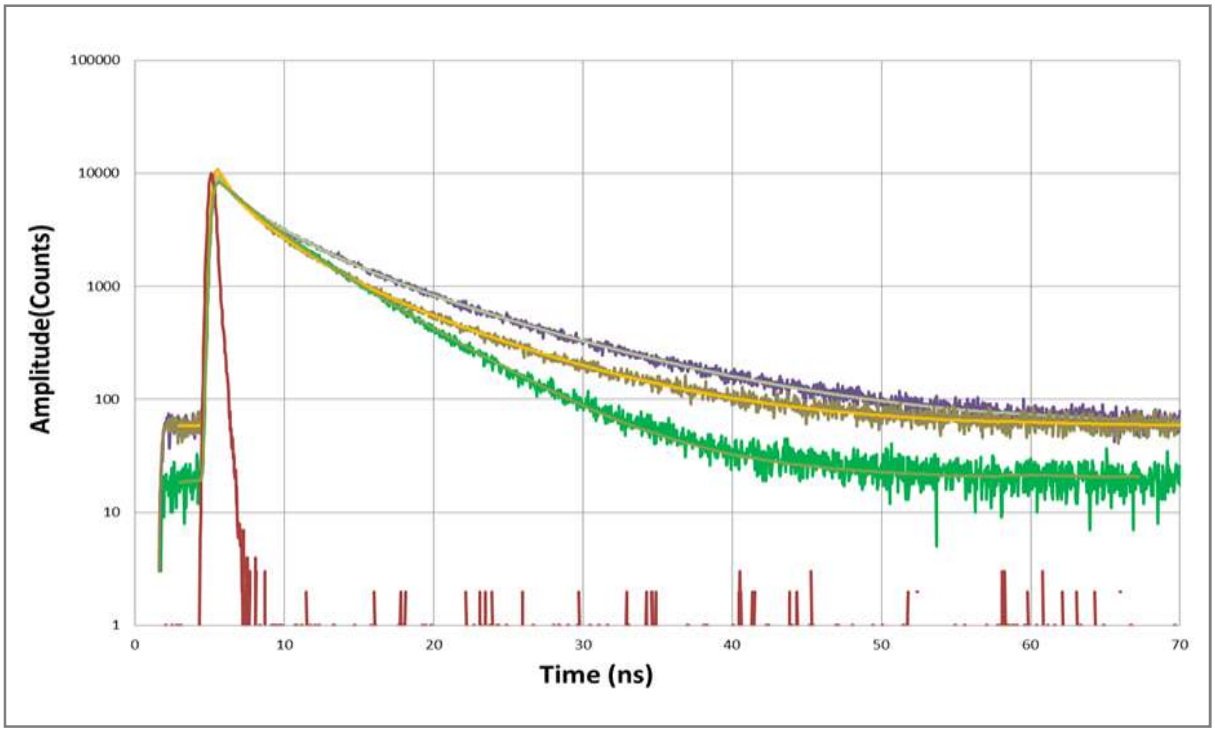

Figure 3.16 Comparison of Fluorescence life time decay of TMPyP in solution (green), Complex-ss-DNA-TMPyP in solution (orange), Complex-ds-DNA-TMPyP in solution (gray)

3.3 Functionalization of Gold Nanorods with DNA Probe for Dengue Virus RNA sensing

3.3.1 Tip Functionalization of Gold Nanorods with DNA Probe for Dengue Virus RNA sensing

Based on the model sensor of tip-functionalized gold nanorods, the same procedure was used for attaching a thiolated ss-DNA probe sequence to the tips of gold nanorods immobilized at a glass surface.

The gold nanorods were first functionalized with a thiolated ss-DNA (10 μM) in the presence of CTAB surfactant (1 mM). Then, the tip-functionalized gold nanorods were exposed to the complementary RNA sequence from Dengue virus (100, and 1000 nM), which is labeled with a biotin. The rationale for this model sensor is that hybridization increases the thickness of the nucleic acid layer at tips of gold nanorods, thus increasing the local refraction index and causing a red shift of the plasmon peak that is used to signal the molecular recognition of the target sequence. The biotin label on the target sequence provides a way to amplify the sensor response, in the case of a successful hybridization, by allowing the binding of a large bio macromolecule, such as streptavidin or anti-biotin antibody (Figure 3.19, A).

A control experiment was carried out by preparing tip-functionalized gold nanorods and performing the biosensing assay with anon–complementary DNA sequence (100, and 1000 nM) instead of the target RNA sequence. As it is expected in this case, the hybridization does not occur and any red-shift observed in the plasmon peak results from non-specific interactions with the glass-immobilized gold nanorods (Figure 3.18, B).

The initial step of tip functionalization with ss-DNA probe induced large plasmon peak shifts of 19.1 nm (Figure 3.17 , A) and 27 nm (Figure 3.18, A), even after washing the samples in PBS for 5 hours and drying. We notice that these plasmon peak shifts were obtained from spectra measured in air. Next, the tip-functionalized gold nanorods were exposed to solutions of complementary and non complementary sequences during 90 mins (sample and control, respectively). Both assays failed to produce any plasmon peak shift (Figure 3.17, B) and (Figure 3.18, B). Moreover, after adding streptavidin (2000 nM) during 60 mins, in an attempt to amplify the plasmon response, still no plasmon shifts were observed.

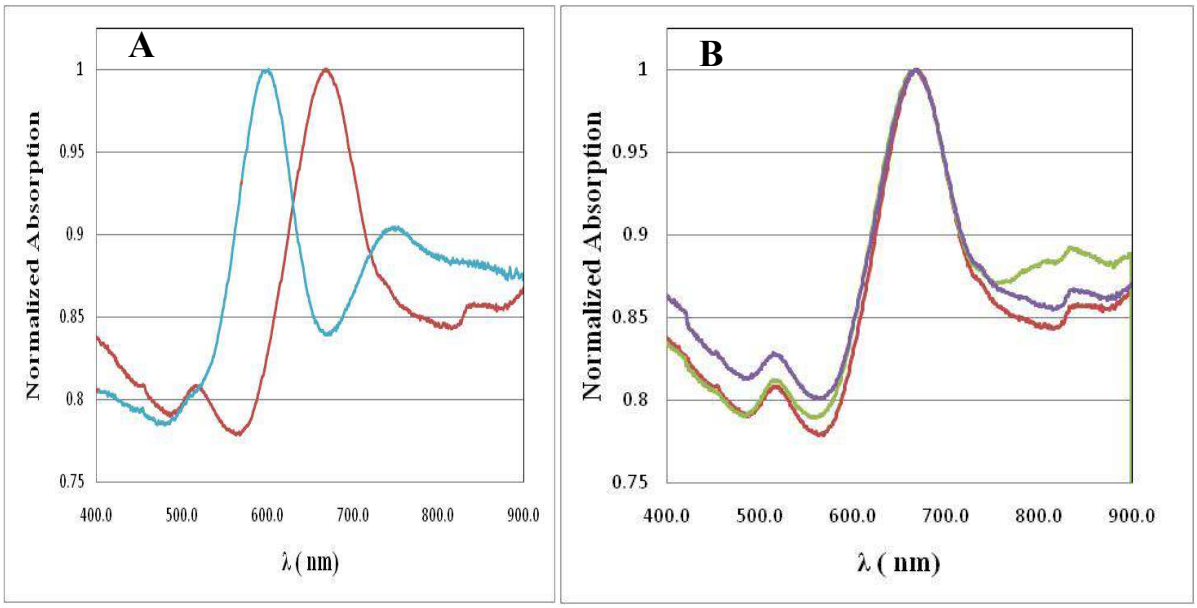

Figure 3.17 A) Tip functionalization of gold nanorods with thiolated ss-DNA probe sequence (blue and red curves are before and after functionalization, respectively, ΔLSPR =19.1 nm) , B) Plasmon peak before adding the target Dengue Virus RNA sequence in PBS solution (red curve), after adding the target sequence(100 nM) (green curve), and after increasing the target concentration (1000 nM) (blue curve), ΔLSPR =0.

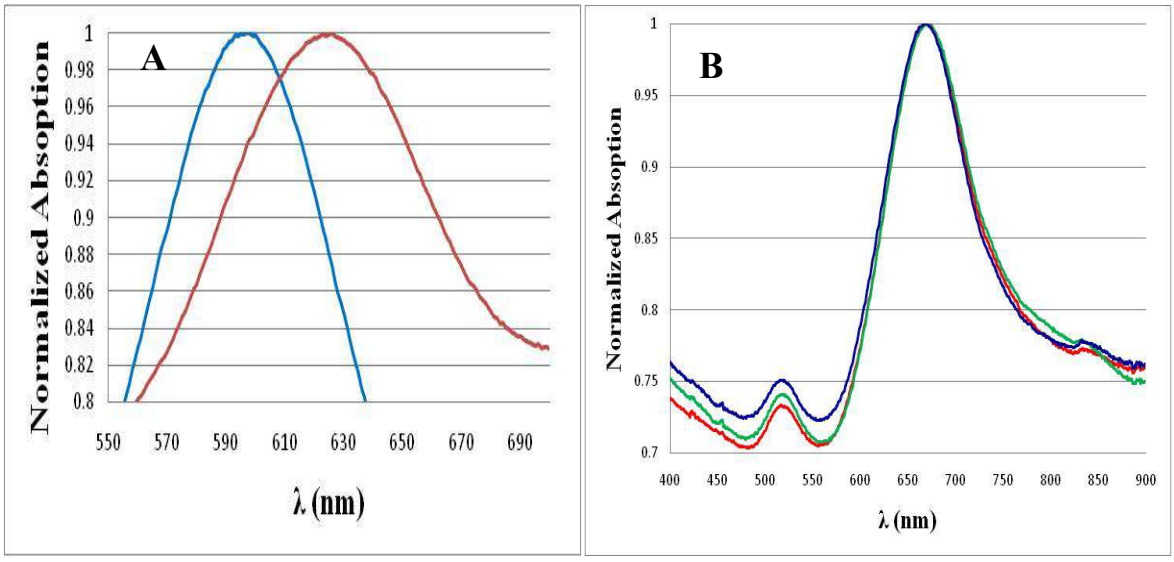

Figure 3.18 A) Tip functionalization of gold nanorods with thiolated ss-DNA probe sequence (blue and red curves are before and after functionalization, respectively, ΔLSPR =28 nm) , B) Plasmon peak before adding the target Dengue Virus RNA sequence in PBS solution (red curve), after adding the target sequence (100 nM) (green curve), and after increasing the target concentration (1000 nM) (blue curve), ΔLSPR =0.

In an attempt to explain the observed results, we speculate that CTAB makes a positive charge bilayer, while DNA has negative charge, and they can strongly interact by electrostatic attraction and make a thick layer on the surface of gold nanorod, thereby causing a large red shift in the plasmon peak, even though the surfaces were washed in PBS solution for 5 hours (Figure 3.19, B). Consequently, adding the complementary sequence during 90 mins does not influence the plasmon peak wavelength, as well as incubating in streptavidin, because of steric hindrance from aggregated CTAB molecules on the probe DNA layer.

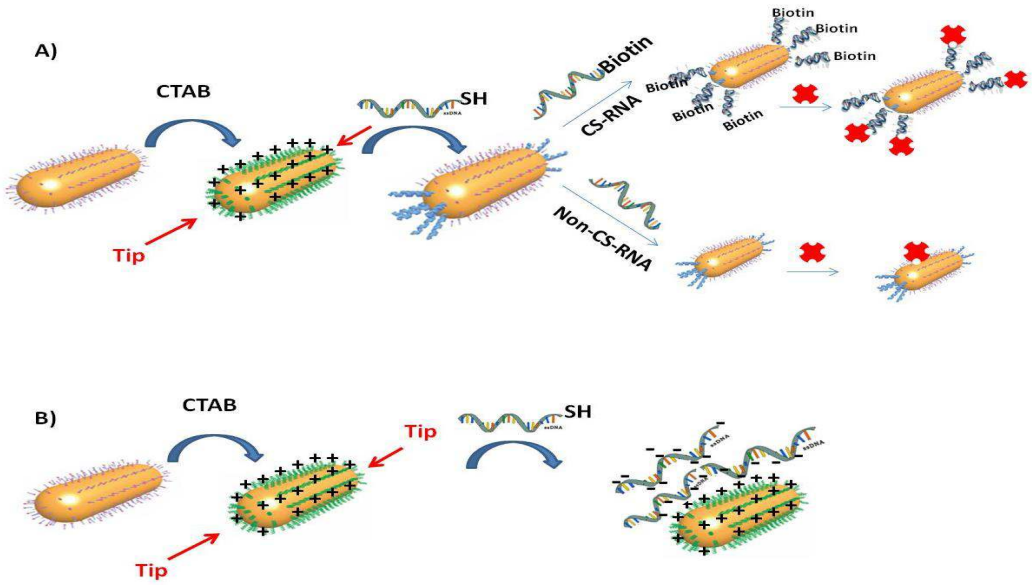

Figure 3.19 A) The proposed biosensor system for tip functionalization of gold nanorods with a thiolated ss-DNA probe sequence using a CTAB protective layer. Then, it is shown the hybridization with a biotin-labeled target RNA sequence from Dengue virus and amplification through binding of streptavidin, B) The CTAB makes a positive charge bilayer and the electrostatic attraction between CTAB and negatively charged DNA makes a thick layer on the surface of the gold nanorod.

3.3.2 Full Functionalization of Gold Nanorods with DNA Probe for Dengue Virus RNA sensing

In order to overcome the problems mentioned in the previous section, the glass-immobilized gold nanorods were fully-functionalized with thiolated ss-DNA probe sequences. A significant plasmon peak red shift of 7.8 nm was obtained for full-functionalization with thiolated ss-DNA probe sequences with a concentration of 10 µM (Figure 3.20, A). Besides, the full functionalization at different concentrations of ss-DNA probe of 0.1 and 1µM was

also tested. For both concentrations, there was no change in plasmon peak wavelength. Only full functionalization with a ss-DNA concentration of 10 µM showed a plasmon red-shift.

Two replica surfaces were prepared to be used as sample and control. The first surface of DNA-functionalized gold nanorods was exposed to complementary RNA sequence from Dengue virus (100 and 1000 nM). After adding complementary sequence RNA (100 nM) during 90 mins, following by a concentration increase to1000 nM during 60 mins, there was no red shift observed in plasmon peak. (Figure 3.20, B)

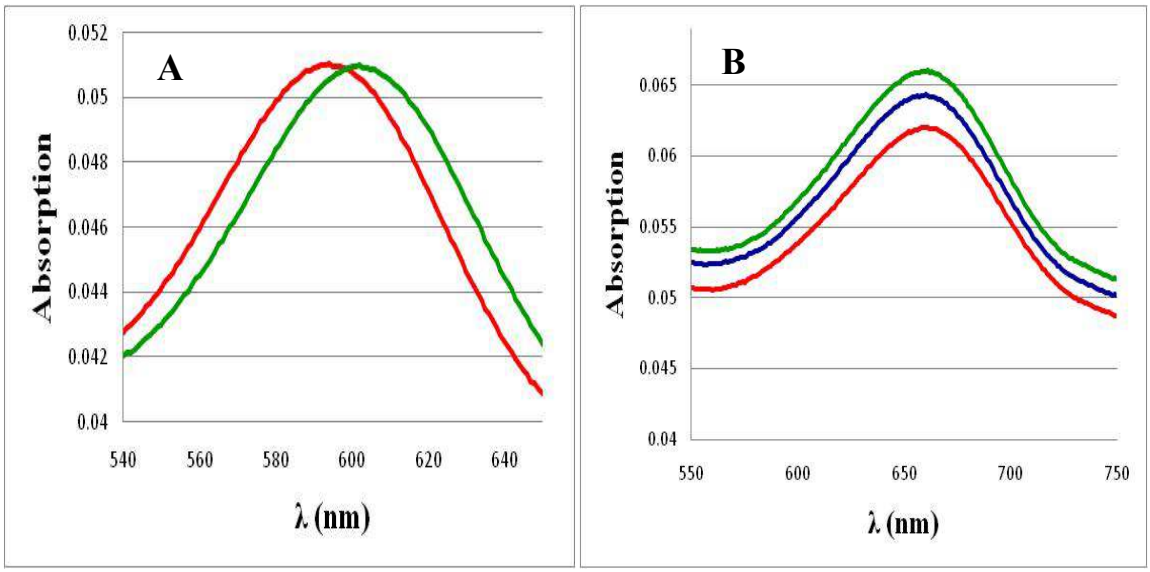

Figure 3.20 A) Full functionalization of gold nanorods with thiolated ss-DNA probe sequence (red and green curve is before and after functionalization, respectively), ΔLSPR =7.8 nm, B) Plasmon peak before adding complementary Dengue virus target RNA in PBS buffer solution (red curve), after adding target sequence (100 nM) (green curve), and after increasing concentration of target sequence (1000 nM) (blue curve).

Figure 3.21 A and B, show results from binding kinetics assays for hybridization sensing. Instead of the expected plasmon red-shift, only blue-shifts were observed: after adding 100 nM of complementary RNA sequence (ΔLSPR = -0.5 nm) and after increasing concentration to 1000 nM (ΔLSPR = -0.3 nm). Figure C, shows the kinetic trace when the same surface was exposed to streptavidin (2000 nM) toward achieving an amplification effect of the LSPR shift having been obtained a shift of 2 nm (Figure 3.21, C).

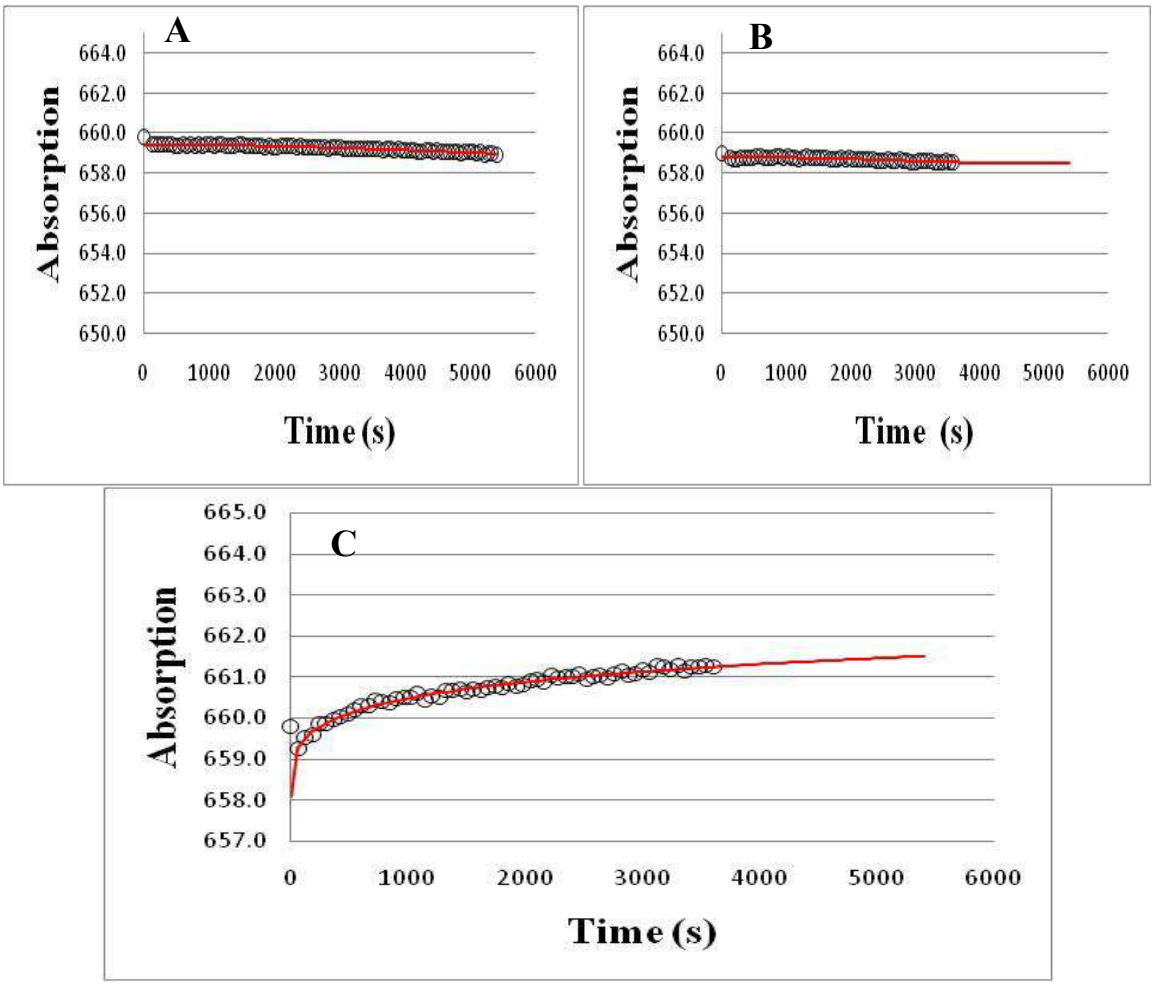

Figure 3.21 A) kinetics assay for hybridization sensing of fully-functionalized gold nanorods with ss-DNA probe upon adding the complementary Dengue virus RNA sequence (100 nM) during 90 mins (ΔLSPR = -0.5 nm) and fitting function (red line), B) kinetics assay after increasing concentration of complementary RNA sequence (1000 nM) during 60 mins (ΔLSPR = -0.3 nm), C) kinetic binding assay upon exposing the previous surface to streptavidin toward signal amplification (ΔLSPR =2 nm).

For the control experiment, a significant shift of 9.1 nm was also observed after full-functionalization (Figure 3.22, A). As it had expected, adding 100 nM of a non-complementary DNA sequence during 90 mins or increasing the concentration to1000 nM produced no shift in the plasmon peak (Figure 3.22, B). The kinetic binding assays show even a slight blue-shift (Figure 3.23). Although, the hybridization is not possible in this case, we have still observed a plasmon red-shift of 2.7 nm for the kinetic binding assay with streptavidin (Figure 3.23, C).

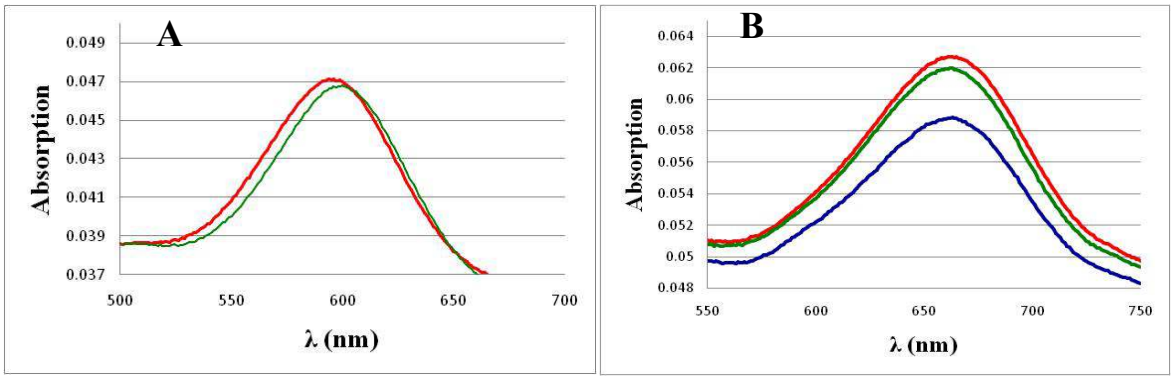

Figure 3.22 A) Full functionalization of GNRs with single strand Dengue Virus DNA receptor (red curve is before functionalization and green curve is after functionalization), ΔLSPR =9.1 nm, B) Plasmon response before adding non-complementary sequence Dengue Virus RNA in PBS buffer solution (red curve), plasmon response after adding non-complementary sequence Dengue Virus RNA (100 nM) (green curve), plasmon response after adding non-complementary sequence Dengue Virus RNA (1000 nM) (blue curve).

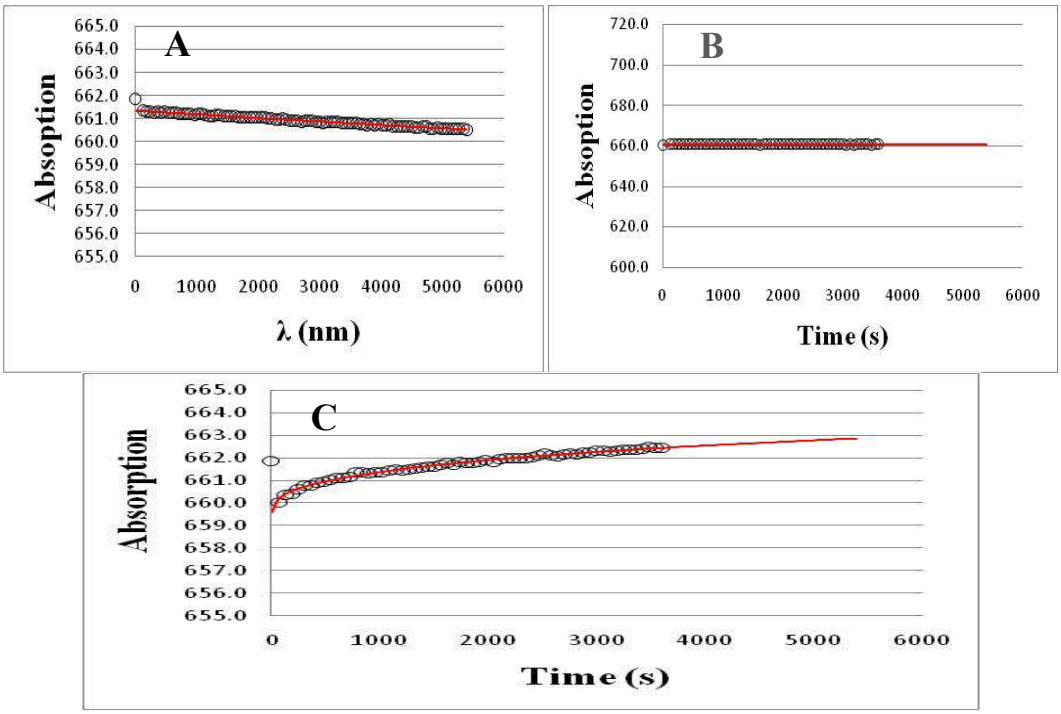

Figure 3.23 A) kinetics assay for hybridization sensing of fully-functionalized gold nanorods with ss-DNA probe upon adding the non-complementary sequence Dengue Virus RNA (100 nM) during 90 mins (ΔLSPR = -0.8 nm) and fitting function (red line), B) kinetics assay after increasing concentration of the non-complementary sequence Dengue Virus RNA (1000 nM) during 60 mins (ΔLSPR = -0.3 nm), C) kinetic binding assay upon exposing the previous surface to streptavidin toward signal amplification (ΔLSPR =2.7 nm).

In an attempt to explain the observed results, we speculate that the full-functionalization can attach non-specifically the ss-DNA probe to the surface of gold nanorod. Consequently, it induces a considerable red shift in the plasmon peak because the ss-DNA chains can interact with each other by hydrogen bonding and form layers of DNA on the gold nanorods' surface that remained even after washing with PBS solution for 3 hours. So, adding the complementary RNA sequence of Dengue virus or a non-complementary sequence did not produce any plasmon responses. Finally, in the biotin-streptavidin assays, since there was no biotinylated nucleic acids specifically attached on the gold nanorods' surface, the streptavin binded non-specifically and gave red-shifts in both the sensing experiment (2 nm) and in its control (2.7 nm) as plasmon response (Figure 3.24).

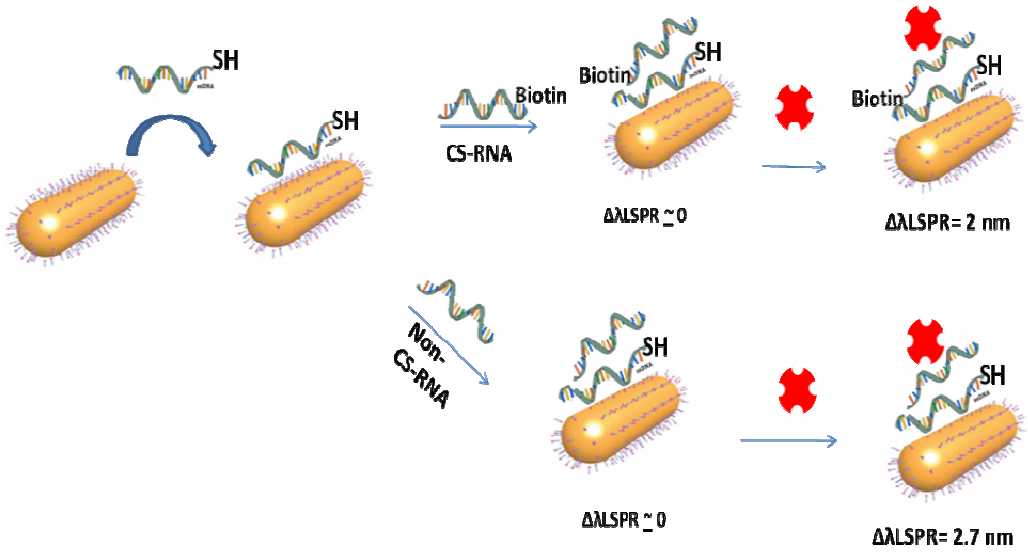

Figure 3.24 The design of our biosensor system for full functionalization of gold nanorods with a ss- DNA probe (binded non-specifically) and plasmonic sensing with complementary RNA sequence from Dengue Virus and a non-complementary sequence, and binding of streptavidin (non-specifically) toward amplification of plasmon response.

3.3.3 Full Functionalization of Gold Nanorods with a mixed monolayer of DNA and PEG-4-SH

Several changes were introduced in order to test the plasmonic response of the model biosensor: i) a mixed monolayer with a thiolated oligo (ethylene glycol) chain with four repeating units (PEG-4-SH) was used to avoid non-specific adsorption of DNA on the gold nanorods; ii) the thiolated ss-DNA probe sequence was previously hybridized with the complementary RNA sequence, and then the hybrid was used for the functionalization of

gold nanorods, and; iii) an anti-biotin antibody was used for testing the plasmon response in the amplification step, because it has more volume when compared to streptavidin and it should provide a larger change in local refraction index (Figure 3.25).

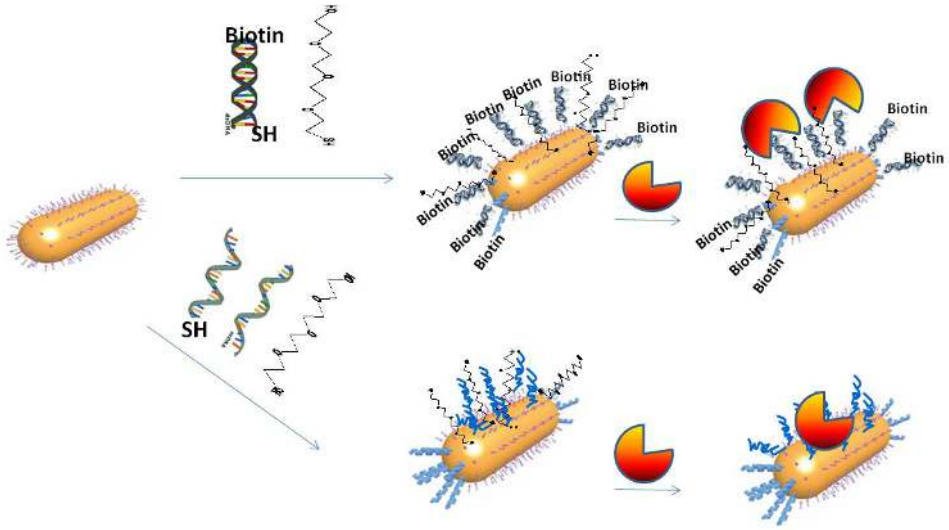

Figure 3.25 Full functionalization of gold nanorods with ss-DNA probe sequences in a mixed monolayer with a thiolated PEG-4-SH spacer for both complementary RNA sequence and a non-complementary sequence, and anti-biotin antibody binding assay.

The full functionalization of glass-immobilized gold nanorods with a DNA hybrid was carried out by immersion in a mixture solution containing thiolated ds-DNA (5 μM) and PEG-4-SH (5 μM) for 90 mins. The control system was also prepared by full functionalization of gold nanorods with a mixture solution containing the thiolated ss-DNA probe (5 μM), a non-complementary DNA sequence (5 μM) and PEG-4-SH (5 μM) for 90 mins. The plasmonic red-shift upon full functionalization are shown in the Table. Afterwards, the kinetic binding assay of biotin-antibiotin for two systems were measured (Table 3.3).

The results show very small plasmon red-shifts of 2.6 + 0.3 nm and 1.1 + 0.8 nm for the ds-DNA and ss-DNA fully-functionalized gold nanorods, respectively. The small difference in the plasmon red-shifts between the model sensor and its control system lead us to conclude that the response observed is mostly due to low functionalization of gold naorods by the bio molecule non-specific interactions between the bio macromolecule and the gold nanorods' surface. Thus, these model plasmonic sensors failed to produce the adequate response for nucleic acid sensing through hybridization.

Table 3.3 Full Functionalization of gold nanorods with a mixed monolayer of thiolated DNA and PEG-4-SH and results from plasmonic sensing.

Biosensing Assay	**ss-Dengue Virus DNA: CS-Dengue Virus: PEG-4-SH (1:1:1)**	**ss-Dengue Virus DNA: Non-CS-Dengue Virus: PEG-4-SH (1:1:1)**
ΔLSPR (nm) GNRs Full Functionalization	2.3	0
	2.5	2
	3	1.3
	Average= 2.6 ± 0.3	Average= 1.1± 0.8
ΔLSPR (nm) Anti-Biotin Antibody	0	0
	0	0
	0	0
	Average= 0	Average= 0

3.4 Single-Particle Spectroscopy of Gold Nanorods and Confocal Fluorescence Lifetime Microscopy

3.4.1 Single gold nanorods functionalized with ss-DNA oligonucleotides and TMPyP

The enhancement of fluorescence emission from TMPyP porphyrin on single gold nanorods functionalized with Dengue Virus ss-DNA analogue sequence was studied. Firstly, the glass-immobilized gold nanoparticles immersed in H_2O,or in PBS buffer, were excited by the laser at the wavelength 480 nm to obtain a scanning confocal image (Figure 3.26).Then, a total of 20 single gold nanorods were selected to measure their optical spectrum.

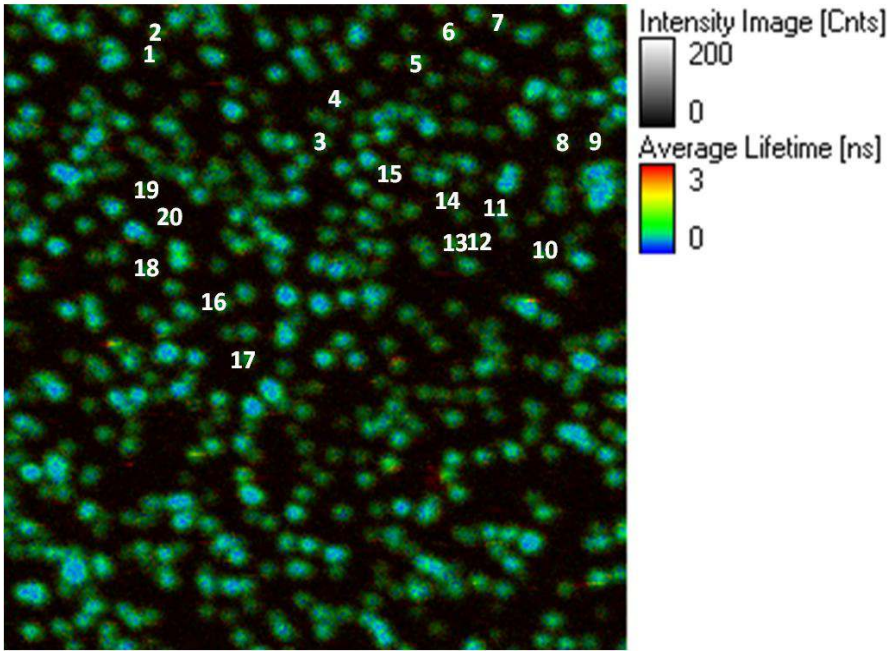

Figure 3.26 Scanning confocal image of glass immobilized single gold nanorods immersed in PBS buffer excited at 480 nm.

The LSPR band of each single particle was fitted with a Lorentzian function in order to find its center position and line width (Figure 3.27) and (Table B2, Annex B).

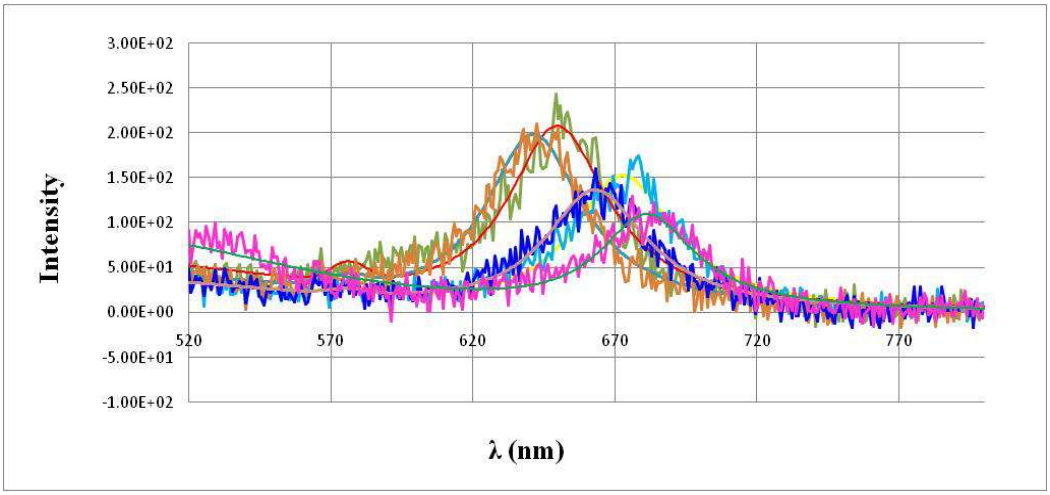

Figure 3.27 LSPR band of single gold nanorods in PBS (5 particles shown here) fitted with a Lorentzian function.

The functionalization of glass-immobilized gold nanorods was carried out by immersing in a solution of a Dengue virus ss-DNA analogue sequence with a concentration of 100 nM in

PBS buffer during 30 minutes. The LSPR spectrum of the 20 selected nanoparticles was measured after ss-DNA functionalization (Figure 3.28). The results are shown in Table B.3 (Annex B). The average LSPR peak wavelengths of sampled nanorods are:

In H_2O: average LSPR = 654.7 $\pm$ 17.7 nm

In PBS: average LSPR = 655.5 $\pm$ 17.1 nm

After Functionalization with ss-DNA in PBS buffer: average LSPR= 653.7 $\pm$ 17 nm

The average peak shift calculated from the individual peak shifts measured particle by particle when condition changes from water to PBS, and after functionalization are:

Average ΔLSPR (PBS-H_2O) = 0.9 $\pm$ 1.4

Average ΔLSPR (After ss-DNA functionalization - PBS)= -1.9 $\pm$ 1.1

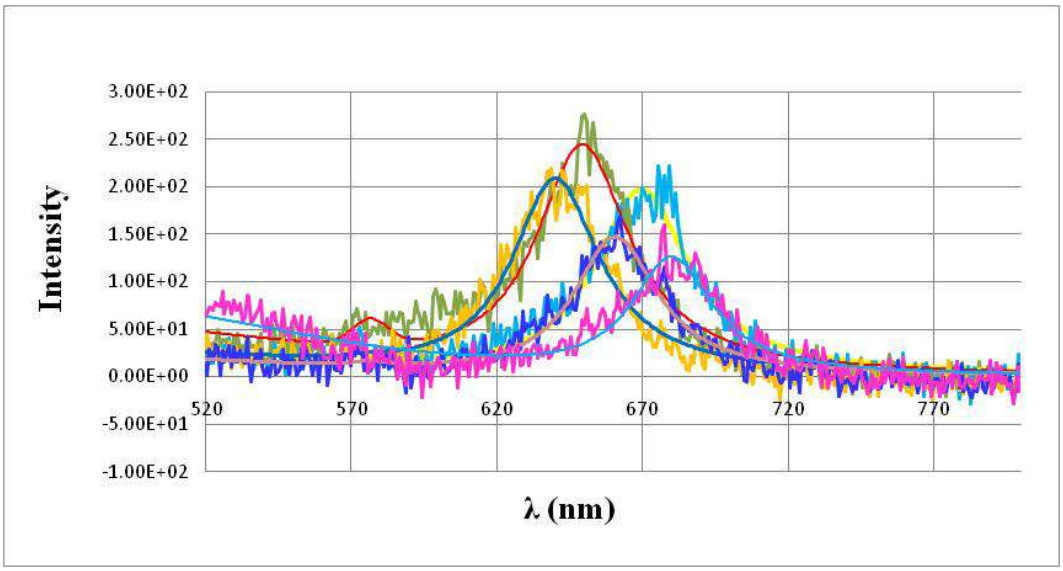

Figure 3.28 Lorentzian fitting function to calculate the LSPR of single gold nanorods after Functinalization with Single Strand Dengue Virus DNA

The excitation laser was changed to 640 nm and the same area as before was scanned to obtain a confocal photoluminescence image of single gold nanorods functionalized with Dengue virus ss-DNA analogue sequences. Then, it was added TMPyP porphyrin (20 nM) to the DNA solution immersing the gold nanorods. The emission intensity time traces were measured on the previously selected single particles. These time traces show strong fluorescence bursts, which are attributed to TMPyP molecules that come into close proximity

of the nanorod and experience the enhanced plasmon filed at the particle tips (Figure 3.29). In figure 3.30, it is shown a time trace for a control measurement carried out under similar conditions for glass-immobilized gold nanorods without DNA spacer. In this case, only a few and less intense fluorescence bursts are observed, which suggests a weak interaction between TMPyP and non-functionalized gold nanorods.

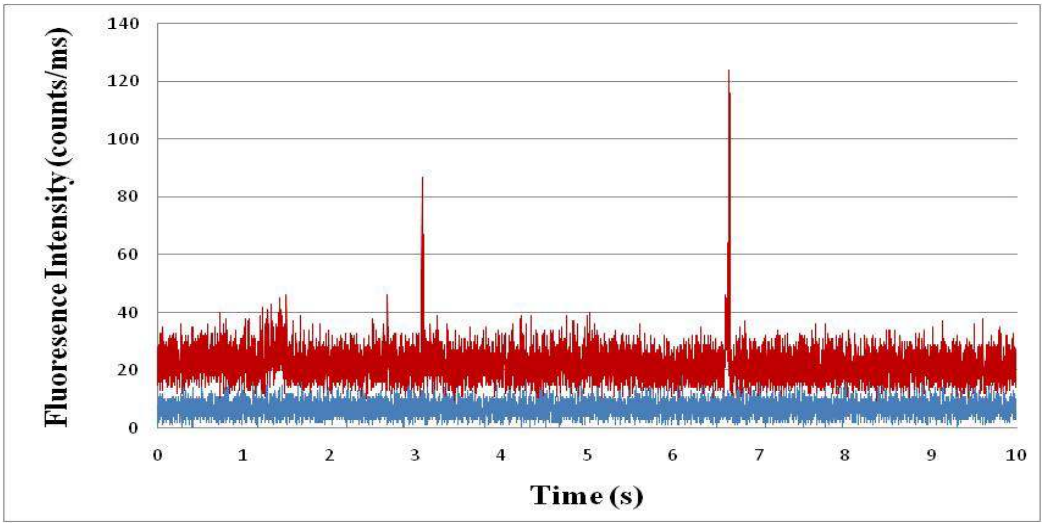

Figure 3.29 Fluorescence intensity versus the time of TMPyP interacting with a gold nanorod functionalized with ss-Dengue DNA analogue sequence showing intense fluorescence bursts with aximum of 120 counts/ms (red) and control measurement on the same nanorod showing the background signal measured before adding TMPyP in solution (blue)

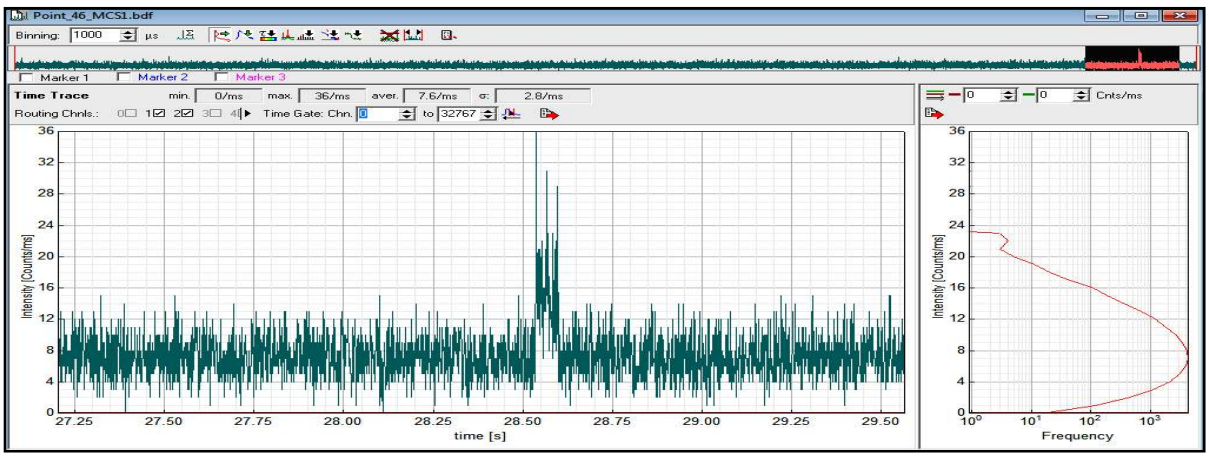

Figure 3.30 Fluorescence intensity versus the time of TMPyP interacting with anon-functionalized single gold nanorod showing a weak fluorescence burst with a maximum of only 36 counts/ms.

For evaluating the fluorescence enhancement effect, it was calculated the top enhancement factor, which is the ratio between enhanced and non-enhanced emission for the most intense fluorescence burst event. The enhanced emission for a particular event is given by the maximum number of counts corrected for the background signal. The latter was determined from the intensity-frequency histogram of the time trace by fitting a Gaussian function to the background peak (Figure 3.31). The background signal was defined from the average photon counts plus two times the standard deviation retrieved from the Gaussian fitting.

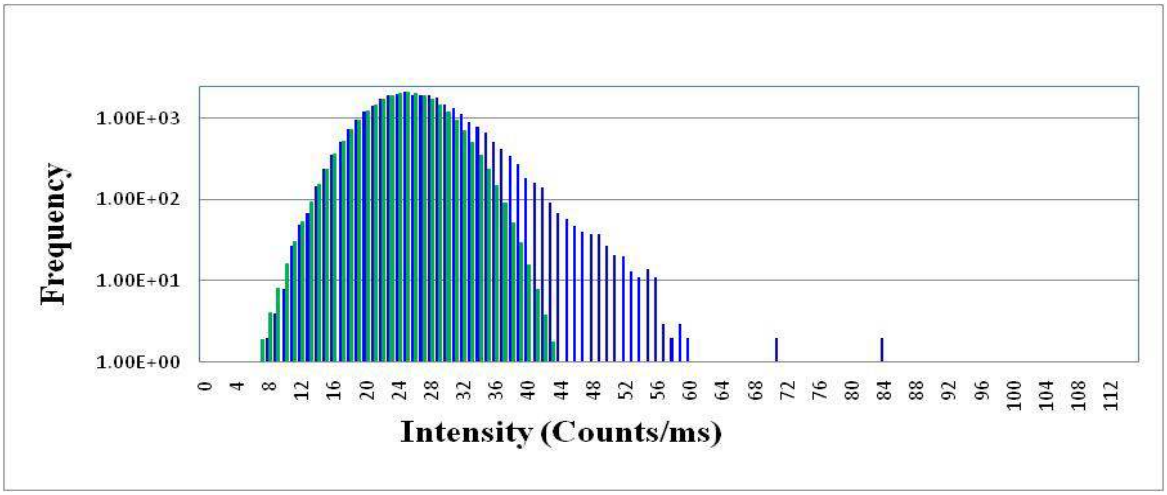

Figure 3.31 Histograms of frequency versus emission intensity of TMPyP porphyrin on gold nanorods functionalized with ss-DNA (blue) and fitted Gaussian function (green).

The non-enhanced emission of TMPyP porphyrin was previously determined from fluorescence measurements in the same confocal microscope for similar experimental conditions to those used in the enhancement experiments [250]. Then, the emission enhancement factors were obtained from dividing the maximum emission intensity corrected for the background by the non-enhanced emission of TMPyP porphyrin. The top enhancement factors determined for the several nanorods measured gave an average enhancement factor of 60600 $\pm$ 29300 (Table B.4, Annex B). Also, an enhancement figure of merit factor was calculated by multiplying the enhancement factors by the fluorescence quantum yield of TMPyP (0.05, [251]) thus giving an average value for this figure of merit of 3030 $\pm$ 1460 (Table B.4, Annex B).

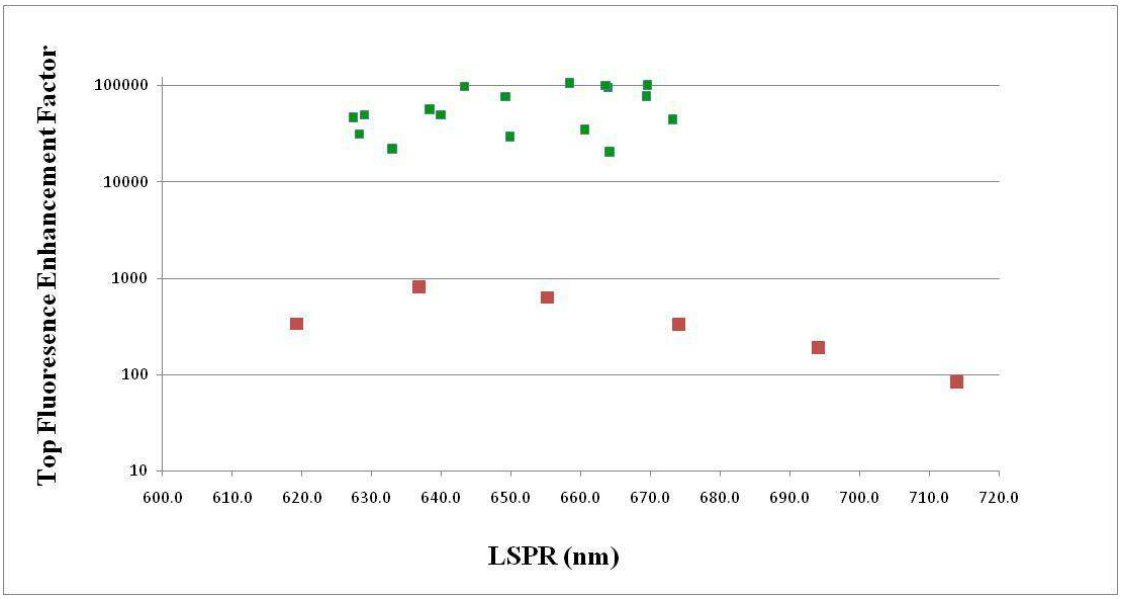

Figure 3.32 Top fluorescence enhancement factor of ss-Dengue Virus DNA functionalized single gold nanorods on glass with TMPyP solution compared to the calculated maximum fluorescence enhancement factor of single gold nano rods with TMPyP

We have compared our experimental enhancement results with theoretical predictions calculated from DDA simulations that describe TMPyP as a radiating dipole positioned at different distances from the tip of a single gold nanorod [252]. The length of the nanorod was varied in the simulations to evaluate the enhancement predicted at different LSPR values. The maximum fluorescence enhancement at the nanorod's tip occurs at an optimum distance for different LSPR of simulated gold nanoparticles (Figure B.11 and B.12, Annex B).

We found surprisingly large enhancement factors of around 60000-fold for TMPyP's emission. These values of enhancement are two orders of magnitude larger than our calculated highest enhanced fluorescence for TMPyP molecule (Figure 3.32).

3.4.1.1 Time Correlated Single Photon Counting (TCSPC)

Time-Correlated Single Photon Counting (TCSPC) was used to determine the fluorescence lifetime. The figure shows the TCSPC histogram of TMPyP's emission on a single gold nanorod functionalized with Dengue Virus ss-DNA analogue sequence. It comprises two components, a fast component and a long component with lifetime values and relative contributions shown in Table 3.4 and Figure 3.33 .

Table 3.4 Fluorescence lifetime values and relative contributions of TMPyP's emission on a single gold nanorod functionalized with Dengue Virus ss-DNA analogue sequence.

Sample	Life Time 1 (Percentage)	Life Time 2 (Percentage)	Life Time 3 (Percentage)
ss-DNA Functionalized Single GNR-TMPyP	9.00 ns (39%)	0.097 ns (44%)	1.49 ns (17%)

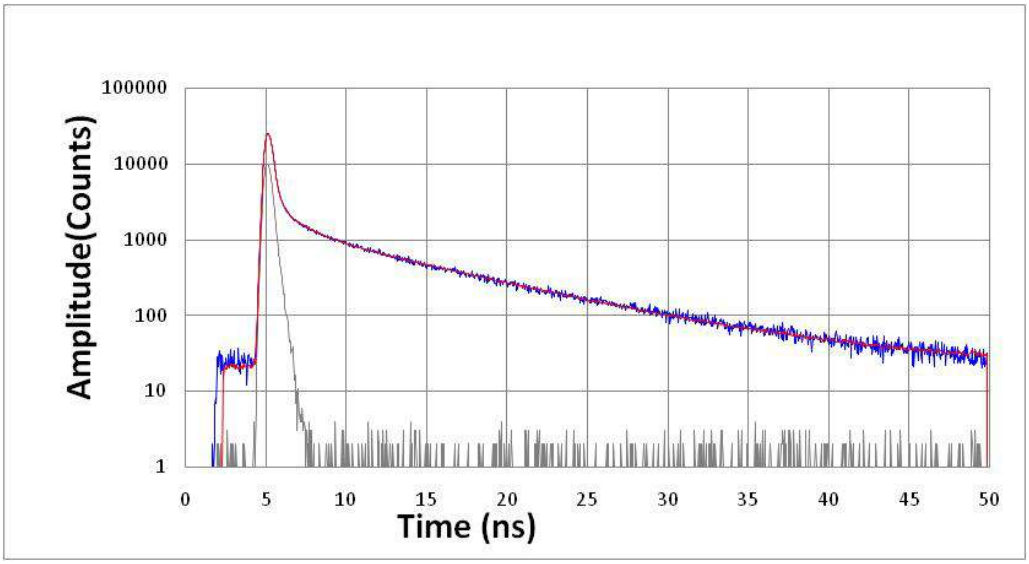

Figure 3.33 Fluorescence decay of TMPyP's emission on a single gold nanorod functionalized with Dengue Virus ss-DNA analogue sequence.

3.4.1.2 Photoluminescence of single gold nanorods

Plasmonic nanostructures have a large optical extinction cross section (that comprises both absorption and scattering). Photoluminescence (abbreviated as PL) is light emission from any form of matter when it relaxes from an electronically excited-state after it has absorbed photon energy from electromagnetic radiation. The photoluminescence of glass-immobilized single gold nanorods was measured at laser excitation wavelengths of both 480 nm (Figure 3.34 and Table B.5, Annex B) and 640 nm (Table B.5, Annex B).

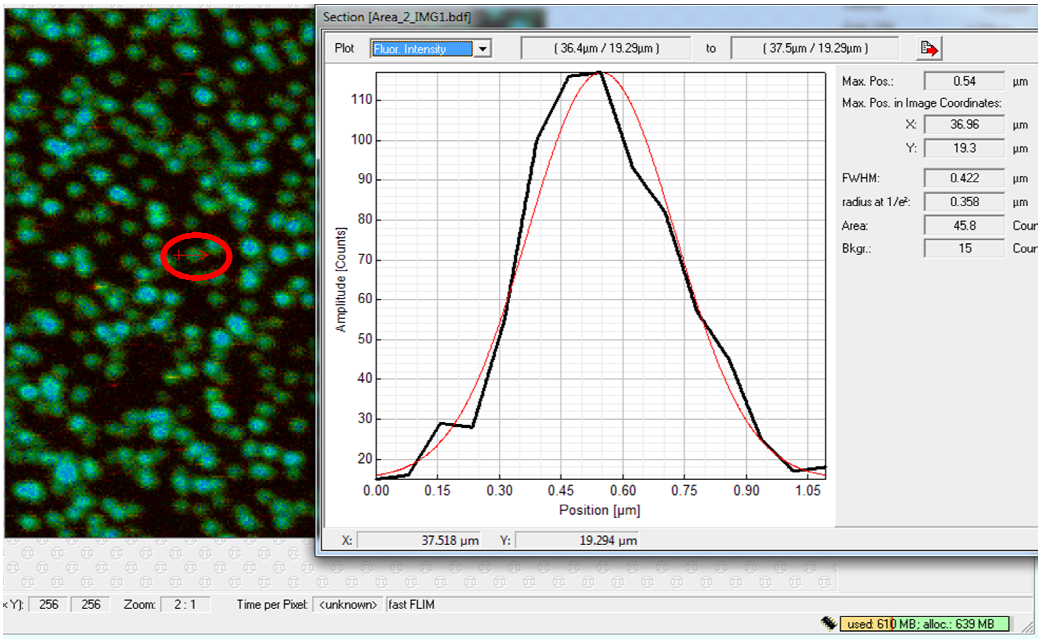

Figure 3.34 Photoluminescence Intensity of glass-immobilized single gold nanorod for an excitation wavelength of 480 nm

The photoluminescence intensity varies slightly from particle to particle due to sample heterogeneity. The TEM image of the gold nanorods sample used in this study clearly shows that there is a dispersion of particles sizes and aspect ratios (Figure 3.35).

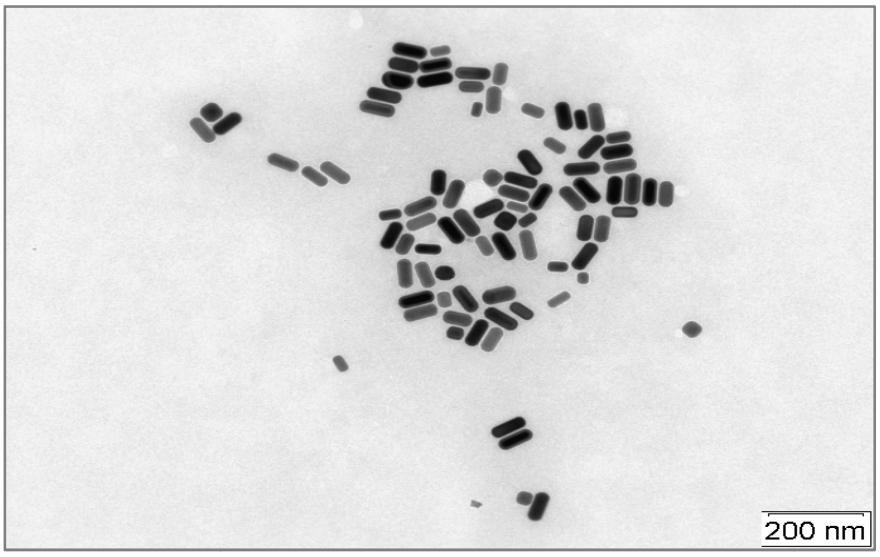

Figure 3.35 The TEM image of gold nanorod sample used as purchased.

The particles with larger volume have larger absorption cross-sections and, thus, absorb more photons for a certain irradiance. Consequently, larger particles also emit more photons, so they have stronger photoluminescence intensity. On the other hand, particles with larger volumes tend to scatter even more strongly and, thus, to give more fluorescence

enhancement, as the antenna effect is related with the scattering versus absorption efficiency of the plasmonic nanoparticle. In agreement, Figure 3.36 shows a weak correlation of top enhancement factors versus the photoluminescence intensity of the corresponding single gold nanorods both at 480 nm and 640 nm excitation wavelengths.

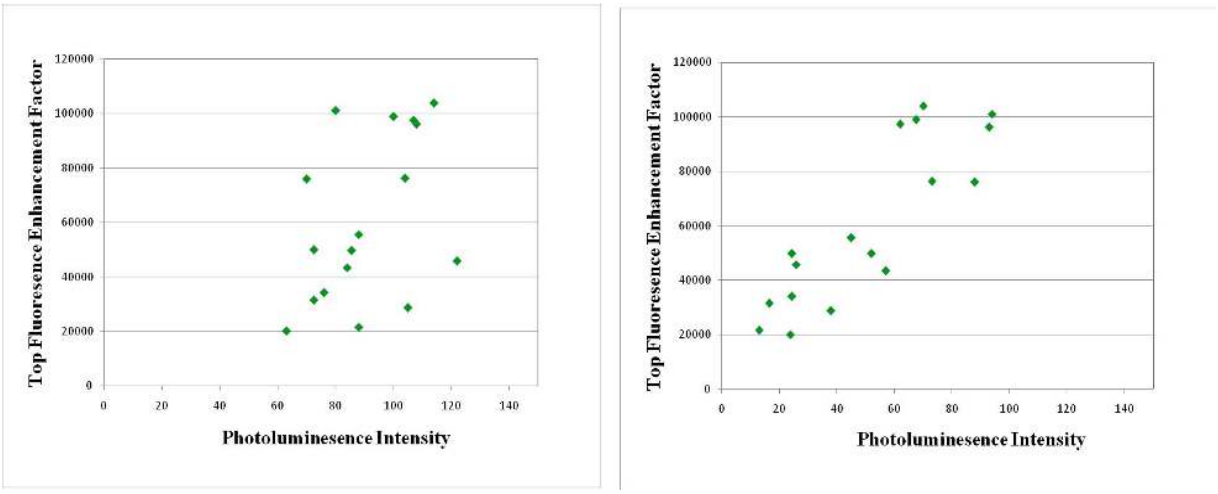

Figure 3.36 Top fluorescence enhancement factors versus the photoluminescence intensity of single gold nanorods excited at 480 nm (left graph) and excited at 640 nm (right graph.

3.4.2 Single gold nanorods functionalized with ds-DNA oligonucleotides and TMPyP

The enhancement of fluorescence emission of TMPyP was also studied on single gold nanorods now functionalized with ds-DNA of the same analogue sequence from Dengue virus. As before, it was selected 20 single gold nanorods from a scanning confocal image obtained for an excitation wavelength of 480 nm (Figure 3.37).

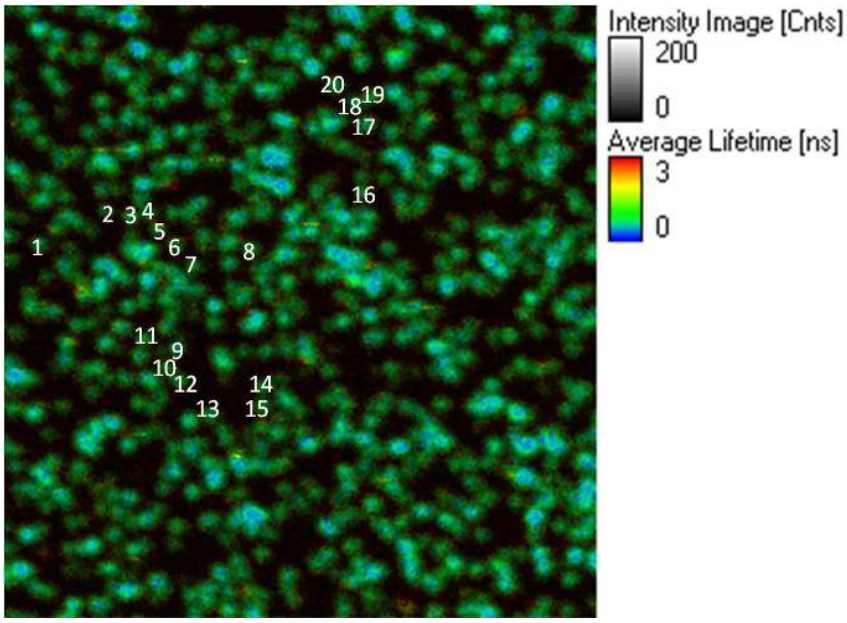

Figure 3.37 Scanning confocal image of glass immobilized single gold nanorods excited at 480 nm in PBS.

The LSPR spectrum of each single particle was measured, and the peak wavelength and the line width were determined by fitting a Lorentzian function (Figure 3.38 and Table B.7, Annex B).

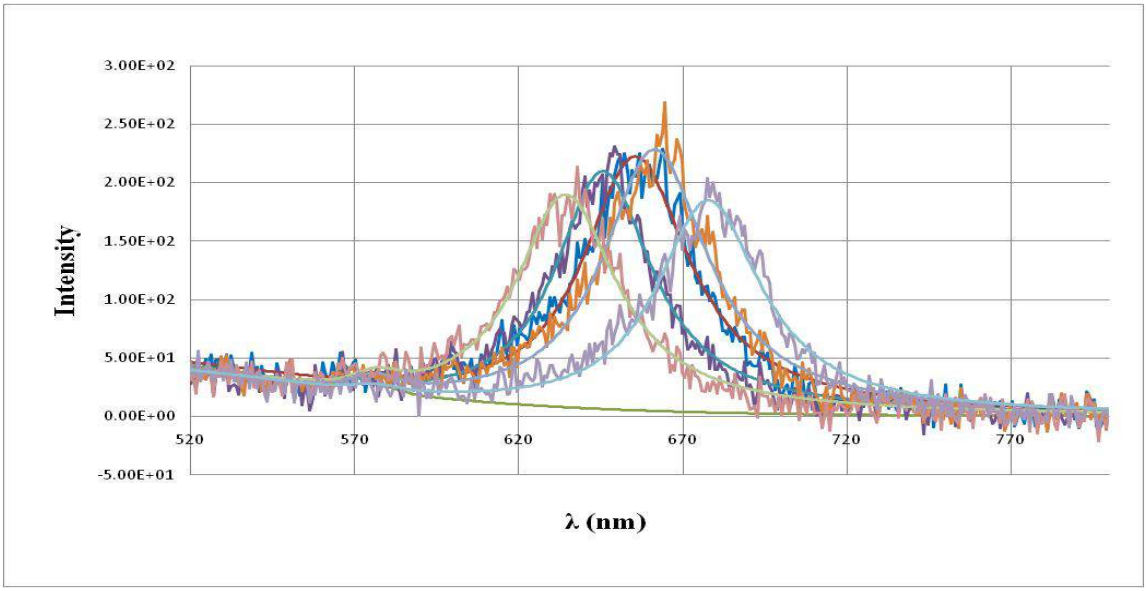

Figure 3.38 LSPR band of single gold nanorods in PBS (5 particles shown here) fitted with a Lorentzian function.

A solution of Dengue virus ds-DNA sequence analogue prepared trough hybridization of ss-DNA previously used with a RNA complementary sequence during 20 minutes in PBS buffer, to givea ds-DNA concentration of 100 nM. The functionalization of glass-immobilized gold nanorods was carried out by the immersing the surface inds-DNA solution for 30 minutes. The LSPR peak wavelength of the selected 20 single nanoparticles was monitored after ds-DNA functionalization (Figure 3.39). The changes in peak wavelength due to ds-DNA functionalization are listed in the Table B.8 (Annex B). The average LSPR peak wavelengths of sampled nanorods are:

In H_2O: average LSPR = 648.6 $\pm$ 13.3

In PBS buffer: average LSPR = 650.6 + 17.1

After Functionalization of gold nanorods with ds-DNA: average LSPR= 650.8 $\pm$ 13.8

The average peak shift calculated from the individual peak shifts measured particle by particle when condition changes from water to PBS, and after functionalization are:

Average ΔLSPR (PBS-H_2O) = 2.1 $\pm$ 1

Average ΔLSPR (After ds-DNA functionalization - PBS)= 0.2 $\pm$ 1.8

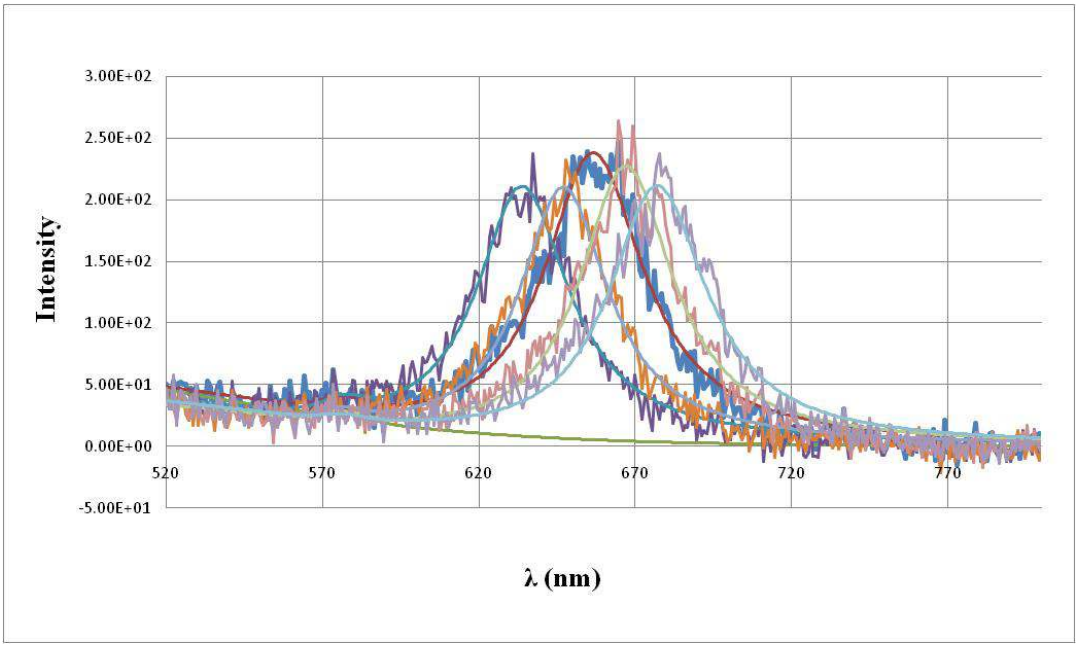

Figure 3.39 Lorentzian fitting function to calculate the LSPR of single gold nanorods after Functinalization with Double Strand Dengue Virus DNA (5 particles)

The excitation laser was changed to 640 nm and the same area as before was scanned to obtain a confocal photoluminescence image of single gold nanorods functionalized with Dengue virus ds-DNA analogue sequences. Then, it was added TMPyP porphyrin (20 nM) to the DNA solution immersing the gold nanorods. The emission intensity time traces were measured on the previously selected single particles. Similarly to the results obtained with ss-DNA functionalized rods, also in this case the time traces show strong fluorescence bursts, which are attributed to TMPyP molecules that come into close proximity of the nanorod and having their emission enhanced by the antenna effect of the plasmonic particle (Figure 3.40).

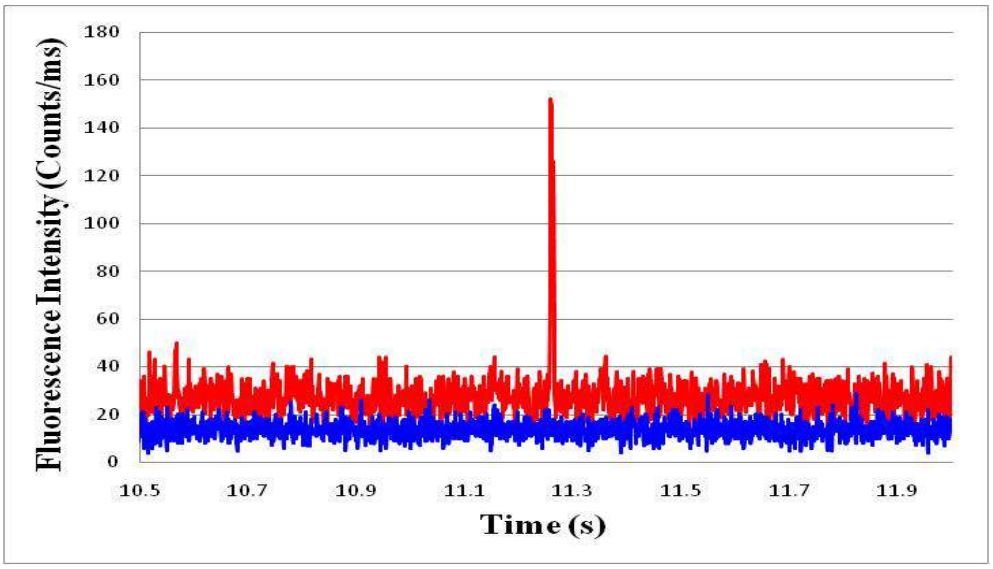

Figure 3.40 Fluorescence intensity versus the time of TMPyP interacting with a single gold nanorod functionalized with ds-Dengue DNA analogue sequence showing intense fluorescence bursts with a maximum of 120 counts/ms (red) and control measurement on the same nanorod showing the background signal measured before adding the TMPyP in solution (blue).

For calculation of Top Fluorescence Enhanced Factor, firstly, the size of maximum burst were calculated using Gaussian fitting function of GNR-TMPyP on the basis of photon counts above the average fluorescence intensity plus 2 sigma limitation (Figure 3.41).

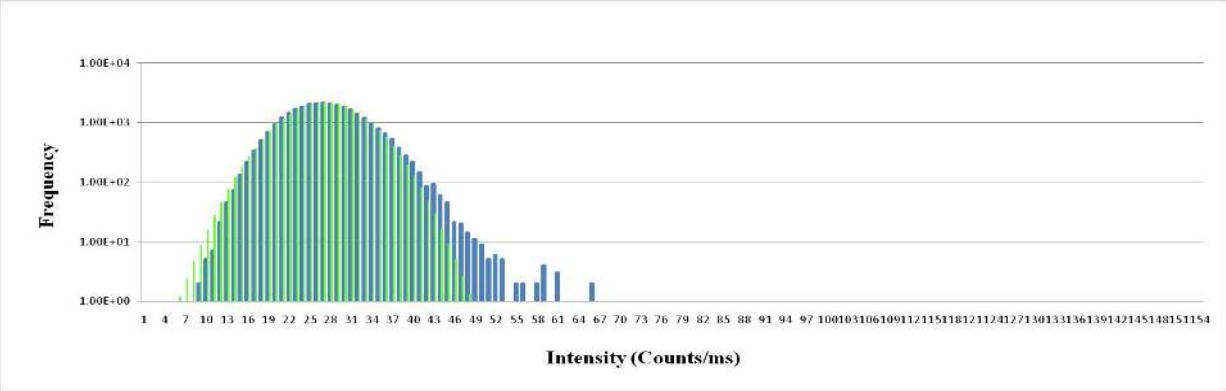

Figure 3.41 Gaussian fitting graph of single gold nanorod-TMPyP system (green graph), ds-Denv2-TMPyP functionalized single gold nano particles (blue graph)

The top fluorescence enhancement factors were calculated for ds-DNA functionalized gold nanorods in the same way as previously described for the ss-DNA functionalization. The average of top florescence enhancement was obtained 60900+ 36400 (Table B.9, Annex B). The enhancement figure of merit has an average value of 3040 $\pm$ 1820 (Table B.9, Annex B) in the case of ds-DNA functionalization. Figure 3.42 shows a scatter plot of top fluorescence enhancement factor versus the LSPR peak wavelength of the respective single gold nanorods.

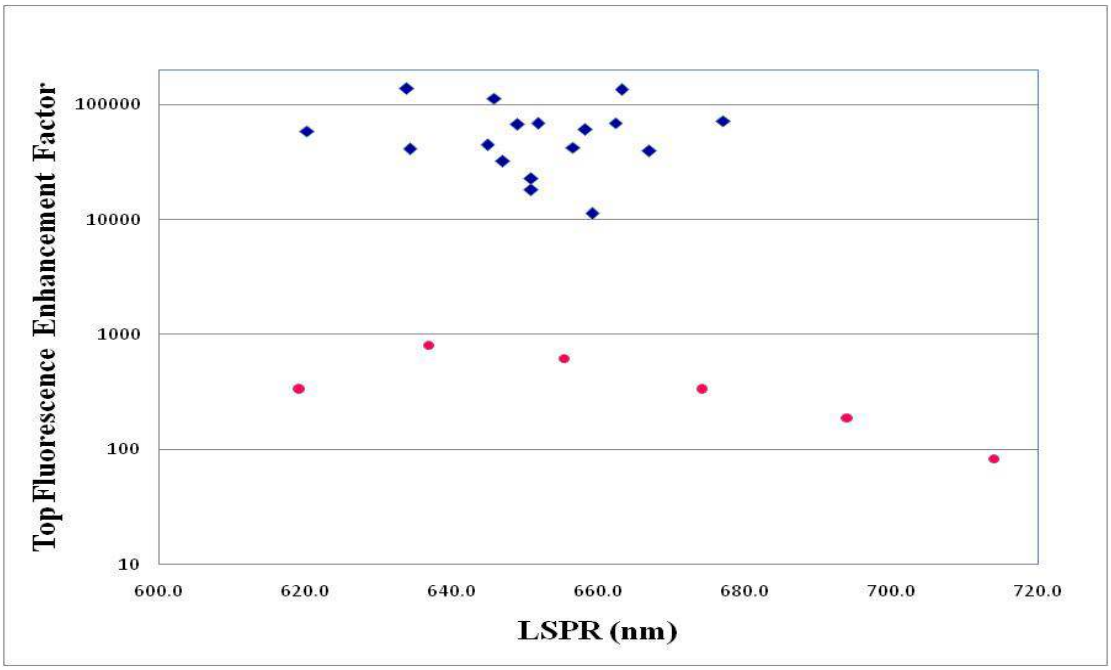

Figure 3.42 Top fluorescence enhancement factor of ds-Dengue Virus DNA functionalized single gold nanorods on glass with TPMPyP solution compared to the calculated maximum fluorescence enhancement factor of single gold nanorods with TMPyP

Also in the case of ds-DNA functionalization, we found surprisingly large enhancement factors of around 60000-fold for TMPyP's emission. These enhancement values are again two orders of magnitude larger than our calculated fluorescence enhancements for TMPyP molecule. The similar range of experimental enhancement factors found for ss-DNA and ds-DNA functionalized gold nanorods suggests that both DNA coatings mediate in a similar way the interaction between TMPyP and the nanorods, thus, resulting in similar antenna effects.

The LSPR and fluorescence enhancement of TMPyP was also investigated for ds-DNA functionalized gold nanorods, in which the TMPyP was previously complexed with ds-DNA before the functionalization onto the gold nanorods. The LSPR peak wavelength of the selected single nanoparticles was monitored before and after complex-ds-DNA-TMPyP functionalization (Figures B.1, B.2, B3, and Tables B.11, B.12, B.13, Annex B). The enhancement factors were very similar to the sequential functionalization with ds-DNA and TMPyP complexation (Figures B.4, B.5, B.6, B.7 and Tables B.14, B16 Annex B), previously presented, and as such, we infer that the order of the experiment (i.e. first complexation and then functionalization or first functionalization and then complexation) does not affect the results and it leads to the same enhancement effect being observed. The figure 3.43 is the scatter plot of enhancement factor vs plasmon peak wavelength showing the results for the two systems of ds-DNA functionalization would be presented.

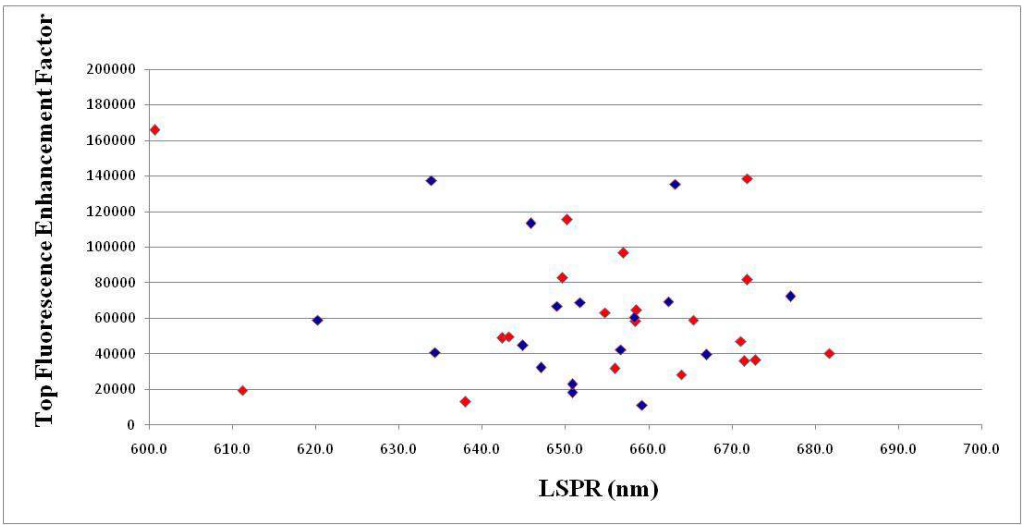

Figure 3.43 Comparison of top fluorescence enhancement of Complex ds-Dengue DNA-TMPyP functionalized single gold nanorods –TMPyP (20 nM) (red), ds-Dengue DNA functionalized single gold nano rods-TMPyP (20 nM) (blue)

3.4.2.1 Time Correlated Single Photon Counting (TCSPC)

The figure 3.44 shows the fluorescence decay of TMPyP's emission in the presence of a single gold nanorod functionalized with Dengue Virus ds-DNA sequence analogue. It comprises two components: i) a fast component, that is attributed to TMPyP's enhanced emission and background signal from the gold nanorods, and; ii) a long component, that is attributed to TMPyP's non-enhanced emission mostly from glass-adsorbed molecules. The fitted exponential lifetimes and their relative contribution are listed in Table 3.4 .

Table 3.4 Lifetimes of TMPyP's emission in the presence of single gold nanorod Functionalized with Dengue virus ds-DNA analogue sequence

Sample	Lifetime 1 (Percentage)	Lifetime 2 (Percentage)	Lifetime 3 (Percentage)
ds-DNA-Functionalized Single GNRs-TMPyP	8.7 ns (47.5%)	0.054 ns (41.6%)	1.524 ns (10.9%)

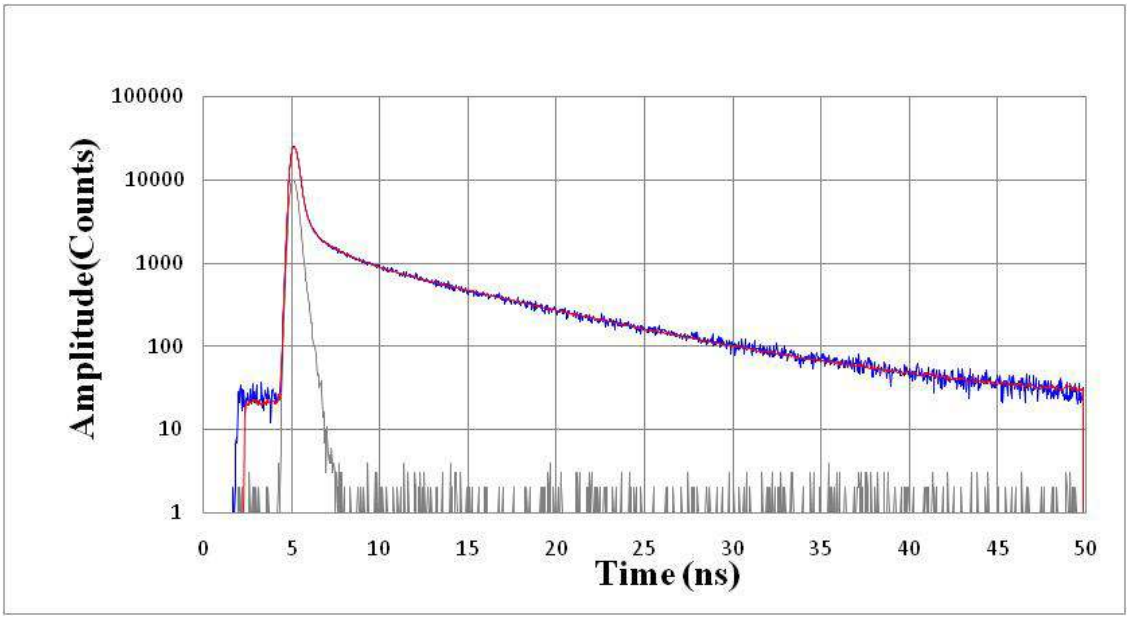

Figure 3.44 Fluorescence decay of TMPyP's emission in the presence of single gold nanorod functionalized with Dengue virus ds-DNA analogue sequence

3.4.2.2 Photoluminescence Intensity of glass-immobilized single gold nanorods

The photoluminescence of glass-immobilized single gold nanorods were measured at excitation wavelengths of 480 nm (Figure 3.45 and Table B.10, Annex B) and 640 nm (Table B.10, Annex B). Figure 3.46 shows a weak correlation of top fluorescence enhancement factors versus the photoluminescence intensity of corresponding single gold nanorods for both excitation wavelengths.

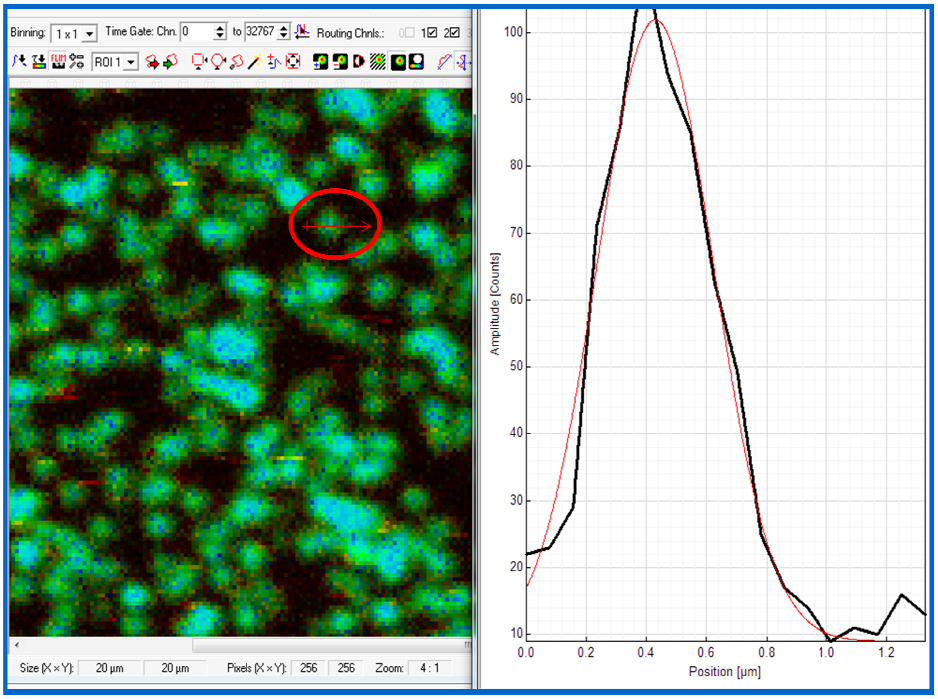

Figure 3.45 Photoluminescence intensity of glass immobilized single gold nanorod at laser excitation wavelength of 480 nm

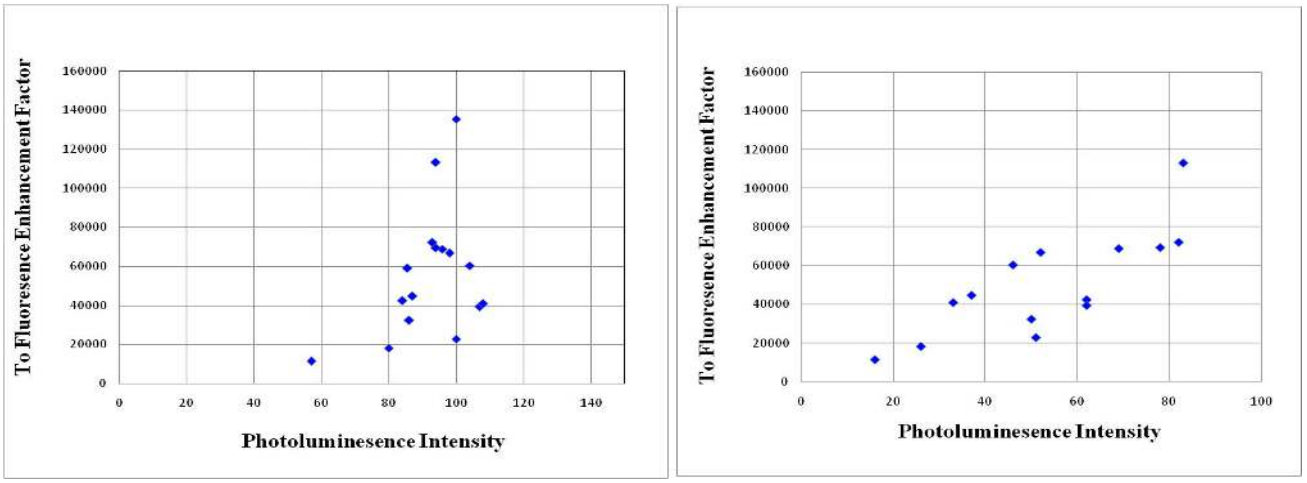

Figure 3.46 Top fluorescence enhancement factor versus the photoluminescence intensity of single gold nanorods excited at 480 nm (left graph) and excited at 640 nm (right graph.

3.4.3 Single gold nanorods functionalized with AUT interaction with TPPS porphyrin

The large enhancement effects previously observed with TMPyP prompted us to investigate this antenna effect on a different porphyrin using the same nanorods, but also changing the surface coating. For this purpose, the tetra-anionic porphyrinTPPS^{-4}was used to study the interaction with single gold nanorods functionalized with 11-amino-1-undecanethiol (AUT), which in PBS buffer should confer a positive surface charge to the nanorods (Figure 3.47).

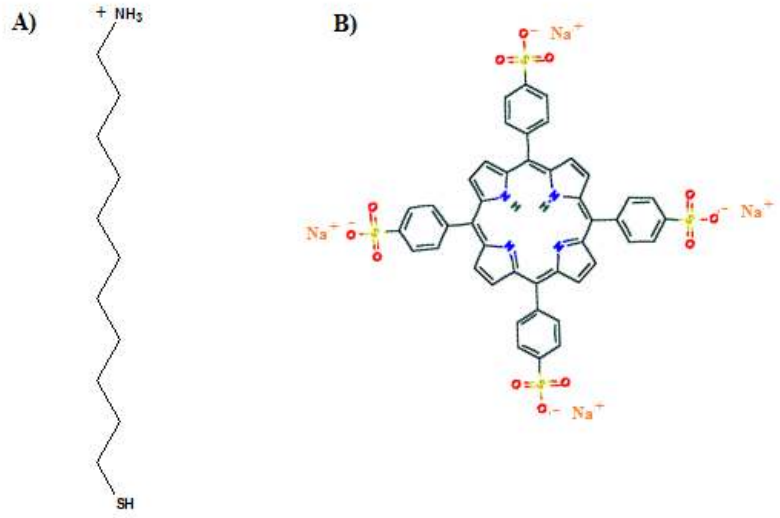

Figure 3.47 A) Chemical structure of 11-amino-1-undecanethiol (AUT) used as a positively-charged spacer, and B) TPPS used as a negatively-charged porphyrin.

TPPS has porphyrin core structure similar to the TMPyP and importantly its photophysical properties such as Q-band absorption spectra, as well as the emission spectra, are also comparable (Figure 3.48 and Table 3.5)

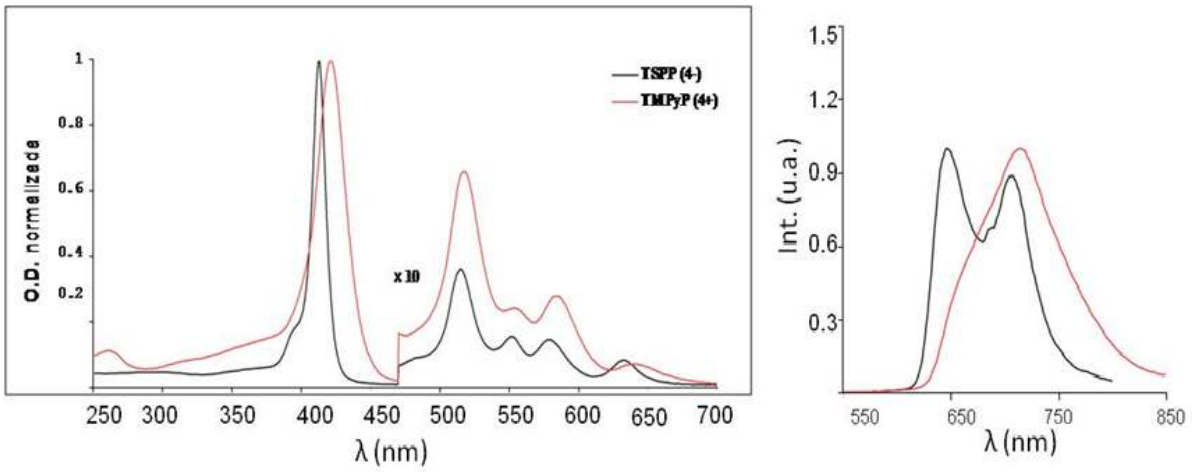

Figure 3.48 Comparison of absorption and emission spectra of $TPPS^{4-}$and $TMPyP^{4+}$porphyrins [253].

Table 3.5 Comparison of photophysical properties of $TPPS^{4-}$ and $TMPyP^{4+}$ porphyrins [253].

	$B(,0)$ / nm ($\Delta\nu_{1/2}$ / cm-1)	$Q_y(1,0)$	$Q_y(0,0)$	$Q_x(1,0)$	$Q_x(0,0)$
$TSPP^{4-}$	413	514	551	580	633
	(621)	(939)	(641)	(714)	(506)
$TMPyP^{4+}$	422	517	556	586	641
	(1353)	(1252)	(651)	(827)	(531)

The scanning confocal image of glass immobilized gold nanoparticles in PBS buffer was obtained at an excitation wavelength of 480 nm (Figure 3.49), and 30 single gold nanorods were selected to measure their optical spectrum.

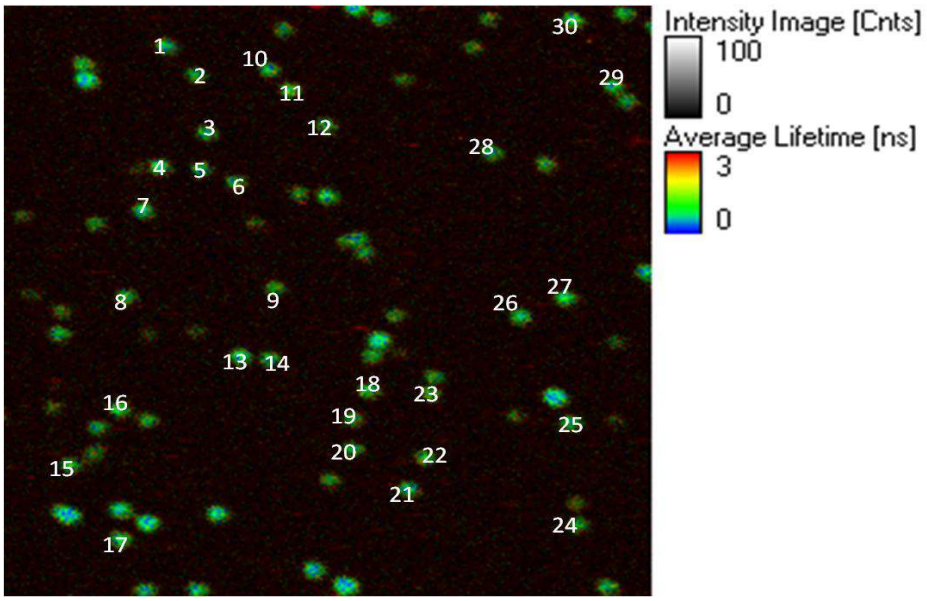

Figure 3.49 Scanning confocal image of glass-immobilized single gold nanorods excited at 480 nm in PBS buffer.

The LSPR peak wavelength of each single particle was measured by fitting a Lorentzian function (Table B.17, Annex B). Single gold nanoparticles were functionalized with a solution of 100 nM of AUT for 30 minutes and the LSPR peak of these 30 single nanoparticles was monitored (Table B.18, Annex B). The average LSPR peak wavelength of the selected single nanorods is:

In PBS: average LSPR = 649.0 $\pm$ 19.8

After Functionalization of single GNRs with AUT: average LSPR= 652.6 $\pm$ 19.9

The average peak shift calculated from the individual peak shifts measured particle by particle when condition changes from PBS to the functionalization are:

Average ΔLSPR (After AUT functionalization - PBS)= 3.6 $\pm$ 1.0

In this case the change in refraction index at the nanorods surface is significant and, thus, we can infer that coating with AUT has occurred.

After washing away the AUT solution, the porphyrin TPPS (10 nM) was added in PBS buffer was added for 30 minutes to investigate their interactions with the AUT-functionalized single gold nanorods. The time trace fluorescence emission was measured before and after adding TPPS with excitation at 640 nm. The results were shown in the Table B.19 (Annex B). The

emission intensity time traces measured on 30 single particles show that fluorescence burst are very rare, which suggests that only a few TPPS molecules come into close proximity of the single gold nanorod during the acquisition time on each particle.

Because of low and rare fluorescence burst events, the concentration of TPPS was increased 10 times (100 nM) (Figure 3.50) to increase the probability of TPPS molecules interacting with gold nanorods (Table B.20, Annex B).

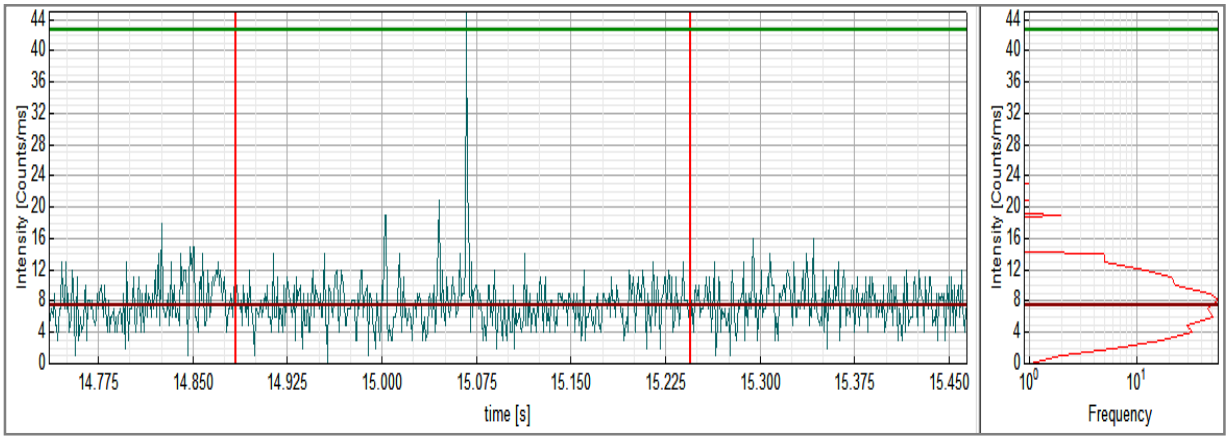

Figure 3.50 Top Fluorescence enhanced (fluorescence burst) with maximum counts of 44 photons of AUT functionalization of single gold nano particles with TPPS (100 nM)

Then, the emission enhancement factors were calculated by comparison with the non-enhanced emission of TPPS in the same experimental conditions (0.00269 count/ms/molecule [254]). The figure of merit for fluorescence enhancement was also calculated considering fluorescence quantum yield of TPPS (0.1, [253]). The average value of top florescence enhancement factors for TPPS (100 nM) was 10144.2 $\pm$ 7034.3 and the respective figure of merit was calculated to be 1014.4 $\pm$ 703.4. Figure 3.51 shows a scatter plot of top fluorescence enhancement factors for TPPS and AUT-functionalized gold nanorods versus their LSPR peak wavelength.

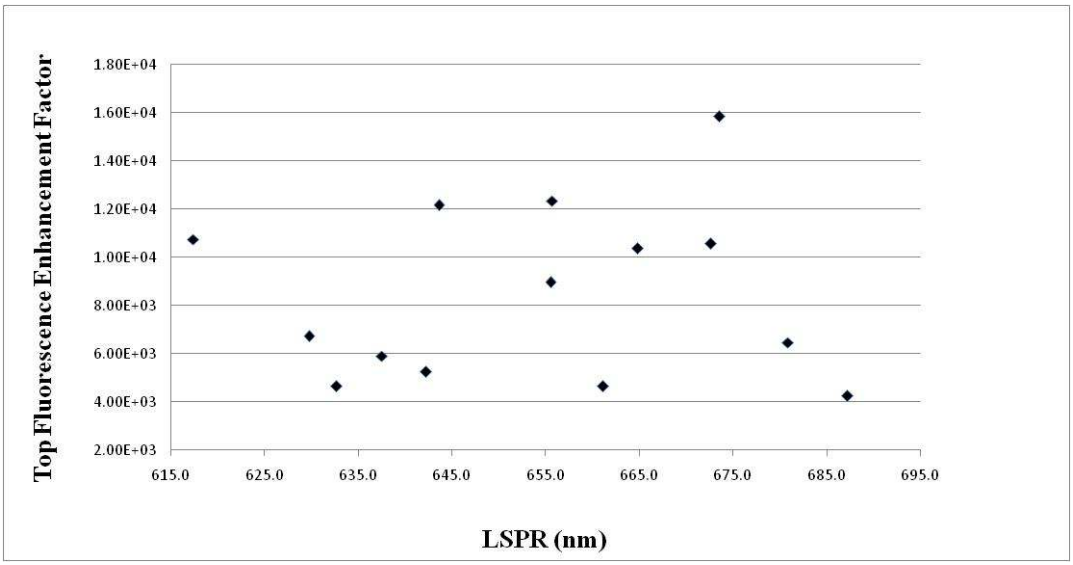

Figure 3.51 Top Fluorescence Enhancement Factor of AUT-functionalized single gold nano particles with TPPS (100 nM) versus their plasmonic resonance wavelength.

3.4.3.2 Photoluminescence Intensity of glass-immobilized single gold nanorods

The photo.luminescence of glass immobilized single gold nanorods were measured at excitation wavelengths of 480 nm (Figure 3.52 and Table B.21, Annex B) and 640 nm (Table B.21, Annex B). Figure 3.53 show a weak correlation of top fluorescence enhancement factor versus the photoluminescence intensity of corresponding single gold nanorods at both excitation wavelengths, as previously observed for TMPyP systems.

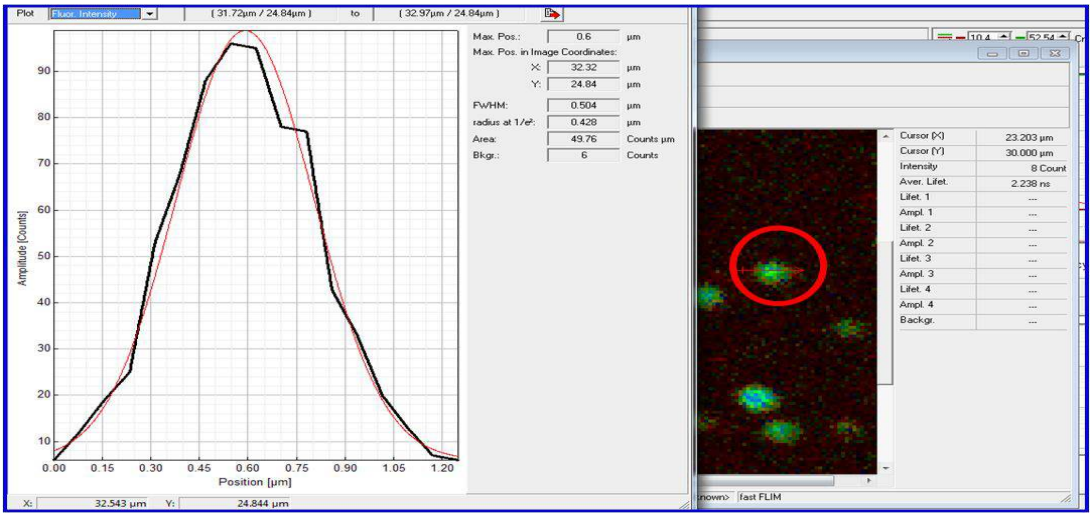

Figure 3.52 Photoluminescence intensity of glass immobilized single gold nanorod at laser excitation wavelength of 480 nm

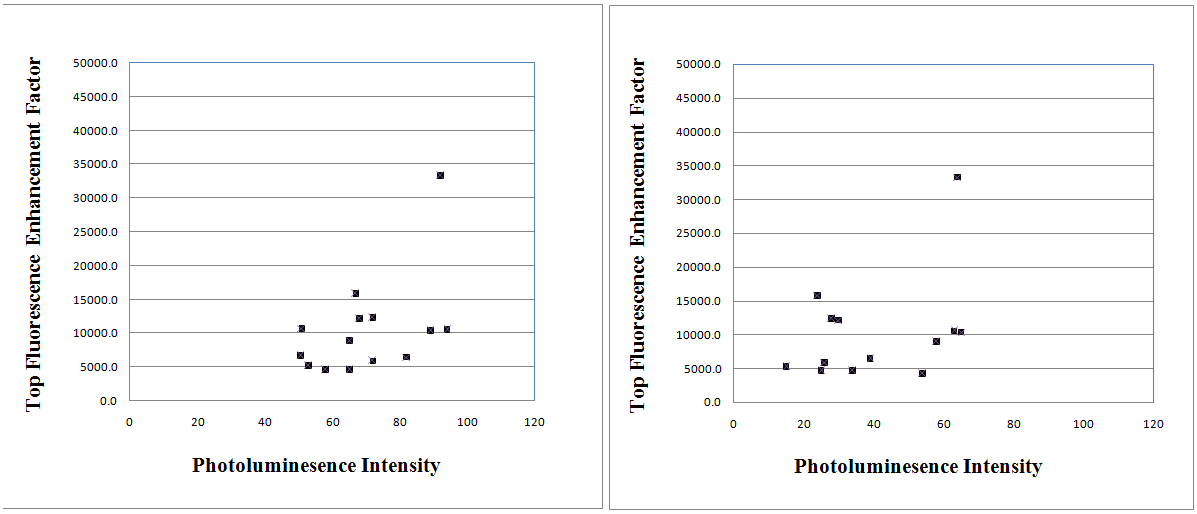

Figure 3.53 Top fluorescence enhancement factor versus the photoluminescence intensity of single gold nanorods excited at 480 nm (left graph) and excited at 640 nm (right graph).

3.5 Comparison of porphyrin emission enhancement on gold nanorods

3.5.1 LSPR

In the Table 3.6, the peak shifts of LSPR wavelength of single gold nanorods after functionalization are compiled. The ΔLSPR is practically negligible for DNA-coated gold nanorods, which suggests that under the conditions tested the coating is very sparse (low DNA surface density) to give an appreciable plasmon peak shift. On the other hand, the AUT coating gives an average shift of 3.6 nm showing that in this case the alkylthiol layer effectively changes the refraction index on the nanorods surface. The refraction index sensitivity of the gold nanorods used here is approximately 200 nm/RIU.

Table 3.6 Comparison of LSPR changes for the porphyrin-gold nanorod systems

Sample	**ΔLSPR**
AUT (100 nM)-functionalized single gold nanorods	3.6 + 1.0 nm
Complex ds-Dengue DNA(100 nM)-TMPyP (20 nM) functionalized single gold nanorods	1.6 $\pm$ 1.7 nm
Ds-Dengue DNA (100 nM)-functionalized single gold nanorods-	0.2 $\pm$ 1.8 nm
Ss-Dengue DNA (100 nM)-functionalized single gold nanorods-	- 1.9 $\pm$ 1.1 nm

3.5.2 Top Fluorescence Enhancement Factor

The top fluorescence enhancements results obtained for the several systems studied are compiled in Table 3.7. The range of enhancement factors for the several TMPyP systems are overlapped, and are approximately two order magnitude more than theoretically predicted maximum fluorescence enhancements (Figure 3.54) .

Table 3.7 Comparison of top fluorescence enhancement factor for the porphyrin-gold nanorod systems

Sample	**Top Fluorescence Enhancement Factor**
Complex ds-Dengue DNA-TMPyP functionalized single gold nanorods –TMPyP	64100 ± 41100
Ds-Dengue DNA functionalized single gold nano rods-TMPyP	60900± 36400
Ss-Dengue DNA functionalized single gold nano rods-TMPyP	60600 ± 29300
AUT -functionalized single gold nanorods-TPPS	10144.2 ± 7034.3

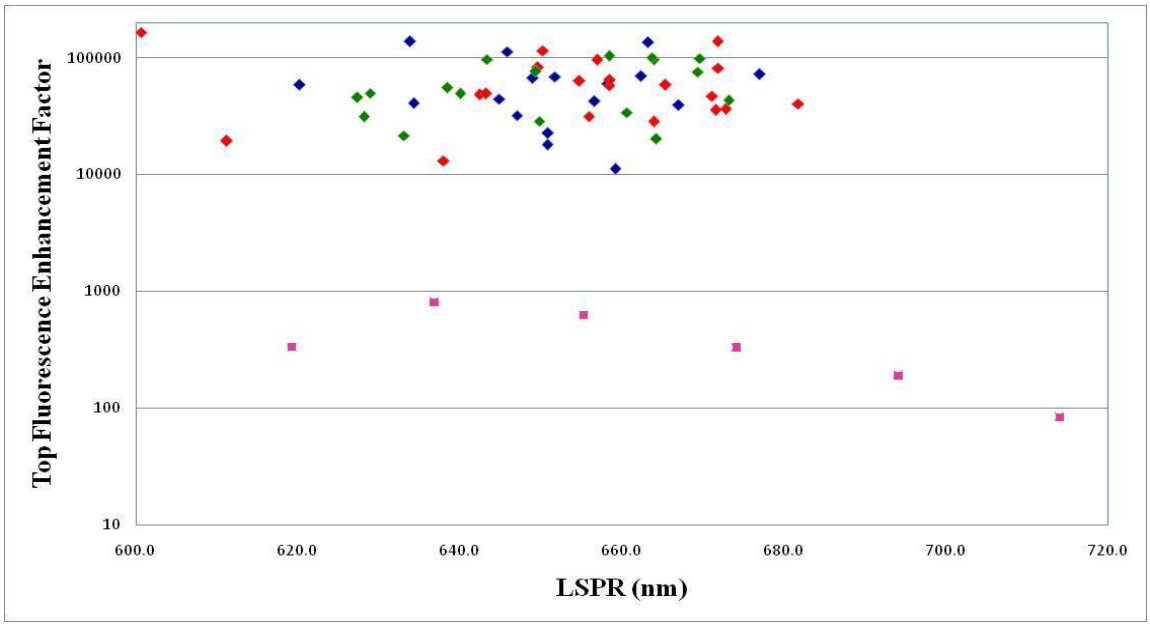

Figure 3.54 Comparison of top fluorescence enhancement of Complex ds-Dengue DNA-TMPyP functionalized single gold nanorods –TMPyP (20 nM) (red), ds-Dengue DNA functionalized single gold nano rods-TMPyP (20 nM) (blue), ss-Dengue DNA functionalized single gold nanorods-TMPyP (20 nM) (green), calculated maximum fluorescence enhancement for single gold nanorods –TMPyP (pink)

This high fluorescence enhancement can be contributed to several important factors including:

1- Confining the optical field into so-called hot spots with volumes much smaller than the diffraction limit. Plasmonic nanostructures enhance the incident field by up to a few orders of magnitude, leading to dye excitation enhancement. They also alter the radiative and non-radiative decay rates of dye molecule in their vicinity. The radiative enhancement results from improved emission by the nano-antenna dipole jointly radiating with the dye's emission dipole.

2- The good overlap between the molecular absorption and emission spectra of the fluorophore and the LSPR of a metal nanoparticle produces the highest fluorescence enhancement factors. In these investigated systems, gold nanorods have longitudinal LSPR wavelengths at 630-660 nm that overlap both Q-bands in the absorption spectra of TMPyP (550-650 nm) and its emission spectra (640-710 nm).

3- Another important parameter is the dye's position and orientation relative to the nano particle. The DNA oligonucleotide on the surface of gold particles creates a sparse and negatively-charged surface that allows a good interaction with positively-charged TMPyP molecule. The DNA coating favors the dye positioning in the vicinity of a gold nanorod to be influenced by the antenna effect (particularly at the tip hot-spots). Moreover, the specific interaction can promote TMPyP molecules to spend more time close to the particles.

4- TMPyP is a weak fluorescence dye, so the antenna effect in the fluorescence emission is more appreciable than that observed for high quantum yield dyes.

However, there is a need for more experiments to find out the reason of such large fluorescence enhancement factors for our porphyrin-gold nanorod systems.

Additionally, there is slight increasing in following order:

Complex ds-Dengue DNA-TMPyP functionalized single GNRs –TMPyP >

Ds-Dengue DNA functionalized single gold nano rods-TMPyP >

Ss-Dengue DNA functionalized single gold nano rods-TMPyP

This result suggests that the complex system may promote a stronger interaction of the TMPyP dye with the gold nano particles, thus leading to a better antenna effect when

compared to the systems of gold nanorods that were previously functionalized with ss-DNA or ds-DNA,and only after placed in the presence of TMPyP in buffer solution.

The top fluorescence enhancement factors obtained for TPPS porphyrin on single gold nanorod functionalized with AUT are substantially much less (Figure and Table) compared to gold nanorods functionalized DNA coatings. This result clearly shows the important role of DNA as a spacer compared to the AUT, but also the lower quantum yield of TMPyP (0.05) compared to TPPS (0.1) could play a role here.

3.5.3 Time Correlated Single Photon Counting (TCSPC)

We proved previously that specific interactions occur between ds- and ss-DNA analogue sequences from Dengue Virus with TMPyP in solution by absorption and fluorescence spectroscopy. The interaction of TMPyP with ds-DNA results in a longer lifetime component of 10.3 ns, when compared to its complex with ss-DNA (8.6 ns), and both complexes have a longer decay component than free TMPyP in solution (5.7 ns).

In DNA functionalized single gold nanorods, the shorter decay component (0.054, 0.061, and 0.097 ns) is considerably shorter than that of free TMPyP in solution (2.3 ns), because it has a different origin.It can be attributed to both emission from single gold nanorods and from enhanced emission due to the interaction of TMPyP with gold nanorods. As shown in Table 3.8, both systems of TMPyP's complex with ds-DNA on gold nanorods (0.061 ns) and of ds-DNA-functionalized nanorods with TMPyP (0.054 ns) have shorter decay components than ss-DNA functionalized nanorods (0.097) which agrees with the slight more fluorescence enhancement observed for the first two systems.

Table 3.8 Comparison of TCSCP of free TMPyP solution with the fluorescence burst in designed biosensor systems

System	Life Time 1 (Percentage)	Life Time 2 (Percentage)	Life Time 3 (Percentage)
$TMPyP^{+4}$ (1μM) in solution	5.7 ns (42.7%)	2.3 ns (53.9%)	0.1 ns (3.4%)
Complex-ds-DNA-TMPyP in	10.3	3.5	0.58

solution	(36.9%)	(52.6%)	(10.5%)
Complex-ss-DNA-TMPyP in solution	8.6 (32.9%)	3.0 (53.3%)	0.58 (13.8%)
Complex-ds-DNA-TMPyP Functionalized Single GNRs	7.8 ns (36.4%)	0.061 ns (48.8%)	1.525 ns (14.8%)
ds-DNA- Functionalized Single GNRs-TMPyP	8.7 ns (47.5%)	0.054 (41.6%)	1.524 (10.9%)
ss-DNA Functionalized Single GNRs-TMPyP	9.00 (39%)	0.097 (44%)	1.49 (17%)

And reversely, regarding lifetime 1 that corresponds to the decay rate of TMPyP dye, the ss-DNA Functionalized Single GNRs-TMPyP has a longer decay component (9.0 ns) than that of ds-DNA-Functionalized Single GNRs-TMPyP (8.7 ns) and of Complex-ds-DNA-TMPyP Functionalized Single GNRs (7.8 ns). These results (Figure 3.55) emphasize that there is interaction between DNA and TMPyP in vicinity of gold nanorods, but also show that complex-ds-DNA-TMPyP system is also more influenced by the interaction with the gold nanorods' surface. However, it cannot be discarded that the long decay components result from the emission of TMPyP molecules adsorbed onto the glass surrounding the nanorods, as it was confirmed by measuring the emission from an area of the glass cover slips without gold nanorods.

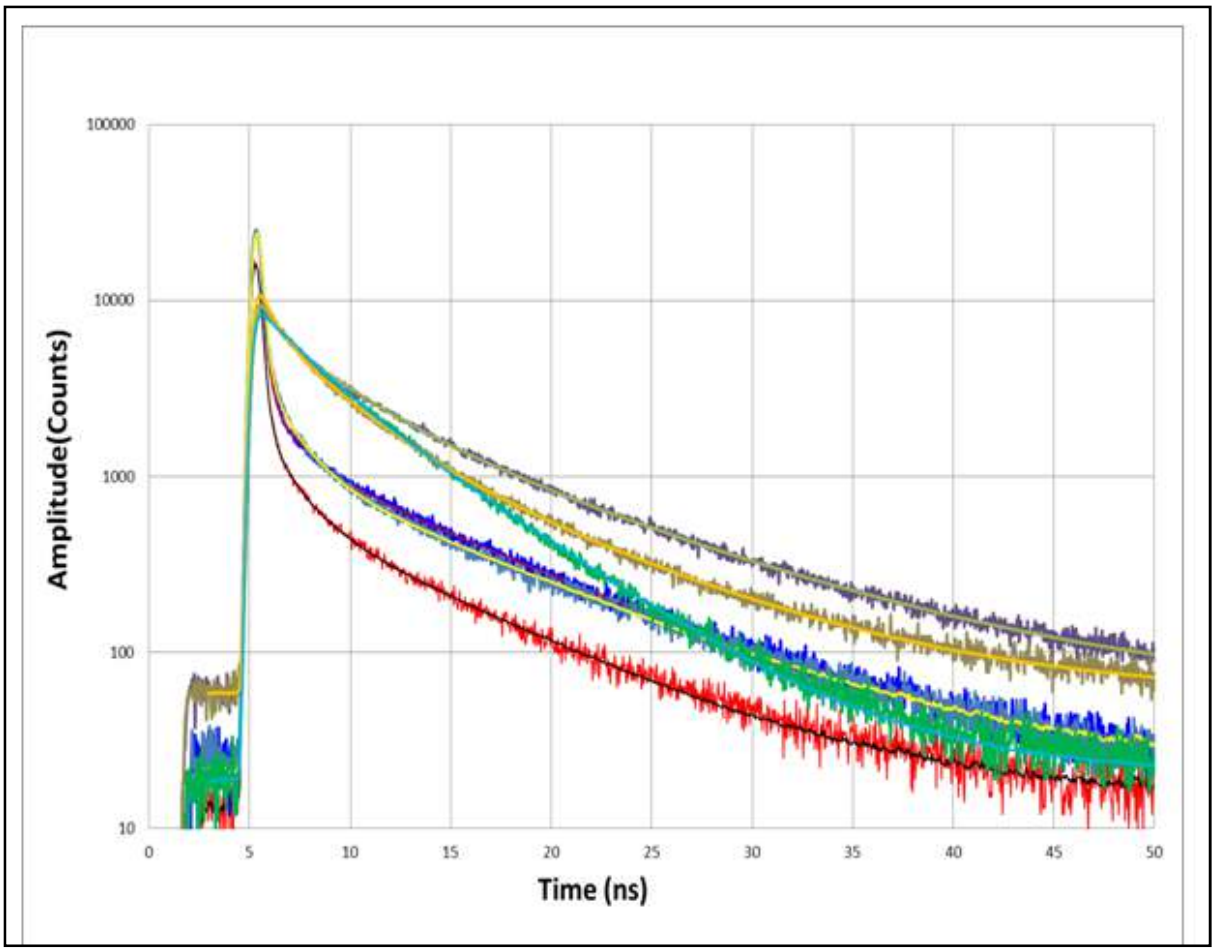

Figure 3.55 Comparison of TCSCP of Complex ds-Dengue DNA-TMPyP functionalized single gold nano rods –TMPyP (20 nM) (red), ss-Dengue DNA functionalized single gold nano rods-TMPyP (20 nM) (blue light), ds-Dengue DNA functionalized single gold nano rods-TMPyP (20 nM) (blue dark), Complex-ss-DNA-TMPyP in solution (orange), Complex-ds-DNA-TMPyP in solution (gray), TMPyP in solution (green).

5.5.4 Top Fluorescence Enhancement factor and Photoluminescence Intensity

There is a weak correlation between top fluorescence enhancement factors of porphyrin emission enhanced by single gold nanorods in our experiments and their photoluminescence intensity excited at both wavelengths of 480 nm (Figure 3.56) and 640 nm (Figure 3.57).

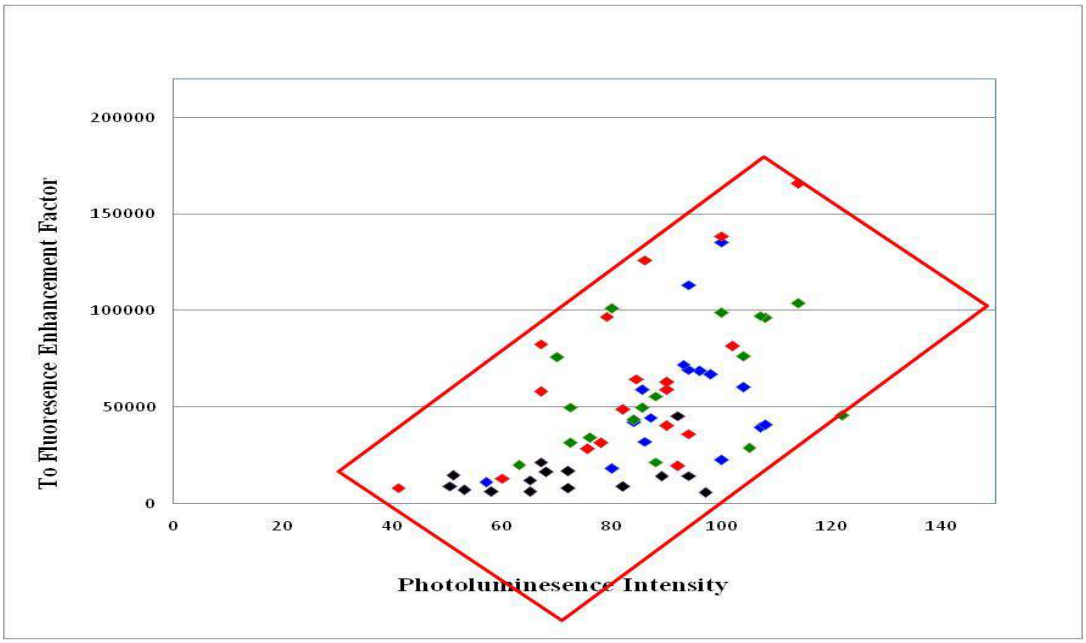

Figure 3.56 Top fluorescence enhancement factor versus the photoluminescence intensity of single gold nanorods excited at 480 nm for Complex-ds-DNA-TMPyP-Functionalized single GNRs (red), ds-DNA -Functionalized single GNRs -TMPyP (blue), ss-DNA -Functionalized single GNRs -TMPyP (green), AUT-functionalized single GNRs-TPPS (black)

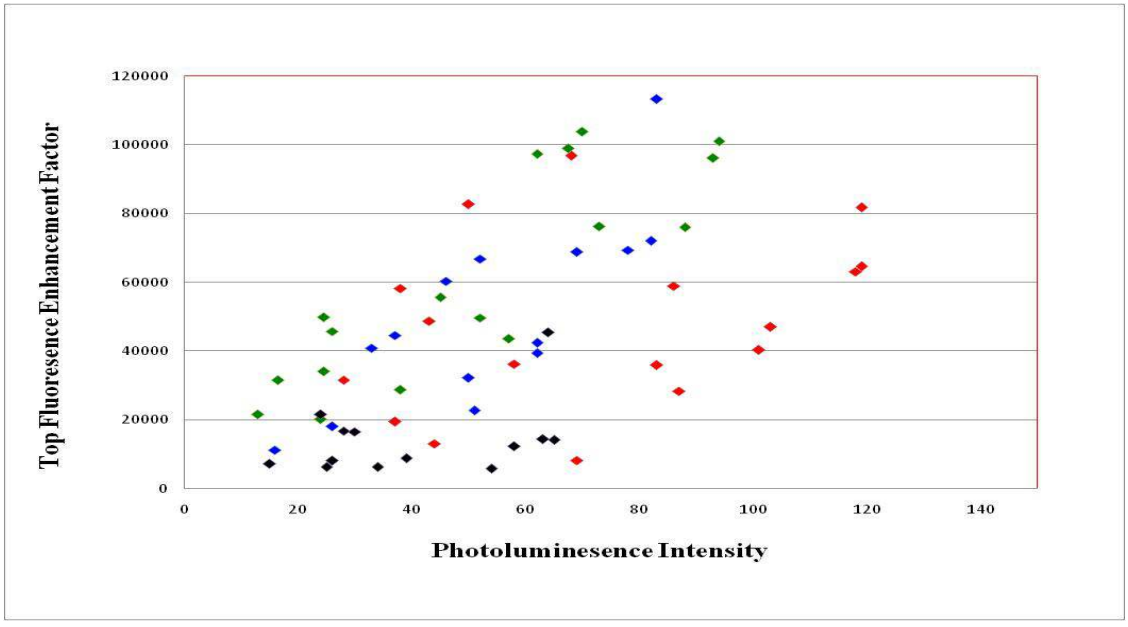

Figure 3.57 Top fluorescence enhancement factor versus the photoluminescence intensity of single gold nanorods excited at 640 nm for Complex-ds-DNA-TMPyP-Functionalized single GNRs (red), ds-DNA -Functionalized single GNRs -TMPyP (blue), ss-DNA -Functionalized single GNRs -TMPyP (green), AUT-functionalized single GNRs-TPPS (black)

4. Conclusions

The performance of label-free sensors strongly relies on the molecular interactions between the target species and the plasmonic particle. Consequently, tip-functionalization with higher concentration of bio-receptors seems to allow for a larger sensor response, as illustrated by our results on gold nanorods functionalized with biotin receptors for streptavidin sensing.

Using the designed gold nanorods-biotin-straptividin biosensor system trough the CTAB as a positive bilayer, the Dengue DNA tip-functionalization of gold nanorods was not achived because of electrostatic interations. However, for the full functionalization of gold nanorod with Dengue virus DNA, we obtained considerable plasmon response corresponding to the non-specifcally attachment of DNA to the gold nanorod' surface. Moreover, for full functionalization of gold nanorods with Dengue virus DNA using spacer to achive the specifically binding to the gold nanoparticles, no significant results were obtained and it need more efforts and overcommig more challenges in the future.

Based on the results of our experiments including Absorption, Emission and Time-Resolved-Spectroscopy, the interaction between ds-Dengue Virus DNA with TMPyP as well as ss-Dengue Virus DNA with TMPyP in solution show a specifc intercalation type of binding interactions that can be used in plasmon enhance fluorescence.

The plasmon enhancement of porphyrin fluorescence, surprisingly, showed top fluorescence enhancement factors that are approximately 2 order magnitude larger than the maximum enhancement effect theoretically predicted from model simulations. The mechanism of plasmon fluorescence enhancement can be mainly attributed to the increased excitation rate due to a local field enhancement effect and the increased emission rate by surface plasmon coupled emission. In addition, the photochemical properties of TMPyP combined with the DNA-coating on the nanorods allowed for a strong and prolonged interaction of the fluorescent molecule with the gold nano antenna, thus leading to more expressive fluorescence enhancements.

Bibliography

(1) Mehrotra, P. Biosensors and their applications–A review. *J. Ora.l Biol. Craniofac. Res.* **2016**, *6*, 153-159.
(2) Zhang, X.; Guo, Q.; Cui, D. Recent Advances in Nanotechnology Applied to Biosensors. *Sensors* **2009**, *9*, 1033-1053.
(3) McDermott, J. E.; Wang, J.; Mitchell, H.; Webb-Robertson, B.-J.; Hafen, R.; Ramey, J.; Rodland, K. D. Challenges in Biomarker Discovery: Combining Expert Insights with Statistical Analysis of Complex Omics Data. *Expert Opin. Med. Diagn.* **2013**, *7*, 37–51.
(4) Messina, J. P.; Brady, O. J.; Scott, T. W.; Zou, Ch.; Pigott, D. M.; Duda, K. A.; Bhatt, S.; Katzelnick, L.; Howes, R. E.; Battle, K. E.; Simmons, C. P.; Hay, S. I. Global spread of dengue virus types: mapping the 70 year history. *Trends Microbiol.* **2014**, *22*, 138-146.
(5) Kyle, J. L.; Harris, E. Global Spread and Persistence of Dengue. *Annu. Rev. Microbiol.* **2008**, *62*, 71-92.
(6) Simmons, C. P.; McPherson, K.; Chau, N. V. V.; Tam, D.T. H.; Young, P.; Mackenzie, J.; Wills, B. Recent advances in dengue pathogenesis and clinical management. *Vaccine* **2015**, *33*, 7061–7068.
(7) Parkash, O., Shueb. R. H., Diagnosis of Dengue Infection Using Conventional and Biosensor Based Techniques. *Viruses*, **2015**, *7*, 5410–542.
(8) Darwish, N. T.; Alias, Y. B.; Khor, S. M. An introduction to dengue-disease diagnostics. *Trends Analyt. Chem.* **2015**, *67*, 45–55.
(9) Zhang, B.; Salieb-Beugelaar, G.B.; Nigo, M. M. Diagnosing dengue virus infection: rapid tests and the role of micro/nanotechnologies. *Nanomedicine,* **2015**, *11*, 1745–1761.
(10) Nune, S. K.; Gunda, P.; Thallapally, P. K.; Lin, Y.-Y.; Forrest, M . L.; Berkland, C. J. Nanoparticles for biomedical imaging. *Expert Opin. Drug Deliv.* **2009**, *6*, *1175–1194.*
(11) Salata, O. Applications of nanoparticles in biology and medicine. *J. Nanobiotech.* **2004**, *2*, 1-6.
(12) Tokel, O.; Inci, F.; Demirci, U. Advances in Plasmonic Technologies for Point of Care Applications. *Chem. Rev.* **2014**, *114*, 5728–5752.
(13) Strobbia, P.; Languirand, E.; Cullum, B. M. Recent advances in plasmonic nanostructures for sensing: a review. *Opt. Eng.* **2015**, *54*, 1009021-21.
(14) Dykman, L. A.; Khlebtsov, N. G. Gold Nanoparticles in Biology and Medicine: Recent Advances and Prospects. Acta Naturae. **2011**, *3,* 34-55.
(15) Weibo Cai, Ting Gao, Hao Hong, Jiangtao Sun Applications of gold nanoparticles in cancer nanotechnology. *J. Nanosci. Nanotechnol.* **2008**, *1*, 17–32.
(16) Daniel, M. -C.; Astruc, D. Gold nanoparticles: Assembly, supramolecular chemistry, quantum-size-related properties, and applications toward biology, catalysis, and nanotechnology.*Chem. Rev.* **2003**, *104*, 293–346.
(17) Wagner, F. E.; Haslbeck, S.; Stievano, L.; Calogero, S.; Pankhurst, Q. A.; Martinek, K. -P. Before striking gold in gold-ruby glass. *Nature* **2000**, *407*, 691-692.
(18) Sekhar, M. C.; Rao, M. N.; Prasad, B. V. K.; Suryanarayana, S. V. 4 Vitality of Physics In Nanoscience and Nanotechnology *IOSR J. Appl. Phys.* **2015**, *7*, 1-5.
(19) Chen, P. C.; Mwakwari, S. C.; Oyeler, A. K. Gold nanoparticles: From nanomedicine to nanosensing. *Nanotechnol. Sci. Appl.* **2008**, *1*, 45–66.
(20) Verma, H. N.; Singh, P.; Chavan, R. M. Gold nanoparticle: synthesis and characterization. *Vet. World*, ***2014***, *7*, 72-77.
(21) Kabashin, A. V.; Meunier, M.; Kingston, C.; Luong, J. H. T.; Fabrication and Characterization of Gold Nanoparticles by Femtosecond Laser Ablation in an Aqueous Solution of Cyclodextrins. *J. Phys. Chem. B*, **2003**, *107*, 4527–4531.

(22) Sharma, N.; Bhatt, G.; Kothiyal, P. Gold Nanoparticles synthesis, properties, and forthcoming applications–A review. *Indian J. Pharm. Biol. Res*. **2015**; *3*, 13-27.
(23) Alshammari, A.; Köckritz, A.; Kalevaru, V. N.; Bagabas, A.; Martin, A. Influence of Single Use and Combination of Reductants on the Size, Morphology and Growth Steps of Gold Nanoparticles in Colloidal Mixture. *Open J. Phys. Chem.* **2012**, *2*, 252-261.
(24) Mayer, K. M.; Hafner, J. H. Localized Surface Plasmon Resonance Sensors. *Chem. Rev.* **2011**, *111*, 3828–3857.
(25) Willets, K. A.; Van Duyne, R. P. Localized surface plasmon resonance spectroscopy and sensing, *Annu. Rev. Phys. Chem.* **2007**, *58*, 267–297.
(26) Cao, J., Sun, T.; Grattan, K. T. V. Gold nanorod-based localized surface plasmon resonance biosensors: A review. Sens. Actuators B Chem.2014, 195, 332-351.
(27) Murphy, C. J.; Gole, A. M.; Hunyadi, S. E.; Stone, J. W.; Sisco, P. N.; Alkilany, A.; Kinard, B. E.; Hankins, P. Chemical sensing and imaging with metallic nanorods, *Chem. Commun.* **2008**, 544–557.
(28) Huang, X.; El-Sayed, I. H.; Qian, W.; El-Sayed, M. A. Cancer cell imaging and photothermal therapy in the near-infrared region by using gold nanorods, *J. Am. Chem. Soc.* **2006**, *128*, 2115–2120.
(29) Anker, J. N.; Hall, W. P.; Lyandres, O.; Shah, N. C.; Zhao, J.; Van Duyne, R. P. Biosensing with plasmonic nanosensors, Nat. Mater. **2008**, 7, 442–453.
(30) Hutter, E.; Fendler, J. H. Exploitation of localized surface plasmon resonance, *Adv. Mater.* **2004**, *16*, 1685–1706.
(31) Song, L.; Zhang, L.; Huang, Y.; Chen, L.; Zhang, G.; Zhang, J.; Xiao, Z.; Chen, T.; Shen, Z. Amplifying the signal of localized surface plasmon resonance sensing for the sensitive detection of Escherichia coli O157:H7. *Sci. Rep.* **2017**, *7*, 1-8.
(32) Huang, H.; He, C. C.; Zeng, Y. L.; Xia, X. D.; Yu, X. Y.; Yi, P. G.; Chen, Z. A novel labelfree multi-throughput optical biosensor based on localized surface plasmon resonance, Biosensors & Bioelectronics **2009**, *24*, 2255–2259.
(33) Mayer, K. M.; Hafner, J. H. Localized surface plasmon resonance sensors, *Chem. Rev.* **2011**, *111*, 3828–3857.
(34) Petryayeva, E.; Krull, U. J. Localized surface plasmon resonance: nanostructures, bioassays and biosensing–a review. *Anal. Chim. Acta.* **2011,** *706*, 8–24.
(35) Stetsenko, M. O.; Rudenko, S. P., Maksimenko, L. S.; Serdega, B. K.; Pluchery O.; Snegir, S. V. Optical Properties of Gold Nanoparticle Assemblies on a Glass Surface Nanoscale Res. Lett. **2017**, *12*, 1-10.
(36) Marinakos, S. M.; Chen, S.; Chilkoti, A. Plasmonic detection of a model analyte in serum by a gold nanorod sensor, *Anal. Chem.* **2007**, *79*, 5278–5283.
(37) Kajikawa, K.; Mitsui, K. Optical fiber biosensor based on localized surface plasmon resonance in gold nanoparticles, Nanosensing: Materials and Devices, *SPIE – Int. Soc. Optical Engineering*, Bellingham, **2004**, 494–501.
(38) Tian, L.; Morrissey, J. J.; Kattumenu, R.; Gandra, N.; Kharasch, E. D.; Singamaneni, S. Bioplasmonic Paper as a Platform for Detection of Kidney Cancer Biomarkers *Anal. Chem.* **2012**, *84*, 9928–9934.
(39) Zhai, S.; Zhao, H. Enhancement of Sensitivity of the Solution-Phase Localized Surface Plasmon by a Nanostructured Substrate. *M.R.S. Advances* **2016**, *1*, 2059-2064.

(40) Haes, A. J.; Stuart, D. A.; Nie, S.; Duyne, R. P. V. Using Solution-Phase Nanoparticles, Surface-Confined Nanoparticle Arrays and Single Nanoparticles as Biological Sensing Platforms. *J. Fluoresc.* **2004**, *14*, 355-367.
(41) Unser, S.; Bruzas, I.; He, J.; Sagle, L. Localized Surface Plasmon Resonance Biosensing: Current Challenges and Approaches. *Sensors* **2015**, *15*, 15684-15716.
(42) Guo, L.; Jackman, J. A., Yang, H. –H.; Chen, P.; Cho, N. –J.; Kim, D. –H. Strategies for enhancing the sensitivity of plasmonic nanosensors. *Nano Today*, **2015**, *10*, 213-239.
(43) Xie, Z. G.; Tao, J.; Lu, Y. H.; Lin, K. Q.; Yan, J.; Wang, P.; Ming, H. Polymer optical fiber SERS sensor with gold nanorods, *Opt. Commun.* **2009**, *282*, 439–442.
(44) Murphy, C. J.; Gole, A. M.; Hunyadi, S. E.; Stone, J. W.; Sisco, P. N.; Alkilany, A.; Kinard, B. E.; Hankins, P. Chemical sensing and imaging with metallic nanorods, *Chem. Commun.* **2008**, 544–557.
(45) Huang, X.; El-Sayed, I. H.; Qian, W.; El-Sayed, M. A. Cancer cell imaging and photothermal therapy in the near-infrared region by using gold nanorods, *J. Am. Chem. Soc.* **2006**, *128*, 2115–2120.
(46) P.; Zijlstra, P. M. R.; Paulo, K.; Yu, Xu, Q. -H.; Michel, O. Chemical Interface Damping in Single Gold Nanorods and Its Near Elimination by Tip-Specific Functionalization. *Angew. Chem. Int. Ed.* **2012**, *51*, 835–8355.
(47) Vigderman, L.; Khanal, B. P.; Zubarev, E. R. Functional Gold Nanorods: Synthesis, Self-Assembly, and Sensing Applications.*Adv. Mater.* **2012**, *24*, 4811–4841.
(48) Eustis, S.; El-Sayed, M. A. Determination of the aspect ratio statistical distribution of gold nanorods in solution from a theoretical fit of the observed inhomogeneously broadened longitudinal plasmon resonance absorption spectrum. *J. Appl. Phys.* **2006**, *100*, 0443241-0443247.
(49) Paulo P. M. R.; Zijlstra P.; Orrit .; Garcia-Fernandez, E.; Pace T. C. S.; Viana, A. S.; Costa S. M. B. Tip-Specific Functionalization of Gold Nanorods for Plasmonic Biosensing: Effect of Linker Chain Length. *Langmuir* **2017**, *33*, 6503-6510.
(50) Nguyen, H. H.; Park, J.; Kang, S.; Kim, M. Surface Plasmon Resonance: A Versatile Technique for Biosensor Applications. *Sensors,* **2015**, *15*, 10481-10510.
(51) Wang, H.; Wang, X.; Wang, J.; Fu, W.; Yao, C. A SPR biosensor based on signal amplification using antibody-QD conjugates for quantitative determination of multiple tumor markers. *Sci. Rep.* **2016**, *6*,1-9.
(52) Helmerhorst, Er.; Chandler, D. J.; Nussio, M.; Mamotte, C. D. Real-time and Label-free Bio-sensing of Molecular Interactions by Surface Plasmon Resonance: A Laboratory Medicine Perspective.*Clin. Biochem. Rev.* **2012**, *33*,161-173.
(53) Rich, R. L.; Myszka, D. G. Advances in surface plasmon resonance biosensor analysis.*Curr. Opin. Biotechnol.* **2000**, *11*, 54-61.
(54) Haes, A. J.; Duyne, R. P. V. Preliminary studies and potential applications of localized surface plasmon resonance spectroscopy in medical diagnostics. *Expert Rev. Mol. Diagn.* **2004**, *4*, 527–537.
(55) A.; Chilkoti, Stayton, P. S. Molecular Origins of the Slow Streptavidin-Biotin Dissociation Kinetics. *J. Am. Chem. Soc.* **1995**, *117*, 10622-10628.

(56) A. C.; Weber, Ohlendorf, D. H.; Wendoloski, J. J.; Salemme, F. R. *Science*, **1989**, *243*, 85-88.
(57) Klumb, L. A.; Chu, V.; Stayton, P. S. Energetic Roles of Hydrogen Bonds at the Ureido Oxygen Binding Pocket in the Streptavidin-Biotin Complex. *Inorg. Chem.* **2006**, *45*, 660–668.
(58) Sano, T.; Cantor, C. R. Cooperative Biotin Binding by Streptavidin. **1990,** *265*, 3369-3373.
(59) Liu, W.; Samanta, S. K.; Smith, B. D.; Isaacs, L. Synthetic mimics of biotin/(strept)avidin.*Chem. Soc. Rev.* **2017**, *46*, 2391-2403.
(60) Dundas, C. M.; Demonte, D.; Park, S. Streptavidin–biotin technology: improvements and innovations in chemical and biological applications. *Appl. Microbiol. Biotechnol.* **2013**, *97*, 9343–9353.
(61) Jung, L. S.; Nelson, K. E.; Stayton, P. S.; Campbell. C. T. Binding and Dissociation Kinetics of Wild-Type and Mutant Streptavidins on Mixed Biotin-Containing Alkylthiolate Monolayers. *Langmuir* **2000**, *16*, 9421–9432.
(62) Marinakos, S. M.; Chen, S. H.; Chilkoti, A. Plasmonic detection of a model analyte in serum by a gold nanorod sensor. *Anal. Chem.* **2007**, *79*, 5278-83.
(63) Detection of a Biomarker for Alzheimer's Disease from Synthetic and Clinical Samples Using a Nanoscale Optical Biosensor. *J. Am. Chem. Soc.* **2005**, *127*, 2264-2271.
(64) Cappi, G.; Spiga, F. M.; Moncada, Y.; Ferretti, A.; Beyeler, M.; Bianchessi, M.; Decosterd, L.; Buclin, T.; Guiducci, C. Label-Free Detection of Tobramycin in Serum by Transmission-Localized Surface Plasmon Resonance. *Anal.Chem.* **2015**, *87*, 5278−5285.
(65) Jin-Ho Park, Ju-Young Byun, Hyoyoung Mun, Won-Bo Shim, Yong-Beom Shin, Taihua Li, Min-Gon Kim A regeneratable, label-free, localized surface plasmon resonance (LSPR) aptasensor for the detection of ochratoxin A. *Biosens. Bioelectron.* **2014**, *59*, 321–327.
(66) Mayer, K. M.; Hao, F.; Lee, S.; Nordlander, P.; Hafner, J. H. A single molecule immunoassay by localized surface plasmon resonance. *Nanotechnology* **2010**, *21*, 1-8.
(67) Xu, X.; Ying, Y.; Li, Y. Gold Nanorods Based LSPR Biosensor for Label-Free Detection of Alpha-Fetoprotein. *Procedia Eng.* **2011,** 25, 67–70.
(68) Kim, D.; Kim, J.; Kwak,C. H.; Heo, N. S.; Oh, S. Y.; Lee, H.; Lee, G. –W.; Vilian, A. T. E.; Han, Y. –K.; Kim, W. –S.; Kim, G. –B.; Kwon, S.; Huh, Y. S. Rapid and label-free bioanalytical method of alpha fetoprotein detection using LSPR chip. *J. Cryst. Growth.* **2017**, *469*, 131-135.
(69) Syahir, A.; Usui, K.; Tomizaki, K. –Y.; Kajikawa, K.; Mihara, H. Label and Label-Free Detection Techniques for Protein Microarrays. *Microarrays* **2015**, *4*, 228-244.
(70) Phelan, M. L.; Nock, S. Generation of bioreagents for protein chips. Proteomics **2003**, 3, 2123–2134.
(71) Fong, C. -C.; Lai, W. -P.; Leung, Y. -C.; Lo, S. C. -L.; Wong, M. -S.; Yang, M. Study of substrate-enzyme interaction between immobilized pyridoxamine and recombinant porcine pyridoxal kinase using surface plasmon resonance biosensor. *Biochim. Biophys. Acta* **2002**, *1596*, 95–107.
(72) Bora, U.; Sett, A.; Singh, D. Nucleic Acid Based Biosensors for Clinical Applications. *Biosens. J.* **2013**, *2*, 1-8.

(73)Sassolas, A.; Leca-Bouvier, B. D.; Blum, L. J. DNA Biosensors and Microarrays. *Chem. Rev.* **2008**, *108*, 109-139.
(74) Samanta, A.; Medintz I. L. Nanoparticles and DNA– a powerful and growing functional combination in bionanotechnology. *Nanoscale* **2016**, *8*, 9037–9095.
(75) Arruebo, M.; Valladares, M.; Gonzalez-Fernandez, A. Antibody-Conjugated Nanoparticles for Biomedical Applications. *J. Nanomater.* **2009**, *2009*, 1-24.
(76) Kairdolf, B. A.; Qian, X.; Nie, S. Bioconjugated Nanoparticles for Biosensing, in Vivo Imaging, and Medical Diagnostics *Anal. Chem.* **2017**, *89*, 1015–1031.
(77) Wang, H.; Yang, R.; Yang, L.; Tan, W. Nucleic Acid Conjugated Nanomaterials for Enhanced Molecular Recognition. *A.C.S. Nano.* **2009**, *3*, 2451–2460.
(78) K. M.; Abu-Salah, S. A.; Alrokyan, Khan, M. N.; Ansari, A. A. Nanomaterials as Analytical Tools for Genosensors *Sensors* **2010**, *10*, 963-993.
(79) Glynou, K.; Ioannou, P.C.; Christopoulos, T.K.; Syriopoulou, V. ODN-functionalized gold nanoparticles as probes in a dry-reagent strip biosensor for DNA analysis by hybridization. *Anal. Chem.* **2003**, *75*, 4155-4160.
(80) Csáki, A.; Möller, R.; Fritzsche, W. Gold nanoparticles as novel label for DNA diagnostics. *Expert Rev. Mol. Diagn.***2002**, *2*, 187–193.
(81) Chen, G.; Roy, I.; Yang, C.; Prasad, P. N. Nanochemistry and Nanomedicine for Nanoparticle-based Diagnostics and Therapy. *Chem. Rev.* **2016**, *116*, 2826−2885.
(82) K. E.; Fong, Yung, L. –Y. L. Localized surface plasmon resonance: a unique property of plasmonic nanoparticles for nucleic acid detection. *Nanoscale*, **2013**, *5*, 12043-12071.
(83) Miao, X.; Ning, X.; Li, Z.; Cheng, Z. Sensitive detection of miRNA by using hybridization chain reaction coupled with positively charged gold nanoparticles.*Sci. Rep.* ***2016***, *6*, 1-9.
(84) Joshi, G. K.; Deitz-McElyea, S.; Johnson, M.; Mali, S.; Korc, M.; Sardar, R. Highly Specific Plasmonic Biosensors for Ultrasensitive MicroRNA Detection in Plasma from Pancreatic Cancer Patients. *Nano Lett.* **2014**, *14*, 6955−6963.
(85) Soares, L.; Csaki, A.; Jatschka J.; Fritzsche, W.; Flores, O.; Franco, R.; Pereira, E.; Localized surface plasmon resonance (LSPR) biosensing using gold nanotriangles: detection of DNA hybridization events at room temperature. *Analyst* **2014**, *139*, 4964-4973.
(86) Guo, L.; Jackman, J. A.; Yang, H. –H.; Chen, P.; Cho, N. -J.; Kim, D. -H. Strategies for enhancing the sensitivity of plasmonic nanosensors. *Nano Today* **2015**, *10*, 213-239.
(87) Ishihara, S.; Minami, K.; Labuta, J.; Hill, J. P.; Rossom, W. V.; Ishikawa, D.; Ariga, K. Porphyrin-based sensor nanoarchitectonics in diverse physical detection modes. *Phys. Chem. Chem.Phys.* **2014**, *16*, 9713-9746.
(88) Costa, L. D.; Costa, J. I. T.; Tomé, A. C. Porphyrin Macrocycle Modification: Pyrrole Ring-Contracted or -Expanded Porphyrinoids. *Molecules* **2016**, *21*, 320-350.
(89) Grand, C. L.; Han H.; Muñoz, R. M.; Weitman, S.; Von Hoff, D. D.; Hurley, L. H.; Bearss D. J. The cationic porphyrin TMPyP4 down-regulates

c-MYC and human telomerase reverse transcriptase expression and inhibits tumor growth in vivo. *Mol. Cancer Ther.* **2003**, *2*, 208.
(90) McCormick, B. P. P.; Pansa, M. F.; Sanabria, L. N. M.; Carvalho, C. M. B.; Faustino, A. M. F.; Neves, M. G. P. M. S.; Rivarola, V. A.; Cavaleiro, J. A. S.; Vittar, N. B. R. Cationic porphyrin derivatives for application in photodynamic therapy of cancer. *Laser Phys.* **2014**, *24*, 1-8.
(91) Cordeiro R. M.; Miotto, R.; Baptista M. S. Photodynamic efficiency of cationic meso-porphyrins at lipid bilayers: insights from molecular dynamics simulations. *J. Phys. Chem. B.* **2012**, *116*, 14618-14627.
(92) Ding, Y.; Zhu, W. –H.; Xie, Y. Development of Ion Chemosensors Based on Porphyrin Analogues. *Chem. Rev.* **2017**, *117*, 2203−2256.
(93)Vidic, J.; Manzano, M.; Chang, C. -M.; Jaffrezic-Renault, N. Advanced biosensors for detection of pathogens related to livestock and poultry. *Vet. Res.* **2017**, *48*, 1-22.
(94) Sin, M. L. Y.; K. E.; Mach, P. K.; Wong, J. C. Liao, Advances and challenges in biosensor-based diagnosis of infectious diseases. *Expert Rev. Mol. Diagn.* **2014,** *14*, 225–244.
(95) Borissevitch, I. E.; Shirley C. M. Gandini Photophysical studies of excited-state characteristics of meso-tetrakis (4-N-methyl-pyridiniumyl) porphyrin bound to DNA. *J. Photochem. Photobiol. B, Biol.* **1998**, *43*, 112-120.
(96) Fiel, R. J. Porphyrin—Nucleic Acid Interactions: A Review. *J. Biomol. Struct. Dyn.* **1989**, *6*, 1259-1274.
(97) Mettath, S.; Munson, B. R.; Pandey, R. K. DNA Interaction and Photocleavage Properties of Porphyrins Containing Cationic Substituents at the Peripheral Position. *Bioconjugate Chem.* **1999**, *10*, 94-102.
(98) McMillin, D. R.; Shelton, A. H.; Bejune, S. A.; Fanwick, P. E.; Wall, R. K. Understanding binding interactions of cationic porphyrins with B-form DNA. *Coord. Chem. Rev.* **2005**, *249*, 1451–1459.
(99) Cenklová, V. Photodynamic therapy with TMPyP–Porphyrine induces mitotic catastrophe and microtubule disorganization in HeLa and G361 cells, a comprehensive view of the action of the photosensitizer. *J. Photochem. Photobiol. B, Biol.* **2017**, 173, 522–537.
(100) Lee, Y. –A.; Lee, S.; Cho, T. –S.; Kim, C.; Han, S. W.; Kim, S. K. Binding Mode of meso-Tetrakis(N-methylpyridinium-4-yl)porphyrin to Poly[d(I-C)]: Effect of Amino Group at the Minor Groove of Poly[d(G-C)] on the Porphyrin-DNA Interaction. *J. Phys. Chem. B*, **2002**, *106*, 11351-11355.
(101) F. X.; Han, Wheelhouse, R. T.; Hurley L. H. Interactions of TMPyP4 and TMPyP2 with Quadruplex DNA. Structural Basis for the Differential Effects on Telomerase Inhibition. *J. Am. Chem. Soc.* **1999**, *121*, 3561-3570.
(102) Hui, X.; Gresh, N.; Pullman, B. Modelling of the binding specificity in the interactions of cationic porphyrins with DNA. *Nucleic Acids Res.* **1990**, *18*, 1109-1114.
(103) Murat, P.; Singh, Y.; Defrancq, E. Methods for investigating G-quadruplex DNA/ligand interactions. *Chem. Soc. Rev.* **2011**, *40*, 5293–5307.
(104) Lee, Y. –A.; Kim, J. –O.; Cho, T. –S.; Song, R.; Kim, S. K. Binding of meso-Tetrakis(N-methylpyridium-4-yl)porphyrin to Triplex Oligonucleotides: Evidence for the Porphyrin Stacking in the Major Groove. *J. Am. Chem. Soc.* **2003**, *125*, 8106-8107.
(105) Yun, B. H.; Jeon, S. H.; Cho, T-. S.; Yi, S. Y.; Sehlstedt, U.; Kim, S. K. Binding mode of porphyrins to poly[d(A-T)2] and poly[d(G-C)2]. *Biophys. Chem.* **1998**, *70*, 1-10.
(106) Bonneau,S.; Vever-Bizet, C.; Morliere, P.; Maziere, J-. C.; Brault, D. Equilibrium and Kinetic Studies of the Interactions of a Porphyrin with Low-Density Lipoproteins. *Biophys. J.* **2002**, *83*, 3470–3481.

(107) Borjesson, K.; Wiberg, J.; El-Sagheer, A. H.; Ljungdahl, T.; Martensson, Je.; Brown, T.; Norden, B.; Albinsson, B. Functionalized Nanostructures: Redox-Active Porphyrin Anchors for Supramolecular DNA Assemblies. *A.C.S. Nano* **2010**, *4*, 5037–5046.
(109) Carvlin, M. J.; Datta-Gupta, N.; Fiel, R. J. Circular Dichroism Spectroscopy of a Cationic Porphyrin Bound to DNA. *Biochem. Biophys. Res. Commun.* **1982**, *108*, 66-73.
(110) Pasternack, R. F.; Goldsmith, J. I.; Szep, S.; Gibbs, E. J. A Spectroscopic and Thermodynamic Study of Porphyrin/DNA Supramolecular Assemblies. *Biophys.* **1998**, *75*, 1024–1031.
(111) Thomas, K. G.; Kamat, P. V. Chromophore-functionalized gold nanoparticles. *Acc. Chem. Res.* **2003**, *36*, 888-898.
(112) Imahori, H.; Kashiwagi, Y.; Endo, Y.; Hanada, T.; Nishimura, Y.; Yamazaki, I.; Araki, Y.; Ito, O.; Fukuzumi, S. Structure and photophysical properties of porphyrin-modified metal nanoclusters with different chain lengths. *Langmuir* **2004**, *20*, 73-81.
(113) Kalachyova, Y.; Lyutakov, O.; Solovyev, A.; Slepi, P.; Švorčík, V. Surface morphology and optical properties of porphyrin/Au and Au/porphyrin/Au systems. *Nanoscale Res. Lett.* **2013**, *8*, 1-10.
(114) Miyachi, M.; Yamanoi, Y.; Nakazato, K.; Nishihara, H. Bio-inspired photoresponse of porphyrin-attached gold nanoparticles on a field-effect transistor. *Biochim. Biophys. Acta* **2014**, *1837*, 1567–1571.
(115) Shaikh, A. J.; Rabbani, F.; Sherazi, T. A.; Iqbal, Z.; Mir, S.; Shahzad, S. A. Binding Strength of Porphyrin−Gold Nanoparticle Hybrids Based on Number and Type of Linker Moieties and a Simple Method To Calculate Inner Filter Effects of Gold Nanoparticles Using Fluorescence Spectroscopy. *J. Phys. Chem. A.* **2015**, *119*, 1108-1116.
(116) A.; Kotiaho, R.; Lahtinen, H.; Lehtivuori, N. V.; Tkachenko, H. Lemmetyinen Photoinduced Energy and Charge Transfer in Layered Porphyrin-Gold Nanoparticle Thin Films. *J. Phys. Chem. C* **2008,***112*, 10316–10322.
(117) Kotiaho, A.; Lahtinen, R. M.; Tkachenko, N. V.; Efimov, A.; Kira, A.; Imahori, H.; Lemmetyinen, H. Gold Nanoparticle Enhanced Charge Transfer in Thin Film Assemblies of Porphyrin-Fullerene Dyads. *Langmuir* **2007**, *23*, 13117-13125.
(118) Templeton, A. C.; Cliffel, D. E.; Murray, R. W. Redox and Fluorophore Functionalization of Water-Soluble, Tiopronin-Protected Gold Clusters. *J. Am. Chem. Soc.* **1999**, *121*, 7081-7089.
(119) Hernandez, F. E.; Yu, S.; M.; Garcıa, Andres, D. Campiglia Fluorescence Lifetime Enhancement of Organic Chromophores Attached to Gold Nanoparticles. *J. Phys. Chem. B* **2005**, *109*, 9499-9504.
(120) Saini, S.; Srinivas, G.; Bagchi, B. Distance and Orientation Dependence of Excitation Energy Transfer: From Molecular Systems to Metal Nanoparticles. *J. Phys. Chem. B* **2009,** *113,* 1817–1832.
(121) Bhowmick, S.; Saini, S.; Shenoy, V. B. Bagchi,B. Resonance energy transfer from a fluorescent dye to a metal nanoparticle. *J. Chem. Phys.* **2006**, *125*, 181102-181102.
(122) Dulkeith, E.; Morteani, A. C.; Niedereichholz, T.; Klar, T. A.; Feldmann, J. Fluorescence Quenching of Dye Molecules near Gold Nanoparticles: Radiative and Nonradiative Effects. *Phys. Rev. Lett.* **2002**, *89*, 203002-203004.
(123) Dulkeith, E.; Ringler, M.; Klar, T. A.; Feldmann, J.; Javier, A. M.; Parak, W. J. Gold Nanoparticles Quench Fluorescence by Phase Induced Radiative Rate Suppression. *Nano Lett.* **2005**, *5*, 585-589.
(124) Thomas, K. G.; Kamat, P. V. Chromophore-Functionalized Gold Nanoparticles. *Acc. Chem. Res.* **2003**, *36*, 888-898.
(125) Samanta, D.; Sarkar, A. Immobilization of bio-macromolecules on self-assembled monolayers: methods and sensor applications. *Chem. Soc. Rev.* **2011**, *40*, 2567–2592.

(126) Conde, J.; Dias, J. T.; Grazú, V.; Moros, M.; Baptista, P. V.; dela Fuente, J. M. Revisiting 30 years of biofunctionalization and surface chemistry of inorganic nanoparticles for nanomedicine. *Front. Chem*. **2014**, *2*,1-27.
(127) Fischer, U. C.; Hentschel, C.; Fontein, F.; Stegemann, L.; Hoeppener, C.; Fuchs, H.; Hoeppener, S. Near-field photochemical and radiation-induced chemical fabrication of nanopatterns of a self-assembled silane monolayer. *Beilstein J. Nanotechnol.* **2014**, *5*, 1441–1449.
(128) Kim, D.; Carroll, D. L.Roles of Au and Ag nanoparticles in efficiency enhancement of poly(3-octylthiophene)/bulk heterojunction photovoltaic devices *Appl. Phys. Lett.* **2005**, *87*, 203113-3.
(129) Chen, S. F.; Cheng, F.; Mei, Y.; Peng, B.; Kong, M.; Hao, J. Y.; Zhang, R.; Xiong, Q. H.; Wang, L. H.; Huang, W. Plasmon-enhanced polymer photovoltaic cells based on large aspect ratio gold nanorods and the related working mechanism. *Appl. Phys. Lett.* **2014**, *104*, 213903-5.
(130) Park, J. H.; Lim, Y. T.; Park, O.; Kim, Y. C. Enhancement of Photostability in Blue-Light-Emitting Polymers Doped with Gold Nanoparticles. *Macromol. Rapid Commun.* **2003**, *24*, 331–334.
(131) Wu, S. –H.; Huang, H.- M.; Chen, K. –C.; Hu, C. –W.; Hsu, C. –C.; Tsiang, R. C.- C. A Green Polymeric Light-Emitting Diode Material: Poly(9,9-dioctylfluorene-alt-thiophene) End-Capped with Gold Nanoparticles. *Adv. Funct. Mater.* **2006**, *16*, 1959–1966.
(132) Kotiaho, A.; Lahtinen, R. M.; Kira, A.; Imahori, H.; Tkachenko, N. V.; Efimov, A.; Lemmetyinen, H. Gold Nanoparticle Enhanced Charge Transfer in Thin Film Assemblies of Porphyrin-Fullerene Dyads. *Langmuir* **2007**, *23*, 13117-13125.
(133) Imahori, A.H.; Fujimoto, A.; Kang, S.; Hotta, H.; Yoshida, K.; Umeyama, T.; Matano, Y.; Isoda, S.; Isosomppi, M.; Tkachenko, N. V.; Lemmetyinen, H. Host–Guest Interactions in the Supramolecular Incorporation of Fullerenes into Tailored Holes on Porphyrin-Modified Gold Nanoparticles in Molecular Photovoltaics. *J. Phys. Chem. C* **2008,** *112,* 10316–10322.
(134) Kotiaho, A.; Lahtinen, R.; Lehtivuori, H.; Tkachenko, N. V.; Lemmetyinen, H. Photoinduced Energy and Charge Transfer in Layered Porphyrin-Gold Nanoparticle Thin Films. *J. Phys. Chem. C* **2008,** *112,* 10316–10322.
(135) Akiyama, T.; Nakada, M.; Terasaki, N.; Yamada, S. Photocurrent enhancement in a porphyrin-gold nanoparticle nanostructure assisted by localized plasmon excitation. *Chem. Commun.* **2006**, 395–397.
(136) Matsumoto, R.; Yamada, S.; Yonemura, H. Effects of Gold Nanoparticles on Photocurrents of Zinc-Porphyrin-Viologen Linked Compound–Gold Nanoparticle Composite Films. *Mol. Cryst. Liq. Cryst.* **2014**, 598, 86–91.
(137) Schwab, A.D.; Smith, D.E.; Bond-Watts, B.; Johnston, D.E.; Hone, J.; Johnson, A.T.; de Paula, J.C.; Smith, W.F. Photoconductivity of self-assembled porphyrin nanorods. *Nano Lett.* **2004**, *4*, 1261–1265.
(138) Hu PG, Chen LM, Kang XW, Chen SW. Surface Functionalization of Metal Nanoparticles by Conjugated Metal-Ligand Interfacial Bonds: Impacts on Intraparticle Charge Transfer. *Accounts Chem Res.* **2016**, *49*, 2251-60.
(139) Kotiaho, A.; Lahtinen, R.; Lemmetyinen, H. Photoinduced processes in chromophore–gold nanoparticle assemblies. *Pure Appl. Chem.* **2011**, *83*, 813–821.
(140) Ishijima, A.; Yanagida, T. Single molecule nanobioscience.*TRENDS Biochem. Sci.* **2001**, *26*, 439-444.
(141) Ishii, Y.; Yanagida, T. Single Molecule Detection in Life Science. *Single Mol.* **2000**, *1*, 5-16.
(142) Weiss, S. Measuring conformational dynamics of biomolecules by single molecule fluorescence spectroscopy. *Nat. struct. biol.* **2000**, *7*, 424-429.

(143) Wang, H.; Branton, D. Nanopores with a spark for single-molecule detection. *Nat. Biotech.* **2001**, *19*, 622–623.
(144) Zlatanova1, J.; Holde, K. V. Single-Molecule Biology: What Is It and How Does It Work? *Molecular Cell* **2004**, *24*, 317–329.
(145) Peterson,E. M.; Manhart, M. W.; Harris, J. M. Single-Molecule Fluorescence Imaging of Interfacial DNA Hybridization Kinetics at Selective Capture Surfaces. *Anal. Chem.* **2016**, *88*, 1345–1354.
(146) Pitchiaya, S.; Heinicke, L. A.; Park, J. I.; Cameron, E. L.; Walter, N. G. Resolving Subcellular miRNA Trafficking and Turnover at Single-Molecule Resolution. *Cell Rep.* **2017**, *19*, 630–642.
(147) Kim, E.; Baaske, M. D.; Schuldes, I.; Wilsch, P. S.; Vollmer,F. Label-free optical detection of single enzyme-reactant reactions and associated conformational changes. *Sci. Adv.* **2017**, *3*, 1-8.
(148)Arjmandi-Tash, H.; Belyaeva, L. A.; Schneider,G. F. Single molecule detection with graphene and other two-dimensional materials: nanopores and beyond. *Chem. Soc. Rev.* **2016**, *45*, 476-493.
(149) Walt, D. R. Optical Methods for Single Molecule Detection and Analysis. *Anal. Chem.* **2013**, *85*, 1258−1263.
(150) Kumar, V. Single Molecule Detection Using Nanoprobe Technology. *Res. Rev. J. Pharm. Pharm. Sci.* **2015**, *3*, 1-5.
(151) Sriram, M.; Zong, K.; Vivekchand, S. R. C.; Justin, J. GoodingSingle Nanoparticle Plasmonic Sensors. *Sensors* **2015**, *15*, 25774-25792.
(152) Mauranyapin, N. P.; Madsen, L. S.; Taylor, M. A.; Waleed, M.; Bowen, W. P. Evanescent single-molecule biosensing with quantum-limited precision. *Nat. Photon.* **2017**, *11*, 477–481
(153) König, I.; Zarrine-Afsar, A.; Aznauryan, M.; Soranno, A.; Wunderlich, B.; Dingfelder, F.; Stüber, J. C.; Plückthun, A.; Nettels, D.; Schuler, B. Single-molecule spectroscopy of protein conformational dynamics in live eukaryotic cells. *Nat. Methods* **2015**, *12*, 773-779.
(154) Moerner, W. E.; Kador, L. *Optical detection and spectroscopy of single molecules in a solid. Phys. Rev. Lett.* **1989**, *62*, 2535–2538.
(155) Orrit, M.; Bernard, J. *Single pentacene molecules detected by fluorescence excitation in a p-terphenyl crystal. Phys. Rev. Lett.* **1990**, *65*, 2716–2719.
(156) Myers, A. B.; Tchénio, P.; Zgierski, M. Z.; Moerner, W. E. *Vibronic spectroscopy of individual molecules in solids. J. Phys. Chem.* **1994**, *98*, 10377–10390.
(157) Feist, F. A.; Basché, T. *Fluorescence excitation and emission spectroscopy on single MEH-PPV chains at low temperature.J. Phys. Chem. B* **2008**, *112*, 9700–9708.
(158) Feist, F. A.; Tommaseo, G.; Basché, T. *Observation of very narrow linewidths in the fluorescence excitation spectra of single conjugated polymer chains at 1.2 K. Phys. Rev. Lett.* **2007**, *98*, 208301–208305.
(159) Nie, S.; Zare, R. N. Optical detection of single molecules comprises both frequency-modulated absorption and laser-induced fluorescence. *Annu. Rev. Biophys. Biomol. Struct.* **1997**, *26*, 567–596.
(160) https://en.wikipedia.org/wiki/Jablonski_diagram.
(161) Ha, T.; Tinnefeld, P. Photophysics of Fluorescence Probes for Single Molecule Biophysics and Super-Resolution Imaging.*Annu. Rev. Phys. Chem.* **2012**, *63*, 595–617.
(162) Chen, R.; Wu, R.; Zhang, G.; Gao, Y.; Xiao, L.; Jia, S. Electron Transfer-Based Single Molecule Fluorescence as a Probe for Nano-Environment Dynamics *Sensors* **2014**, *14*, 2449-2467.
(163) Walt, D. R. Optical methods for single molecule detection and analysis. *Anal Chem.* **2013**, *85*, 1258–1263.

(164) Handbook of Biological Confocal Microscopy. Ed.: J. Pawley. 3rd edition. Springer US, **2006**.
(165) Paddock S.W. Confocal Microscopy Methods and Protocols: Methods in Molecular Biology. Ed Paddock SW. Humana Press; **1999**.
(166) Hibbs, A. R. Confocal Microscopy for Biologists, New York. Kluwer Academic/Plenum Publishers, **2004**.
(167) Matsumoto B. (ed.), Cell Biological Applications of Confocal Microscopy , in Methods in Cell Biology, Volume 70, New York: Academic Press, **2002**
(168) Conn, P. M. Confocal Microscopy, in Methods in Enzymology. Volume 307, New York: Academic Press, **1999**.
(169) Periasamy, A. Methods in Cellular Imaging. Oxford University Press, New York. 5. **2001**.
(170) Hansma, H. G.; Kim, K. J.; Laney, D. E.; Garcia, R. A.; Argaman, M.; Allen, M. J.; Parsons, S. M. Properties of biomolecules measuredfrom atomic force microscope images: a review. *J. Struct. Biol.* **1997**, *119*, 99-108.
(171) Hansma, H. G. Surface biology of DNA by atomic force microscopy. *Annu. Rev. Phys. Chem.* **2001**, *52*, 71-92.
(172) Engel, A.; Lyubchenko, Y.; and Muller, D. Atomic force microscopy: a powerful tool to observe biomolecules at work. *Trends Cell Biol.* **1999**, *9*, 77-80.
(173) Betzig, E.; Chichester, R. J. Single molecules observed by near-Field scanning optical microscopy. *Science* **1993**, *262*, 1422-1425.
(174) Meixner, A. J.; Kneppe, H. Scanning near-Field optical microscopy in cell biology and microbiology. *Cell. Mol. Biol.* **1998**, *44*, 673-688.
(175) Segers-Nolten, G. M. J.; Wyman, C.; Wijgers, N.; Vermeulen, W.; Lenferink, A. T. M.; Hoeijmakers, J. H. J.; Greve, J.; Otto, C. Scanning confocal fluorescence microscopy for single molecule analysis of nucleotide excision repair complexes. *Nucleic Acids Res.* **2002**, *30*, 4720-4727.
(176) Moerner, W. E.; Fromm, D. P. Methods of single-molecule fluorescence spectroscopy and microscopy. *Rev. Sci. Instrum.***2003**, *74*, 3597-3619.
(177) Chaudhery, V.; George, S.; Lu, M.; Pokhriyal, A.; Cunningham, B. T. Nanostructured Surfaces and Detection Instrumentation for Photonic Crystal Enhanced Fluorescence. *Sensors* **2013**, *13*, 5561-5584.
(178) Wei, Q.; Acuna, G.; Kim, S.; Vietz, C.; Tseng, D.; Chae, J.; Shir, D.; Luo, W.; Tinnefeld, P.; Ozcan, A. Plasmonics Enhanced Smartphone Fluorescence Microscopy. *Sci. Rep.* **2017**, 7, 1-10.
(179) Sheppard C. J. R.; Shotton, D. M. Confocal Laser Scanning Microscopy, Oxford, United Kingdom: BIOS Scientific Publishers, **1997**.
(180) Hibbs, Confocal A. R. Microscopy for Biologists, New York: Kluwer Academic, **2004**.
(181) Claxton, N. S.; Fellers, T. J.; Davidson, M. W. Microscopy, Confocal. Encyclopedia of Medical Devices and Instrumentation. **2006.**
(182) Single-Molecule Florescence Spectroscopy and Microscopy of Biomolecular Motors. *Annu. Rev. Phys. Chem.* **2004**. *55*, 79–96.
(183) Liu, R.; Li, Y.; Liu, L. Single molecule fluorescence spectroscopy for quantitative biological applications. *Quant. Biol.* **2016**, *4*, 177–191.
(184)Kondo, T.; Chen, W. J.; Schlau-Cohen, G. S. Single-Molecule Fluorescence Spectroscopy of Photosynthetic Systems. *Chem. Rev.* **2017**, *117*, 860–898.
(185) Finger, I.; Phillips, S.; Mobley, E.; Tucker, R.; Hess, H.; A brightness of fluorescent microspheres.*Lab Chip*, **2009**, *9*, 476–478.
(186) Webb, S. E. D.; Roberts, S. K.; Needham, S. R.; Tynan, C. J.; Rolfe, D. J.; Winn, M. D.; Clarke, D. T.; Barraclough, R.; Martin-Fernandez, M. L. Single-Molecule Imaging and

Fluorescence Lifetime Imaging Microscopy Show Different Structures for High- and Low-Affinity Epidermal Growth Factor Receptors in A431 Cells. *Biophys. J.* **2008**, *94*, 803–819.
(187) Becher, W. Fluorescence lifetime imaging–techniques and applications. *J. Microsc.* **2012**, 247, 119–136.
(188) Kapusta, P.; Macháň, R.; Benda, A.; Hof, M. Fluorescence Lifetime Correlation Spectroscopy (FLCS): Concepts, Applications and Outlook. Int. *J. Mol. Sci.* **2012**, *13*, 12890-12910.
(189) Borst.; J. W.; A. J. W. G. Visser, Fluorescence lifetime imaging microscopy in life sciences *Meas. Sci. Technol.* **2010**, 21, 1-21.
(190) Okkelman, I. A.; Dmitriev, R. I.; Foley, T.; Papkovsky, D. B Use of Fluorescence Lifetime Imaging Microscopy (FLIM) as a Timer of Cell Cycle S Phase. *PLoS ONE* **2016**, *11*, 1-18.
(191) Claudiu C. Gradinaru, Denys O. Marushchak, Masood Samim, Ulrich J. Krull Fluorescence anisotropy: from single molecules to live cells. *Analyst* **2010**, *135*, 452–459.
(192) Zhang, D.; Lu, M.; Wang, H. Fluorescence Anisotropy Analysis for Mapping Aptamer–Protein Interaction at the Single Nucleotide Level. *J. Am. Chem. Soc.* **2011**, *133*, 9188–9191.
(193) Confocal fluorescence spectroscopy and anisotropy imaging system. *Opt. Lett.* **2003**, *28*, 695-697.
(194) Suzuki, Y.; Tani, T.; Sutoh, K.; Kamimura, S. Imaging of the Fluorescence spectrum of a single fluorescent molecule by prism-based spectroscopy. *FEBS Let.* **2002**, *512*, 235-239.
(195) P.; Liu, Z.; He, G. –L.; Hou, B.; Guan, H.; Lin, Z.; Huang, The Diagnostics of Laser Induced Fluorescence (LIF) Spectra of PAHs in Flame with TD-DFT : Special Focus on 5-Membered Ring. *J. Phys. Chem.A* **2015**, 119, 13009–13017.
(196) Shahzad, A.; Koehler, G. Fluorescence spectroscopy: An emerging excellent diagnostic tool in Medical Sciences. *Int. J. Med. Tech.* **2005**, *5*, 1-4.
(197) Laser-induced fluorescence: Progress and prospective for in vivo cancer diagnosis. *Chin. Sci. Bull.* **2013**, *58*, 2003-2016.
(198) Götz, S. Recent developments in optical detection methods for microchip separations. *Anal. Bioanal. Chem*. **2007**, *387*, 183–192
(199) Vrábel, P.; Táborský, P.; Ryvolová, M.; Havel. J.; Preisler, J. Sensitive detection and separation of fluorescent derivatives using capillary electrophoresis with laser-induced fluorescence detection with 532 nm Nd:YAG laser. *Luminescence* **2006**, *118*, 283–292.
(200) Krämer, B.; Koberling, F. Fluorescence Lifetime Imaging (FLIM) based analysis of lipid organization in hepatocytes using the MicroTime 200, 2005 PicoQuant GmbH, http://www.picoquant.com.
(201) Berner, M.; Hilbig, U.; Schubert, M. B.; Gauglitz, G. Laser-induced fluorescence detection platform for point-of-care testing. *Meas. Sci. Technol.* **2017**, at press: https://doi.org/10.1088/1361-6501/aa7810.
(202) Eleni Drakaki, Clio Dessinioti, Alexander J. Stratigos, Carmen Salavastru, Christina Antoniou, Laser-induced fluorescence made simple: implications for the diagnosis and follow-up monitoring of basal cell carcinoma. *J. Biomed. Opt.* **2014**, *19*, 030901-6.
(203) C. D.; Geddes, J. R. Lakowicz1,Metal-Enhanced Fluorescence. *J. Fluoresc.* **2002**, *12*, 121-129.
(204) Strickler, S. J.; Berg, R. A. Relationship between Absorption Intensity and Fluorescence Lifetime of Molecules. *J. Chem. Phys.* 1**962**, *37*, 814-822.
(205) J.; Dong, Z.; Zhang, H.; Zheng, M.; Sun, Recent Progress on Plasmon-Enhanced Fluorescence. Nanophotonics **2015**; *4*:472–490.
(206) Bauch, M.; Toma, K.; Toma, M. Plasmon-Enhanced Fluorescence Biosensors: a Review. Plasmonics **2014**, 9, 781–799.

(207) Flynn, J. D.; Haas, B. L.; Biteen, J. S. Plasmon-Enhanced Fluorescence from Single Proteins in Living Bacteria.*J. Phys. Chem. C* **2016**, *120*, 20512–20517.
(208) Donehue, J. E.; Wertz, E.; Talicska, C. N.; Biteen, J. S. Plasmon-enhanced brightness and photostability from single fluorescent proteins coupled to gold nanorods. *J. Phys. Chem. C* **2014***,118,* 15027-15035.
(209) Bouccara, S.; Sitbon, G.; Fragola, A.; Loriette, V.; Lequeux, N.; Pons, T. Enhancing Fluorescence in vivo imaging using inorganic nanoprobes. Current Opinion in Biotechnology, Elsevier, **2015**, *34*, 65-72. .
(210) Anger, P.; Bharadwaj, P.; Novotny, L. Enhancement and quenching of single-molecule fluorescence. *Phys. Rev. Lett.* **2006***, 96,* 1130021-1130024.
(211) Aslan, K.; Lakowicz, J. R.; Szmacinski, H.; Geddes, C. D. Metal-Enhanced Fluorescence Solution-Based Sensing Platform. *J. Fluoresc.* **2004**, 677-679.
(212)Jiang, Y.; Wang, H. –Y.; Wang, H.; Gao, B. –R.; Hao, Y. –W.; Jin, Y.; Chen, Q. –D.; Sun, H. –B. Surface Plasmon Enhanced Fluorescence of Dye Molecules on Metal Grating Films. *J. Phys. Chem. C* **2011**, *115*, 12636–12642.
(213)Riedel, T.; Hageneder, S.; Surman, F.; Pop-Georgievski, O.; Noehammer, C.; Hofner, M.; Brynda, E.; Rodriguez-Emmenegger, C.; Dostálek, J. Plasmonic Hepatitis B Biosensor for the Analysis of Clinical Saliva. *Anal. Chem.* **2017**, *89*, 2972−2977.
(214) Wang, L.; Song, Q.; Liu, Q.; He, D.; Ouyang, J. Plasmon-Enhanced Fluorescence-Based Core–Shell Gold Nanorods as a Near-IR Fluorescent Turn-On Sensor for the Highly Sensitive Detection of Pyrophosphate in Aqueous Solution. *Adv. Funct. Mater.* **2015**, *25*, 7017–7027.
(215) Park, J. –E.; Kim, J.; Nam, J. –M. Emerging plasmonic nanostructures for controlling and enhancing photoluminescence. *Chem. Sci.* **2017**, *8*, 4696–4704.
(216) Galloway, C. M.; Artur, C.; Grand, J.; Le, E. C. Ru Photobleaching of Fluorophores on the Surface of Nanoantennas. *J. Phys. Chem. C* **2014**, *118*, 28820−28830.
(217) Li, J. -F.; Li, C. –Y.; Aroca, R. F. Plasmon-enhanced fluorescence spectroscopy. *Chem. Soc. Rev.* **2017**, *46*, 3962-3979.
(218) Cheng, Y.; Stakenborg, T.; Dorpe, P. V.; Lagae, L.; Wang, M.; Chen, H.; Borghs, G. Fluorescence near gold nanoparticles for DNA sensing. *Anal. Chem.* **2011**, *83*, 1307–1314.
(219) Abadeer, N. S.; Brennan, M. R.; Wilson, W. L.; Murphy, C. J. Distance and plasmon wavelength dependent fluorescence of molecules bound to silica-coated gold nanorods. *A.C.S. nano* **2014**, *8*, 8392–8406.
(220) Deng, W.; Goldys, E. M. Plasmonic Approach to Enhanced Fluorescence for Applications in Biotechnology and the Life Sciences. *Langmuir* **2012**, *28*, 10152-10163.
(221) Vukovic, S.; Corni, S.; Mennucci, B. Fluorescence enhancement of chromophores close to metal nanoparticles. Optimal setup revealed by the polarizable continuum model. *J. Phys. Chem. C* **2009**, *113*, 121–33.
(222) Yuan, H., Khatua, S., Zijlstra, P., Yorulmaz, M. & Orrit, M. Thousand-fold enhancement of single-molecule fluorescence near a single gold nanorod. *Angew. Chem. Int. Ed.* **2013**, *52*, 1217–21.
(224) Li, H.; Chen, C. –Y.; Wei, X.; Qiang, W.; Li, Z.; Cheng, Q.; Xu, D. Highly sensitive detection of proteins based on metal-enhanced fluorescence with novel silver nanostructures. *Anal. Chem.* **2012**, *84*, 8656–8262.
(225) Darvill, D.; Centeno, A.; Xie, F. Plasmonic fluorescence enhancement by metal nanostructures: shaping the future of bionanotechnology. *Phys. Chem. Chem. Phys.* **2013,** *15*, 15709–15726.
(226) Khatua, S.; Paulo, P. M. R.; Yuan, H.; Gupta, A.; Orrit, M.; Zijlstra, P. Resonant Plasmonic Enhancement of Single-Molecule Fluorescence by Individual Gold Nanorods. *ACS Nano*, **2014**, *8*, 4440–4449.

(227) Yorulmaz, M.; Khatua, S.; Zijlstra, P.; Gaiduk, A.; Orrit, M. *Nano Lett.* **2012**, *12*, 4385−4391.
(228) Rao, W.; Li, Q.; Wang, Y.; Li, T.; Wu, L. *ACS Nano* 2015, 9, 2783−2791.
(229) Wu, X.; Ming, T.; Wang, X.; Wang, P.; Wang, J.; Chen, J. *A.C.S. Nano* **2010**, *4*, 113−120.
(230) Bardhan, R.; Grady, N. K.; Halas, N. J. Nanoscale Control of Near-Infrared Fluorescence Enhancement Using Au Nanoshells. *Small* **2008**, *4*, 1716–1722.
(231) Bardhan, R.; Grady, N. K.; Cole, J. R.; Joshi, A.; Halas, N. J. Fluorescence enhancement by Au nanostructures: nanoshells and nanorods. *ACS Nano***2009**, *3*, 744−752.
(232) Reineck, P.; Gómez, D.; Ng, S. H.; Karg, M.; Bell, T.; Mulvaney, P.; Bach. U. Distance and wavelength dependent quenching of molecular fluorescence by Au@SiO2 core-shell nanoparticles. *ACS nano* **2013***, 7*, 6636–6648.
(233) Lin, H. -H.; Chen, I. -C. Study of the interaction between gold nanoparticles and rose bengal fluorophores with silica spacers by time-resolved fluorescence spectroscopy. *J. Phys. Chem. C* **2015,** *119*, 26663–26671.
(234) Chen, J.; Jin, Y.; Fahruddin, N.; Zhao, J. X. Development of gold nanoparticle-enhanced fluorescent nanocomposites. *Langmuir* **2013**, *29*, 1584–1591.
(235) Abadeer, N. S.; Brennan, M. R.; Wilson, W. L.; Murphy, C. J. Distance and plasmon wavelength dependent fluorescence of molecules bound to silica-coated gold nanorods. *ACS nano* **2014**, *8*, 8392–8406.
(237) Guerrero-Martinez, A.; Perez-Juste, J.; Liz-Marzan, L. M. Recent progress on silica coating of nanoparticles and related nanomaterials. *Adv. Mater.* **2010**, *22*, 1182–1195.
(238) Ribeiro, T.; Baleizão, C.; Farinha, J. P. S. Artefact-free Evaluation of Metal Enhanced Fluorescence in Silica Coated Gold Nanoparticles. *Sci. Rep.* **2017**, *7*, 1-12.
(239) Muskens, O. L.; Giannini, V.; Sanchez-Gil, J. A.; Rivas, J. G. Strong Enhancement of the Radiative Decay Rate of Emitters by Single Plasmonic Nanoantennas. *Nano Lett.***2007**, *7*, 2871–2875.
(240) Zhao, T.; Yu, K.; Li, L.; Zhang, T.; Guan, Z.; Gao, N.; Yuan, P.; Li, S.; Yao, S. Q.; Xu, Q. –H.; Xu, G. Q. Gold Nanorod Enhanced Two-Photon Excitation Fluorescence of Photosensitizers for Two-Photon Imaging and Photodynamic *.ACS Appl. Mater. Interfaces* **2014**, *6*, 2700–2708. Therapy
(241) Ayala-Orozco, C.; Liu, J. G.; Knight, M. W.; Wang, Y.; Day, J. K.; Nordlander, P.; Halas, N. J. Fluorescence Enhancement of Molecules inside a Gold Nanomatryoshka. *Nano Lett.* **2014**, *14*, 2926−2933.
(242) Cheng, Y.; Stakenborg, T.; Dorpe, P. V.; Lagae, L.; Wang, M.; Chen, H.; Borghs, G. Fluorescence near gold nanoparticles for DNA sensing. *Anal. Chem.* **2011**, *83*, 1307–1314.
(243) Chatterjee, S.; Lee, J. B.; Valappil, N. V.; Luo, D.; Menon, V. M. Investigating the distance limit of a metal nanoparticle based spectroscopic ruler. *Biomed. Opt. Express* **2011**, *2*, 1727–1733.
(244) Ribeiro, T.; Prazeres, T. J. V.; Moffitt, M.; Farinha, J. P. S. Enhanced photoluminescence from micellar assemblies of cadmium sulfide quantum dots and gold nanoparticles. *J. Phys. Chem. C* **2013,** *117*, 3122–3133.
(245) Zhang, J.; Ma, N.; Tang, F.; Cui, Q.; He, F.; Li, L. pH- and glucose-responsive core-shell hybrid nanoparticles with controllable metal-enhanced fluorescence effects. *ACS Appl. Mater. Int.* **2012**, *4*, 1747–1751.
(246) Tang, F.; Ma, N.; Tong, L.; He, F.; Li, L. Control of metal-enhanced fluorescence with pH- and thermoresponsive hybrid microgels. *Langmuir* **2012**, *28*, 883–888.
(247) Zhang, B.; Kumar, R. B.; Dai, H.; Feldman, B. J. A plasmonic chip for biomarker discovery and diagnosis of type 1 diabetes. *Nat. Med.* **2014,** *20*, 948-53.

(248). Paulo, P. M. R.; Zijlstra, P.; Orrit, M.; G.-Fernandez, E.; Pace, T. C. S. Viana, A. S.; Costa, S. M. B. Tip-Specific Functionalization of Gold Nanorods for Plasmonic Biosensing: Effect of Linker Chain Length. *Langmuir* **2017**, *33*, 6503−6510.
(249) Mita, H.; Ohyama, T.; Tanaka, Y.; Yamamoto, Y. "Formation of a Complex of 5,10,15,20-Tetrakis(N-methylpyridinium-4-yl)-21H,23H-porphyrin with G-Quadruplex DNA, *Biochemistry* **2006** *45*, 6765-6772.
(250) Francisco, A. P. **2017**, "Intensificação Plasmónica de Fluorescência de Cromóforos Bio-inspirados" (Master's thesis). Faculdade de Ciências e Tecnologia da Universidade Nova de Lisboa).The value obtained for TMPyP in PBS buffer is 0.0008 count/ms/molecule.

(251) Goncalvesa, P. J.; Franzenb, P. L.; Correac, D. S.; Almeidad, L.M.; Takarae, M.; Itoe, A. S.; Zíliob, S. C.; Borissevitch I. E. Effects of environment on the photophysical characteristics of meso tetrakis methylpyridiniumyl porphyrin (TMPyP). *Spectrochim. Acta A* **2011**, *79*, 1532–1539.

(252) Paulo, P. M. R. private communication, **2017**, Instituto Superior Técnico da Universidade de Lisboa.

(253) Paulo, P. M. R. **2005**, "Processos Fotoinduzidos em Sistemas Não-Covalentes Iónicos Porfirina-Dendrímero: Interacções Excitónicas e Transferência Electrónica" (PhD thesis). Instituto Superior Técnico da Universidade de Lisboa.

(254) Francisco, A. P. **2017**, "Intensificação Plasmónica de Fluorescência de Cromóforos Bio-inspirados" (Master's thesis). Faculdade de Ciências e Tecnologia da Universidade Nova de Lisboa.

Annex A

1. Sensing of Streptavidin with Biotin-functionalized Gold Nanorods

1.1 Gold Nanorods functionalized with a PEG-4 linker concentration of 1 μM

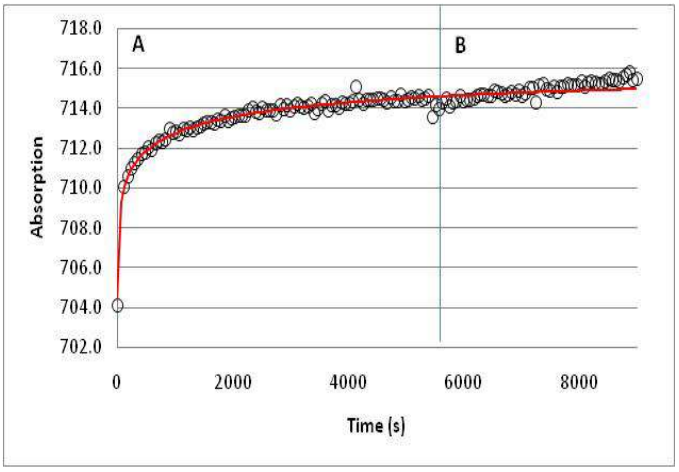

Figure A.1 A) Binding kinetic curve of biotin-functionalized gold nanorods (30nm x 10nm) with PEG-4 linker (1 μm) with streptavidin target solution 100 nM (black curve) and fitted kinetic model (red curve). B) Binding kinetic curve of the same sample with streptavidin solution 1000 nM (black curve).

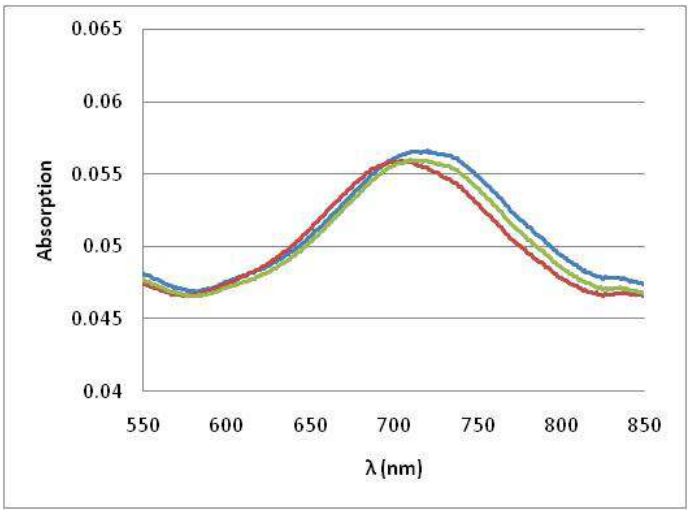

Figure A.2 Absorption spectra of biotin-functionalized gold nanorods (30nm x 10nm) with PEG-4 linker (1 μm) in PBS before binding assay (red curve); the same sample after binding assay with streptavidin solution 100 nM (green curve); and after binding assay with streptavidin solution 1000 nM (blue curve).

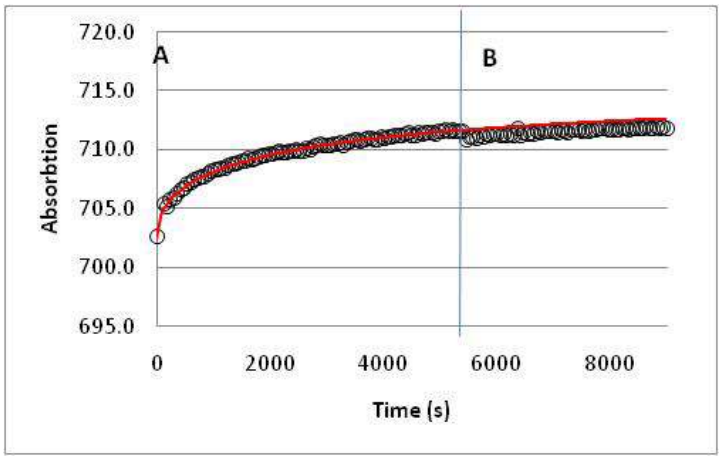

Figure A.3 A) Binding kinetic curve of biotin-functionalized gold nanorods (30nm x 10nm) with PEG-4 linker (1 µm) with streptavidin target solution 100 nM (black curve) and the fitted kinetic model (red curve). B) Binding kinetic curve of same sample with streptavidin solution 1000 nM (black curve).

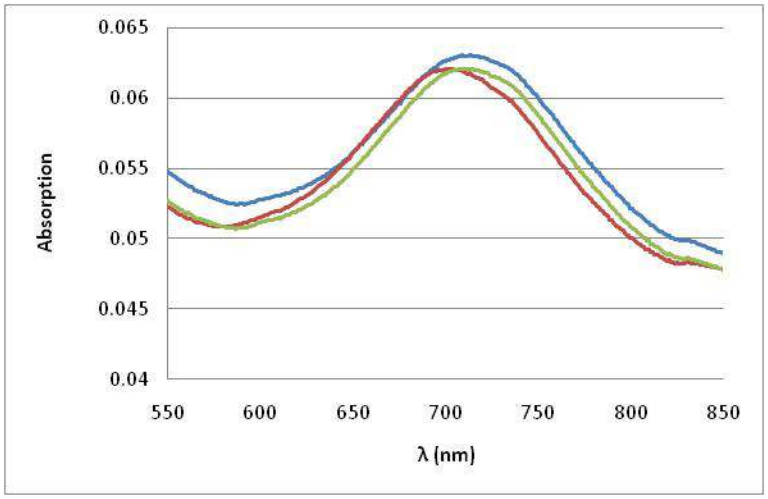

Figure A.4 Absorption spectra of biotin-functionalized gold nanorods (30nm x 10nm) with PEG-4 linker (1 µm) in PBS before binding assay (red curve); the same sample after binding assay with streptavidin solution 100 nM (green curve); and after binding assay with streptavidin solution 1000 nM (blue curve).

1.2 Gold Nanorods functionalized with a PEG-4 linker concentration of 10 µM

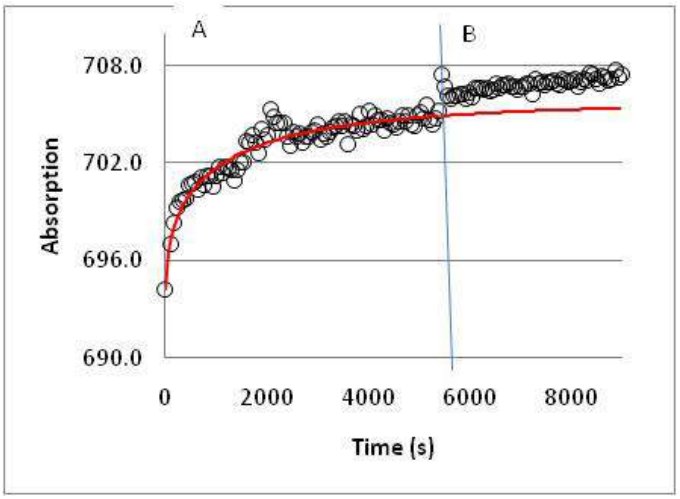

Figure A.5 A) Binding kinetic curve of biotin-functionalized gold nanorods (30nm x 10nm) with PEG-4 linker (10 µm) with streptavidin target solution 100 nM (black curve) and the fitted kinetic model (red curve); B) Binding kinetic curve of same sample with streptavidin solution 1000 nM (black curve).

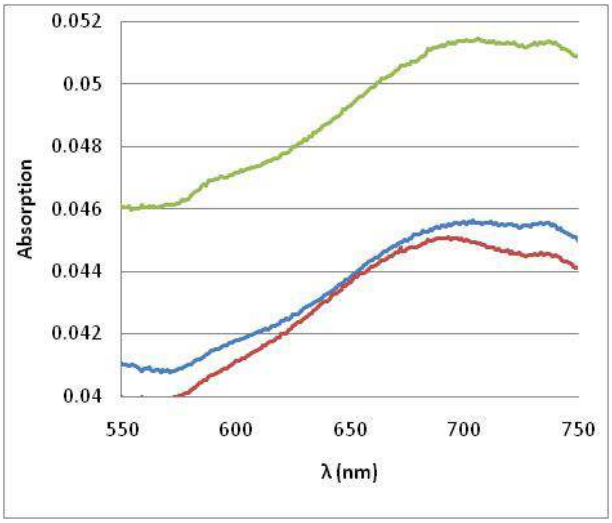

Figure A.6 Absorption spectra of biotin-functionalized gold nanorods (30nm x 10nm) with PEG-4 linker (10 µm) in PBS before binding assay (red curve); the same sample after binding assay with streptavidin solution 100 nM (green curve); and after binding assay with streptavidin solution 1000 nM (blue curve).

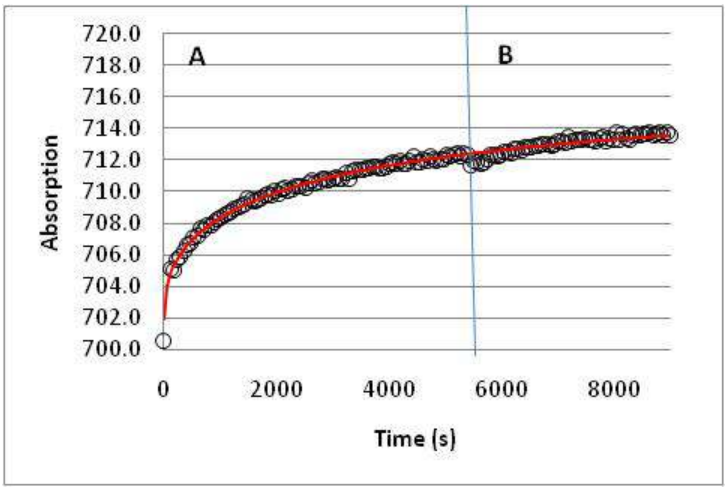

Figure A.7 A) Binding kinetic curve of biotin-functionalized gold nanorods (30nm x 10nm) with PEG-4 linker (10 µm) with streptavidin target solution 100 nM (black curve) and fitted kinetic model (red curve); B) Binding kinetic curve of same sample with streptavidin solution 1000 nM (black curve).

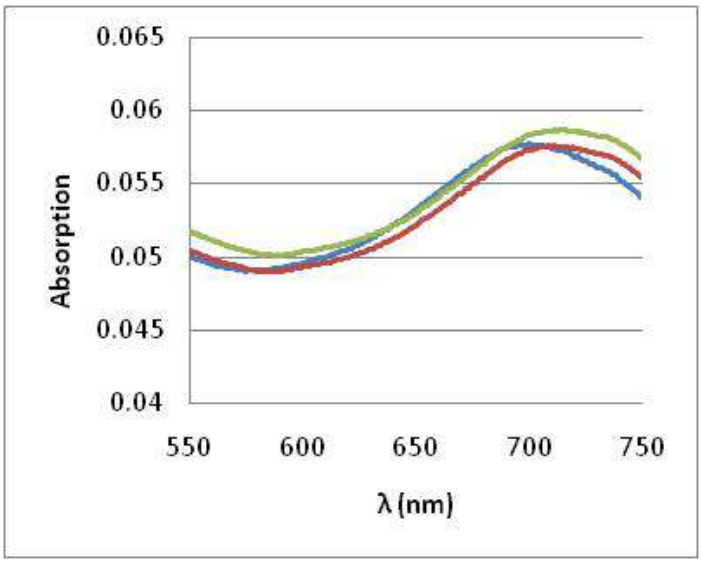

Figure A.8 Absorption spectra of biotin-functionalized gold nanorods (30nm x 10nm) with PEG-4 linker (10 µm) in PBS before binding assay with streptavidin (red curve); the same sample after binding assay with streptavidin solution 100 nM (green curve); and after binding assay with streptavidin solution 1000 nM (blue curve).

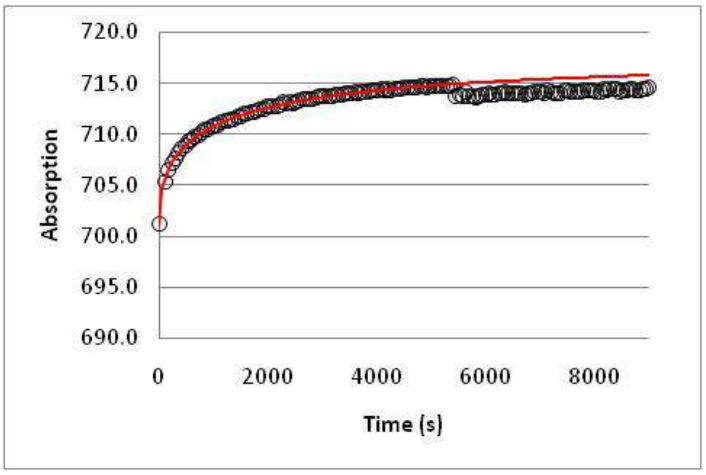

Figure A.9 A) Binding kinetic curve of biotin-functionalized gold nanorods (30nm x 10nm) with PEG-4 linker (10 µm) with streptavidin target solution 100 nM (black curve) and the fitted kinetic model (red curve); B) Binding kinetic curve of same sample with streptavidin solution 1000 nM (black curve).

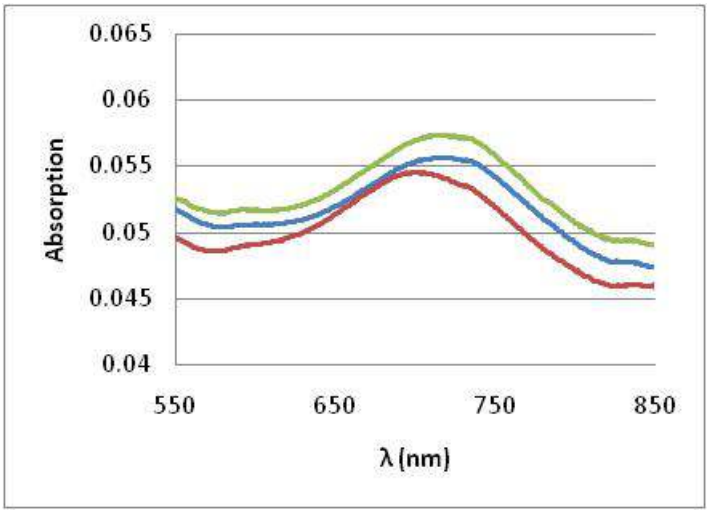

Figure A.10 Absorption spectra of biotin-functionalized gold nanorods (30nm x 10nm) with PEG-4 linker (10 µm) in PBS before binding assay with streptavidin (red curve); the same sample after binding assay with streptavidin solution 100 nM (green curve); and after binding assay with streptavidin solution 1000 nM (blue curve).

1.3 Gold Nanorods functionalized with a PEG-4 linker concentration of 100µM

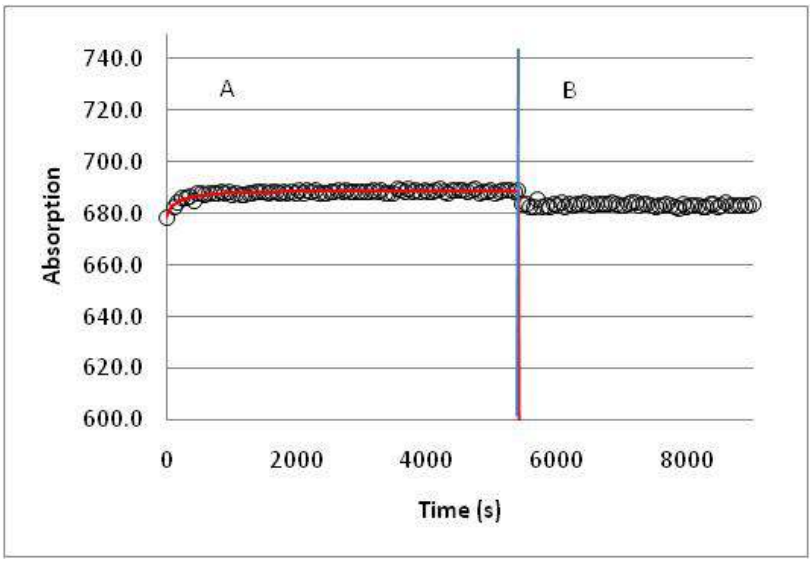

Figure A.11 A) Binding kinetic curve of biotin-functionalized gold nanorods (30nm x 10nm) with PEG-4 linker (100 µm) with streptavidin target solution 100 nM (black curve) and the fitted kinetic model (red curve); B) Binding kinetic curve of same sample with streptavidin solution 1000 nM (black curve).

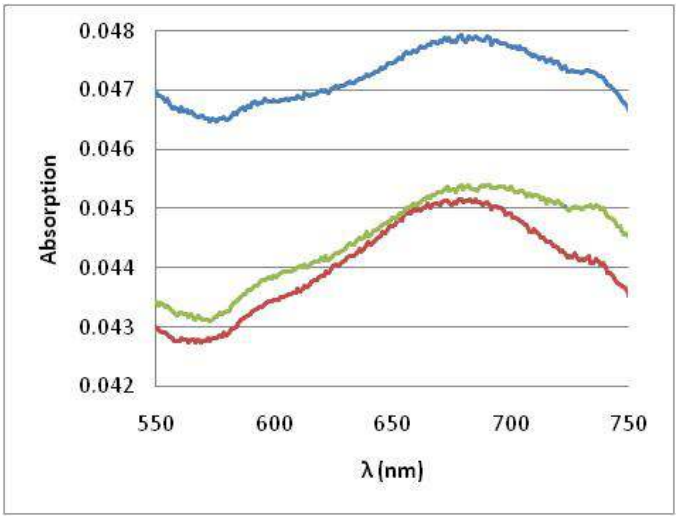

Figure A.12 Absorption spectra of biotin-functionalized gold nanorods (30nm x 10nm) with PEG-4 linker (100 µm) in PBS before binding assay with streptavidin (red curve); the same sample after binding assay with streptavidin solution 100 nM (green curve); and after binding assay with streptavidin solution 1000 nM (blue curve).

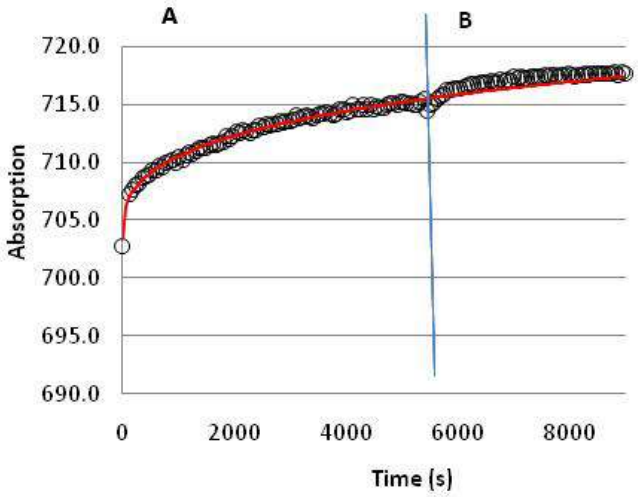

Figure A.13 A) Binding kinetic curve of biotin-functionalized gold nanorods (30nm x 10nm) with PEG-4 linker (100 µm) with streptavidin target solution 100 nM (black curve) and fitted kinetic model (red curve); B) Binding kinetic curve of same sample with streptavidin solution 1000 nM (black curve).

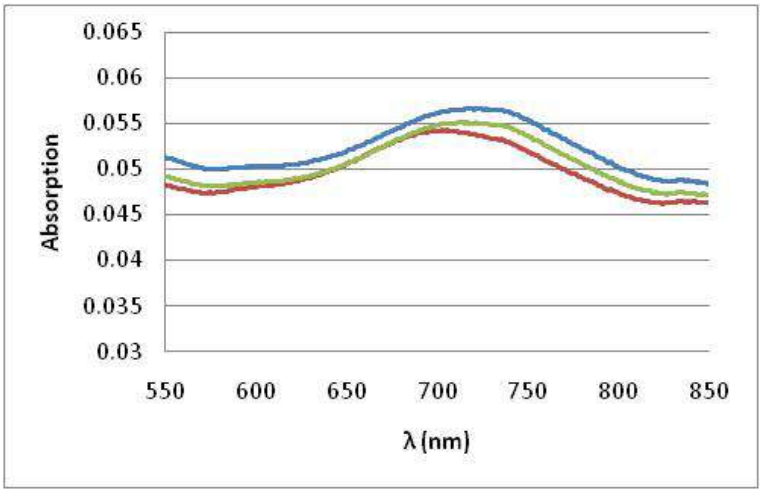

Figure A.14 Absorption spectra of biotin-functionalized gold nanorods (30nm x 10nm) with PEG-4 linker (100 µm) in PBS before binding assay with streptavidin (red curve); the same sample after binding assay with streptavidin solution 100 nM (green curve); and after binding assay with streptavidin solution 1000 nM (blue curve).

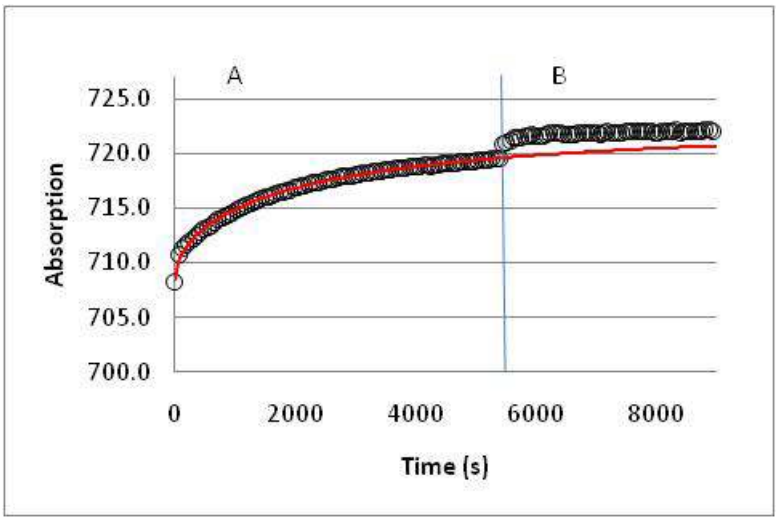

Figure A.15 A) Binding kinetic curve of biotin-functionalized gold nanorods (30nm x 10nm) with PEG-4 linker (100 µm) with streptavidin target solution 100 nM (black curve) and fitted kinetic model (red curve); B) Binding kinetic curve of same sample with streptavidin solution 1000 nM (black curve).

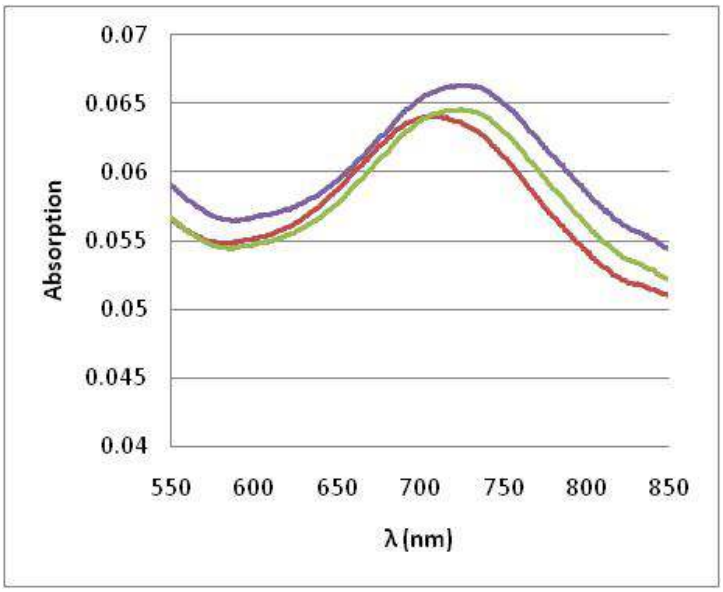

Figure A.16 Binding kinetic curve of biotin-functionalized gold nanorods (30nm x 10nm) with PEG-4 linker (100 µm) with streptavidin target solution 100 nM (black curve) and the binding kinetic calculated model curve (red color); Binding kinetic curve of same sample with streptavidin solution 1000 nM (black curve); and the binding kinetic calculated model curve (red color).

Annex B

1. Ss-Dengue DNA functionalized single gold nanorods-TMPyP

1.1 The LSPR and FWHM of the glass immobilized gold nanoparticles excited at laser wavelength of 480 nm in H_2O (Table B.1), PBS (Table B.2) and after functionalization with ss-Dengue Virus DNA solution (100 nM) (Table B.3)

Table B.1

Data file:	WL_max (nm)	FWHM	WL_max (meV)	FWHM
1	664.7	41.9	1.87	117.5
2	670.9	40.2	1.85	110.6
3	650.0	40.7	1.91	119.4
4	671.6	39.2	1.85	107.7
5	651.6	38.5	1.90	112.3
6	626.5	41.8	1.98	131.9
7	658.4	42.4	1.88	121.2
8	627.4	34.6	1.98	108.8
9	679.8	33.6	1.82	90.0
10	633.8	38.0	1.96	117.3
11	665.0	38.7	1.86	108.4
12	628.8	34.4	1.97	107.9
13	640.6	39.5	1.94	119.3
14	662.5	40.2	1.87	113.6
15	682.0	34.6	1.82	92.1
16	643.6	43.9	1.93	131.1
17	639.3	39.3	1.94	119.2
18	673.3	42.9	1.84	117.3
19	667.2	43.7	1.86	121.5
20	656.4	42.4	1.89	121.8
	averages		SD	
WL_max	654.7	+/-	17.7	
FWHM	114.4	+/-	10.5	

Table B.2

Data file	WL_max (nm)	FWHM	WL_max (meV)	FWHM	ΔWL_max (PBS-H2O)
1	666.2	43.0	1.86	120.0	1.5
2	672.9	43.6	1.84	119.2	2.1
3	649.8	43.0	1.91	126.1	-0.2
4	672.0	42.7	1.85	117.1	0.4
5	652.7	41.5	1.90	120.7	1.2
6	629.8	41.1	1.97	128.2	3.3
7	660.8	43.7	1.88	123.9	2.5
8	630.7	36.2	1.97	112.6	3.3
9	677.6	41.9	1.83	113.1	-2.2
10	634.9	41.5	1.95	127.5	1.1
11	666.4	42.2	1.86	117.8	1.4
12	630.1	38.4	1.97	119.8	1.3
13	641.4	41.2	1.93	124.2	0.8
14	663.1	43.6	1.87	122.8	0.6
15	681.3	40.9	1.82	109.0	-0.6
16	643.9	48.6	1.93	145.1	0.2
17	639.0	38.9	1.94	118.1	-0.3
18	674.6	42.6	1.84	115.9	1.3
19	668.4	43.1	1.85	119.6	1.2
20	654.7	40.2	1.89	116.2	-1.7
	averages		**SD**		**averages**
WL_max	**655.5**	+/-	**17.1**		**0.9**
FWHM	**120.8**	+/-	**7.6**		**1.4**

Table B.3

Data file:	WL_max (nm)	FWHM	WL_max (meV)	FWHM	ΔWL_max (ss_Denv2-PBS)
1	663.9	40.1	1.87	112.7	-2.3
2	669.6	39.2	1.85	108.4	-3.4
3	649.3	39.0	1.91	114.6	-0.4
4	669.4	38.0	1.85	104.9	-2.6
5	649.8	33.9	1.91	99.5	-3.0
6	627.4	36.9	1.98	116.1	-2.5
7	658.4	35.6	1.88	101.7	-2.4
8	628.9	33.0	1.97	103.3	-1.8
9	677.5	34.7	1.83	93.8	-0.1
10	633.1	34.2	1.96	105.6	-1.8
11	663.7	36.7	1.87	103.3	-2.7
12	628.2	32.1	1.97	100.9	-1.9
13	640.0	36.3	1.94	109.9	-1.4
14	660.6	34.9	1.88	99.1	-2.5
15	679.9	33.6	1.82	90.1	-1.4
16	643.3	39.1	1.93	117.2	-0.6
17	638.4	33.2	1.94	101.0	-0.5
18	673.2	39.4	1.84	107.7	-1.4
19	664.3	34.8	1.87	97.8	-4.1
20	654.4	32.5	1.89	93.9	-0.2
	averages		**SD**		**averages**
WL_max	**653.7**	**+/-**	**17.0**		**-1.9**
FWHM	**104.1**	**+/-**	**7.6**		**1.1**

1.2 Top Fluorescence Enhancement Factor and Fluorescence Enhanced Figure of Merit of ss-Dengue Virus DNA functionalized single GNRs in TMPyP solution and their Plasmonic resonance wavelength have shown in Table B.4

Tabel B.4

Particles No.	size_max_burst (max.counts)-(Average+2*sigma)	Top Enhanc. Factor (Siz.max.burst)/(A)	Fluor. Enhanc. Figure of Merit (Top Enhancement Factor)/(B)	λ max
1	76.9	96125	4806.25	663.9
2	79.1	98875	4943.75	669.6
3	61	76250	3812.5	649.3
4	60.8	76000	3800	669.4
5	23	28750	1437.5	649.8
6	36.6	45750	2287.5	627.4
7	83.1	103875	5193.75	658.4
8	39.9	49875	2493.75	628.9
10	17.3	21625	1081.25	633.1
11	80.8	101000	5050	663.7
12	25.2	31500	1575	628.2
13	39.8	49750	2487.5	640.0
14	27.3	34125	1706.25	660.6
16	77.9	97375	4868.75	643.3
17	44.5	55625	2781.25	638.4
18	34.8	43500	2175	673.2
19	16.1	20125	1006.25	664.3
	Average of Top Enhancement	**6.06E+04**	**3.03E+03**	
	STDEV	**2.93E+04**	**1.46E+03**	

1.3 Photluminescence Intensity single GNRs at laser excitation wavelength 480 nm and 640 nm (Table B.5)

Table B.5

Particles No.	Top Enhanc. Factor (Siz.max.burst)/(A)	λ max	Photoluminesence Inensity λ Excitation =480 nm	Photoluminesence Inensity λ Excitation =640nm
1	96125	663.9	108	93
2	98875	669.6	100	67.5
3	76250	649.3	104	73
4	76000	669.4	70	88
5	28750	649.8	105	38
6	45750	627.4	122	26
7	103875	658.4	114	70
8	49875	628.9	72.5	24.5
10	21625	633.1	88	13
11	101000	663.7	80	94
12	31500	628.2	72.5	16.5
13	49750	640.0	85.5	52
14	34125	660.6	76	24.5
16	97375	643.3	107	62
17	55625	638.4	88	45
18	43500	673.2	84	57
19	20125	664.3	63	24
	6.06E+04	**Average**	**90.6**	**51.1**
	2.93E+04	**STDEV**	**16.9**	**26.4**

2 Ds-Dengue Virus DNA functionalized single gold nanorods

2.1 The LSPR and FWHM of the glass immobilized gold nanoparticles excited at laser wavelength of 480 nm in H_2O (Table B.6), PBS (Table B.7) and after functionalization with ds-Dengue Virus DNA solution (100 nM) (Table B.8)

B.6

Data file	WL_max (nm)	FWHM	WL_max (meV)	FWHM
1	656.3	38.8	1.89	111.6
2	658.6	42.5	1.88	121.4
3	652.7	40.0	1.90	116.4
4	659.4	40.5	1.88	115.4
5	632.6	37.5	1.96	116.2
6	626.7	37.1	1.98	117.0
7	644.1	37.2	1.92	111.1
8	651.4	39.1	1.90	114.1
9	645.3	39.1	1.92	116.4
10	617.9	38.1	2.01	123.6
11	645.8	38.3	1.92	113.8
12	658.4	40.3	1.88	115.2
13	662.0	38.9	1.87	109.9
14	649.0	38.5	1.91	113.3
15	643.2	39.6	1.93	118.5
16	652.2	40.9	1.90	119.1
17	632.0	41.7	1.96	129.4
18	651.2	42.0	1.90	122.7
19	674.6	40.4	1.84	109.9
20	657.6	42.4	1.89	121.5
	averages		SD	
WL_max	648.6	+/-	13.3	
FWHM	116.8	+/-	5.0	

B.7

Data file	WL_max (nm)	FWHM	WL_max (meV)	FWHM	ΔWL_max (PBS-H2O)
1	659.0	38.5	1.88	109.9	2.7
2	660.7	41.1	1.88	116.7	2.1
3	655.7	39.5	1.89	113.8	3.0
4	662.8	40.6	1.87	114.4	3.4
5	634.5	37.3	1.95	114.9	1.8
6	628.8	36.7	1.97	115.0	2.0
7	645.8	35.8	1.92	106.5	1.6
8	653.1	38.4	1.90	111.6	1.8
9	647.3	38.6	1.92	114.1	2.0
10	620.5	36.5	2.00	117.5	2.6
11	648.0	36.9	1.91	108.8	2.1
12	658.4	40.3	1.88	115.2	0.0
13	661.5	38.7	1.87	109.6	-0.5
14	651.1	37.4	1.90	109.2	2.1
15	645.0	38.7	1.92	115.2	1.8
16	654.3	40.8	1.89	118.1	2.1
17	634.1	39.9	1.96	122.9	2.1
18	652.5	40.9	1.90	118.9	1.3
19	677.9	38.9	1.83	104.8	3.2
20	661.4	40.1	1.87	113.5	3.8
	averages		SD		averages
WL_max	650.6	+/-	13.4		2.1
FWHM	113.5	+/-	4.4		1.0

B8.

Data file:	WL_max (nm)	FWHM	WL_max (meV)	FWHM	ΔWL_max (ds_Denv2-PBS)
1	658.2	36.8	1.88	105.2	-0.7
2	659.2	38.2	1.88	108.9	-1.6
3	656.6	38.5	1.89	110.6	0.9
4	663.3	38.5	1.87	108.4	0.4
5	633.8	35.7	1.96	110.2	-0.6
6	628.5	35.5	1.97	111.3	-0.3
7	647.0	34.4	1.92	101.8	1.2
8	651.7	37.2	1.90	108.6	-1.4
9	645.8	37.5	1.92	111.4	-1.5
10	620.2	35.4	2.00	114.0	-0.3
11	648.9	36.0	1.91	106.0	1.0
12	662.4	36.7	1.87	103.7	4.0
13	667.0	36.2	1.86	100.9	5.4
14	650.8	34.2	1.91	99.9	-0.3
15	644.9	36.9	1.92	110.0	-0.1
16	653.4	37.2	1.90	107.8	-0.9
17	634.3	40.0	1.95	123.2	0.1
18	650.8	37.8	1.91	110.6	-1.7
19	677.0	37.9	1.83	102.5	-0.9
20	663.2	37.2	1.87	104.8	1.8
	averages		SD		averages
WL_max	650.8	+/-	13.8		0.2
FWHM	108.0	+/-	5.3		1.8

2.2 Top Fluorescence Enhancement Factor and Fluorescence Enhanced Figure of Merit of ds-Dengue Virus DNA functionalized single GNRs in TMPyP solution and their Plasmonic resonance wavelength have shown in Table B.9

B.9

Particles No.	max_counts	size_max_burst (max.counts)-(Average+2*sigma)	Top Enhanc. Factor (Siz.max.burst)/(A)	Fluor. Enhanc. Figure of Merit (Top Enhancement Factor)/(B)	λ max
1	81	48.3	60375	3018.75	658.2
2	51	9	11250	562.5	659.2
3	64	33.9	42375	2118.75	656.6
5	144	110	137500	6875	633.8
7	64	25.8	32250	1612.5	647.0
8	94	55.1	68875	3443.75	651.7
9	124	90.6	113250	5662.5	645.8
10	80	47.2	59000	2950	620.2
11	96	53.5	66875	3343.75	648.9
12	98	55.5	69375	3468.75	662.4
13	74	31.5	39375	1968.75	667.0
14	57	14.5	18125	906.25	650.8
15	78	35.7	44625	2231.25	644.9
17	75	32.7	40875	2043.75	634.3
18	62	18.2	22750	1137.5	650.8
19	100	57.7	72125	3606.25	677.0
20	152	108.4	135500	6775	663.2
		Average	**6.09E+04**	**3.04E+03**	**651.3**
		SD	**3.64E+04**	**1.82E+03**	**13.2**

2.3 Photluminescence Intensity single GNRs at laser excitation wavelength 480 nm and 640 nm (Table B.10)

B.10

Particles No.	Top Fluorescence Enhancement Factor	λ max	Photoluminescence Inensity λ Excitation =480nm	Photoluminescence Inensity λ Excitation =640nm
1	60375	658.2	104	46
2	11250	659.2	57	16
3	42375	656.6	84	62
5	137500	633.8		
7	32250	647.0	86	50
8	68875	651.7	96	69
9	113250	645.8	94	83
10	59000	620.2	85.5	
11	66875	648.9	98	52
12	69375	662.4	94	78
13	39375	667.0	107	62
14	18125	650.8	80	26
15	44625	644.9	87	37
17	40875	634.3	108	33
18	22750	650.8	100	51
19	72125	677.0	93	82
20	135500	663.2	100	63
	6.09E+04	**Avarage**	**92.1**	**54.0**
	3.64E+04	**SD**	**12.1**	**19.5**

3 Complex Ds-Dengue DNA-TMPyP functionalized single gold nanorods-TMPyP

3.1 The LSPR and FWHM of the glass immobilized gold nanoparticles excited at laser wavelength of 480 nm in H_2O (Table B.11), PBS (Table B.12) and after functionalization with Complex -ds-Dengue_2-TMPyP solution (100 nM) (Table B.13)

B.11

Data file:	WL_max (nm)	FWHM	WL_max (meV)	FWHM
1	669.6	41.3	1.85	114.0
2	661.1	38.6	1.88	109.5
3	602.9	38.0	2.06	129.6
4	653.7	37.3	1.90	108.0
5	659.6	44.1	1.88	125.5
6	637.5	52.8	1.94	160.8
7	652.6	37.9	1.90	110.3
8	616.7	37.2	2.01	121.3
9	619.6	36.2	2.00	116.8
10	644.8	39.8	1.92	118.6
11	646.7	39.7	1.92	117.6
12	635.1	39.7	1.95	121.8
13	664.6	41.8	1.87	117.1
14	667.8	36.4	1.86	101.1
15	680.4	39.6	1.82	105.9
	averages		SD	
WL_max	647.5	+/-	21.8	
FWHM	118.5	+/-	14.0	

B.12

Data file:	WL_max (nm)	FWHM	WL_max (meV)	FWHM	ΔWL_max (PBS-H2O)
1	673.2	41.8	1.84	114.2	3.6
2	664.2	38.6	1.87	108.3	3.1
3	604.7	38.9	2.05	131.8	1.8
4	655.3	37.9	1.89	109.3	1.6
5	662.0	43.0	1.87	121.4	2.4
6	642.7	49.2	1.93	147.6	5.3
7	653.0	37.4	1.90	108.7	0.4
8	619.4	38.8	2.00	125.4	2.6
9	622.8	37.7	1.99	120.5	3.2
10	647.5	36.1	1.91	106.6	2.7
11	649.1	38.1	1.91	112.1	2.4
12	636.9	36.9	1.95	112.5	1.8
13	668.3	42.9	1.86	118.8	3.8
14	666.3	36.8	1.86	102.7	-1.5
15	684.2	39.1	1.81	103.4	3.8
	avarage		SD		**avarage**
WL_max	**650.0**	+/-	**21.80**		**2.5**
FWHM	**116.2**	+/-	**11.85**		**1.5**

B.13

Data file:	WL_max (nm)	FWHM	WL_max (meV)	FWHM	ΔWL_max (Complex-ds_Denv2-TMPyP)-PBS)
1	673.6	45.0	1.84	122.9	0.4
2	662.8	39.6	1.87	111.6	-1.4
3	604.4	45.9	2.05	155.6	-0.3
4	657.7	42.1	1.89	120.5	2.3
5	663.2	46.8	1.87	131.7	1.2
6	645.0	51.4	1.92	152.8	2.3
7	655.7	41.8	1.89	120.3	2.7
8	620.1	45.3	2.00	145.8	0.8
9	623.5	45.2	1.99	144.1	0.6
10	650.3	40.6	1.91	118.8	2.8
11	651.9	42.3	1.90	123.3	2.8
12	641.5	42.1	1.93	126.8	4.5
13	668.1	46.6	1.86	129.3	-0.2
14	670.7	41.8	1.85	115.0	4.4
15	685.4	47.1	1.81	124.1	1.1
	avarage		**SD**		**avarage**
WL_max	**651.6**	**+/-**	**21.93**		**1.6**
FWHM	**129.5**	**+/-**	**14.16**		**1.7**

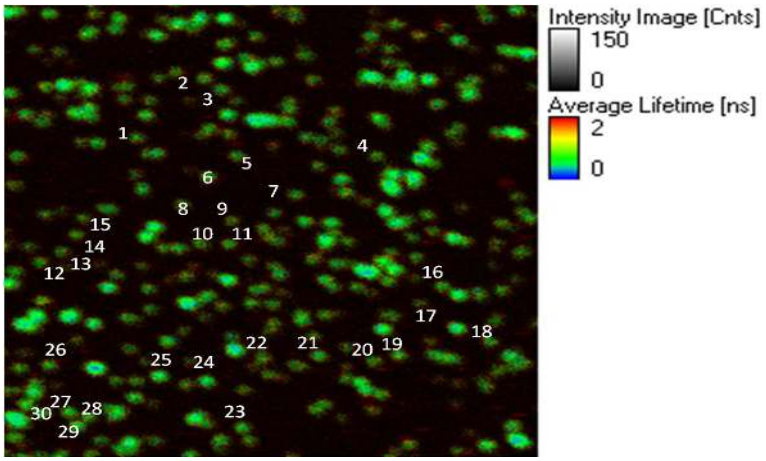

Figure B.1 Scanning confocal image of glass immobilized single gold nanorods excited at 480 nm in PBS

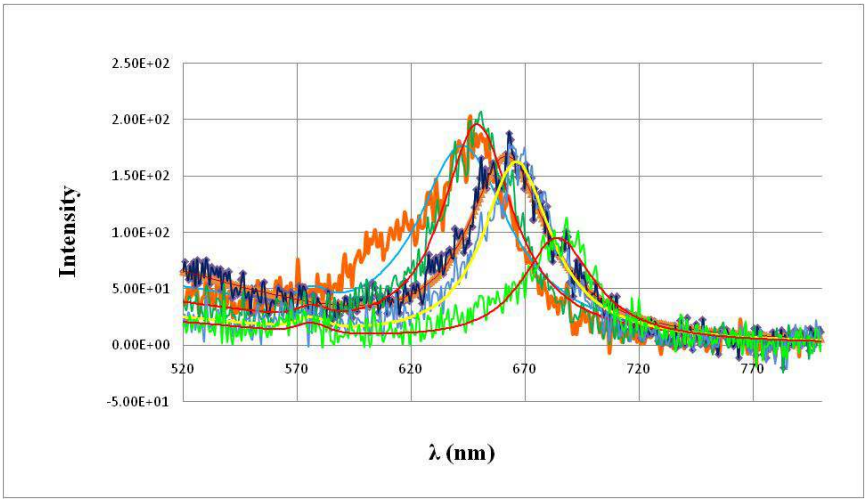

Figure B.2 Lorentzian fitting function to calculate the LSPR of glass immobilized single gold nanorods in PBS (5 particles)

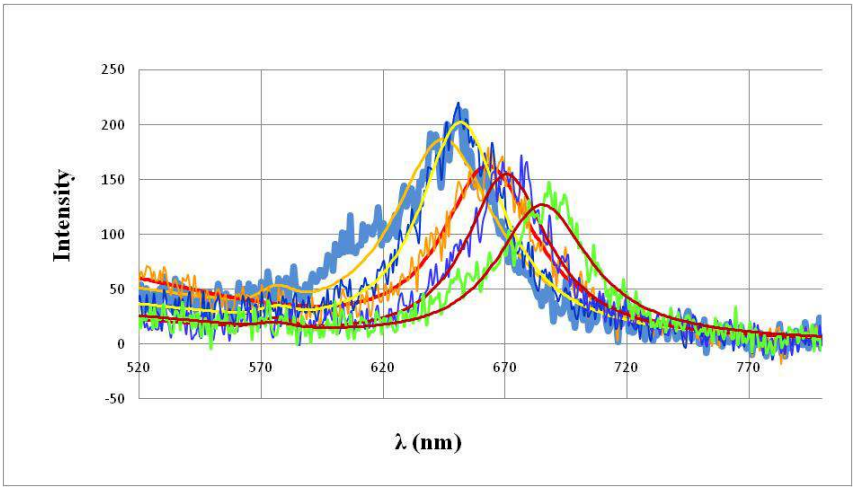

Figure B.3 Lorentzian fitting function to calculate the LSPR of single gold nanorods after Functinalization with complex Double Strand Dengue Virus DNA and TMPyP (5 particles)

3.2 Top Fluorescence Enhancement Factor and Fluorescence Enhanced Figure of Merit of Complex-ds-Dengue_2-TMPyP solution (100 nM) functionalized single GNRs in TMPyP solution and their plasmonic resonance wavelength have shown in Table B.14

B.14

Particles No.	max_counts	size_max_burst (max.counts)-(Average+2*sigma)	Top Enhanc. Factor (Siz.max.burst)/(A)	Fluor. Enhanc. Figure of Merit (Top Enhancement Factor)/(B)	λ max
1	49	29	36250	1812.5	672.8
2	52	22.7	28375	1418.75	663.9
3	64	46.6	58250	2912.5	658.4
4	61	39	48750	2437.5	642.4
5	43	25.3	31625	1581.25	655.9
6	78	66.2	82750	4137.5	649.6
7	115	92.3	115375	5768.75	650.2
8	36	10.5	13125	656.25	638.0
9	47	28.7	35875	1793.75	671.5
10	126	100.9	126125	6306.25	557.0
11	71	39.7	49625	2481.25	643.2
12	72	32.3	40375	2018.75	681.7
13	148	110.9	138625	6931.25	671.8
14	62	37.6	47000	2350	671.1
15	110	77.5	96875	4843.75	656.9
16	72	47.2	59000	2950	665.3
17	34	6.6	8250	412.5	590.5
18	72	50.5	63125	3156.25	654.7
19	95	65.4	81750	4087.5	671.9
20	49	15.6	19500	975	611.2
21	68	51.7	64625	3231.25	658.5
22	160	132.8	166000	8300	600.6
		Average of Top Enhancement	**6.41E+04**	**3.21E+03**	
		STDEV	**4.11E+04**	**2.05E+03**	

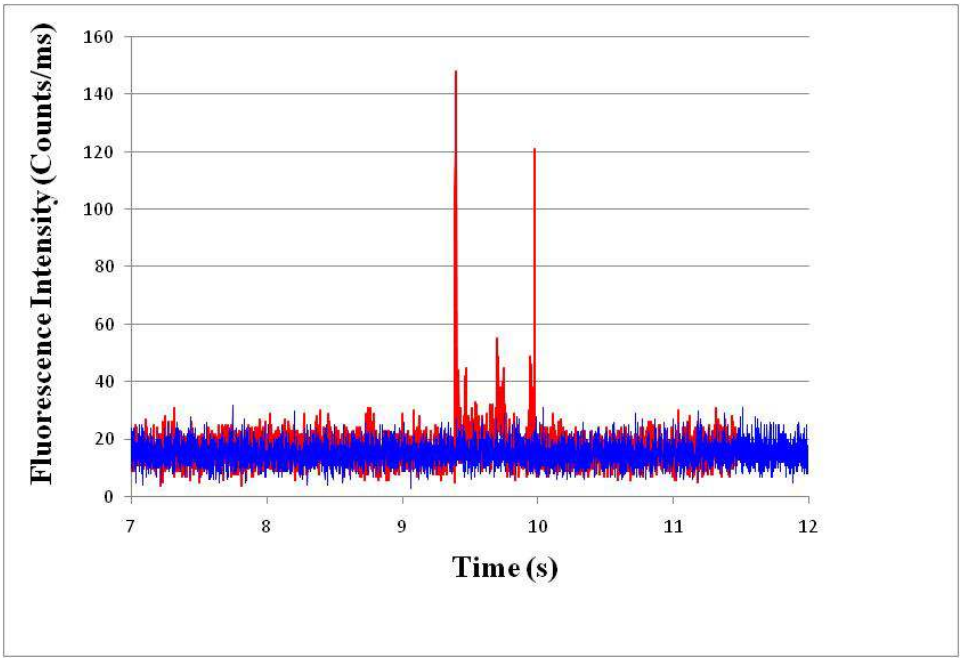

Figure B.4 Top Fluorescence enhanced (fluorescence burst) with maximum counts of 155 photons after (red) and before (blue) Complex ds-Denv2-TMPyP functionalization of single gold nano particles

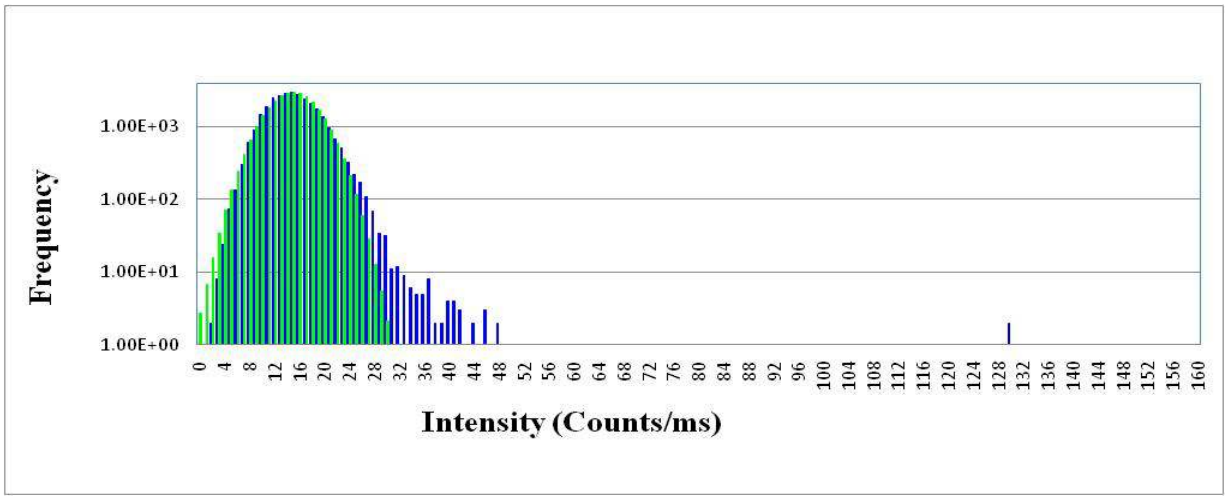

Figure B.5 Gaussian fitting graph of single gold nanorod-TMPyP system (green graph), Complex ds-Denv2-TMPyP functionalized single gold nano particles (blue graph)

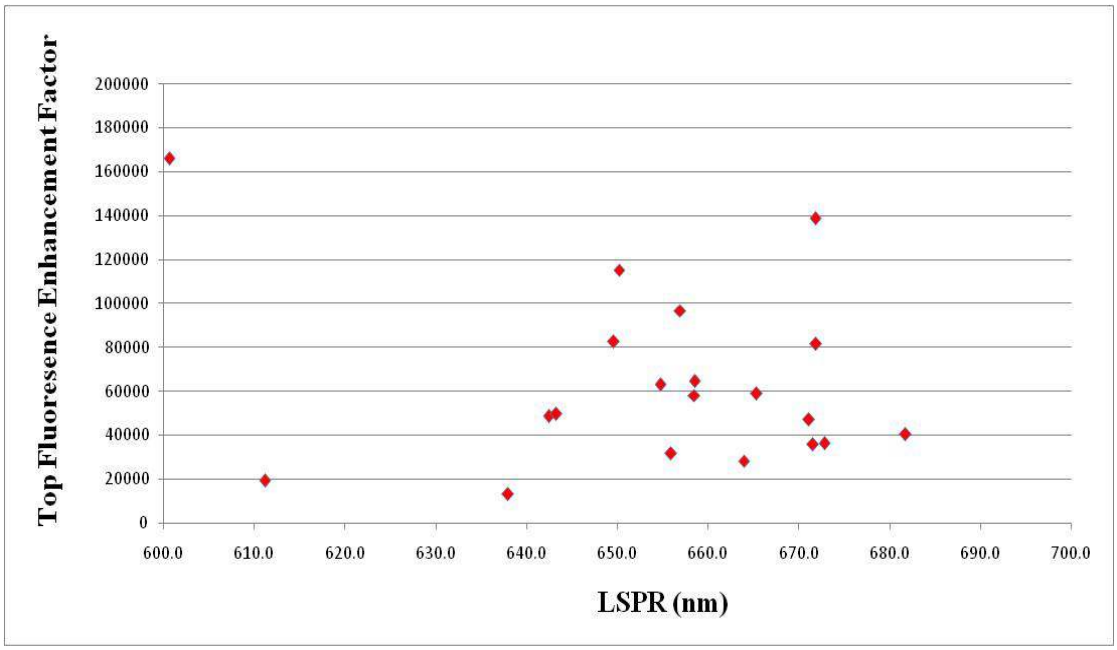

Figure B.6 Top Fluorescence Enhancement Factor of Complex ds-Denv2-TMPyP functionalized single gold nano particles versus their plasmonic resonance wavelength

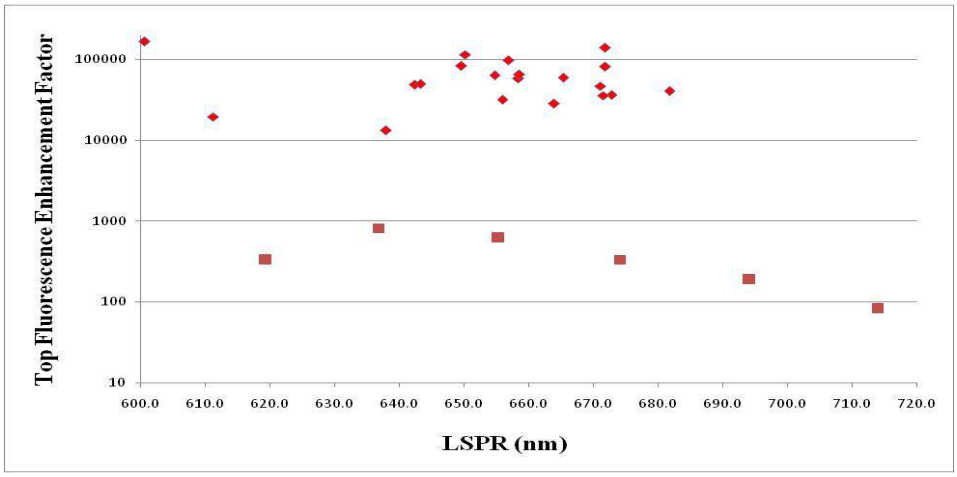

Figure B.7 The large fluorescence enhancement of Complex ds-Denv2-TMPyP functionalized single gold nano particles are two orders of magnitude larger than the calculated highest enhanced fluorescence expected for single GNR-TMPyP molecule.

Table B.15 Life time decay of Complex ds-Denv2-TMPyP functionalized single gold nanorods with TMPyP

Biosensor	Life Time 1 (Percentage)	Life Time 2 (Percentage)	Life Time 3 (Percentage)
Complex-ds-DNA-TMPyP Functionalized Single GNRs	7.8 ns (36.4%)	0.061 ns (48.8%)	1.525 ns (14.8%)

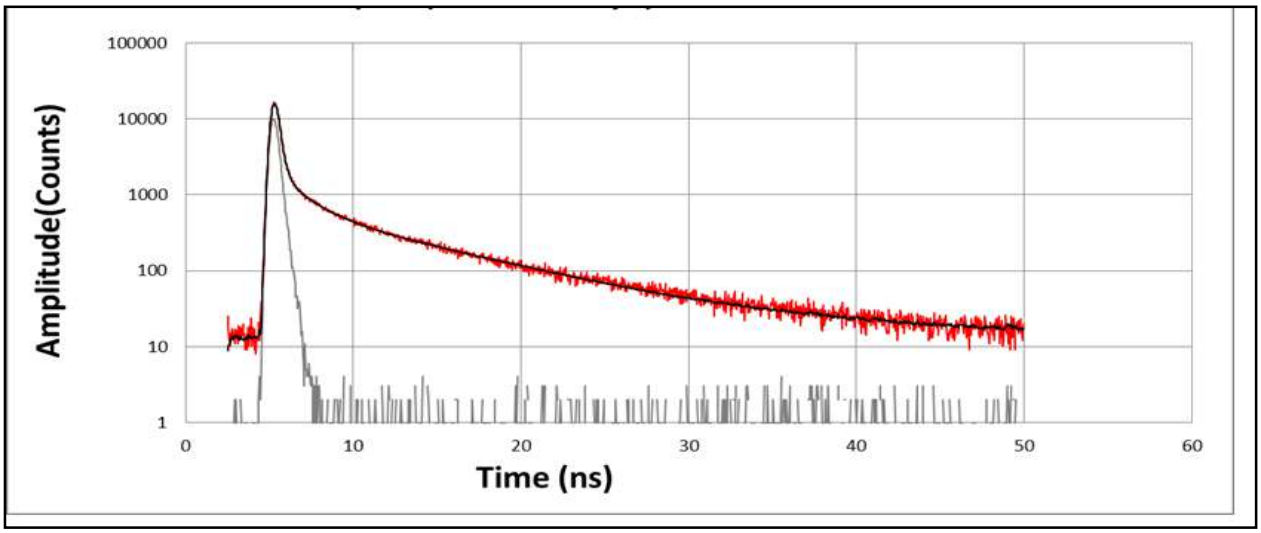

Figure B.8 TCSPC histogram of Life time decay of complex ds-Denv2-TMPyP Functionalized Single gold nanoparticles

3.3 Photluminescence Intensity single GNRs at laser excitation wavelength 480 nm and 640 nm (Table B.16)

B.16

Particles No.	Top Fluorescence Enhancement Factor	λ max	Photoluminesence Inensity λ Excitation =480nm	Photoluminesence Inensity λ Excitation =640nm
1	36250	672.8	94	58
2	28375	663.9	75.5	87.0
3	58250	658.4	67	38.0
4	48750	642.4	82	43.0
5	31625	655.9	78	28.0
6	82750	649.6	67	50.0
7	115375	650.2		
8	13125	638.0	60	44.0
9	35875	671.5		83.0
10	126125	557.0	86	95
11	49625	643.2		
12	40375	681.7	90	101.0
13	138625	671.8	100	95
14	47000	671.1		103
15	96875	656.9	79	68
16	59000	665.3	90	86
17	8250	590.5	41	69
18	63125	654.7	90	118
19	81750	671.9	102	119
20	19500	611.2	92	37
21	64625	658.5	84.5	119
22	166000	600.6	114	
	Average		**82.9**	**75.8**
	STDEV		**16.5**	**29.3**

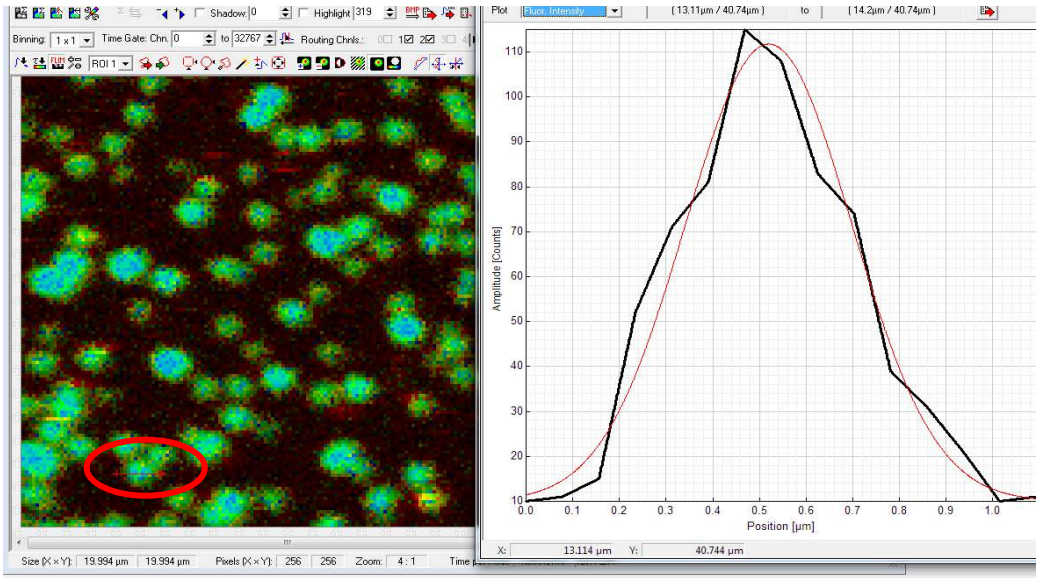

Figure B.9 Photoluminescence intensity of glass immobilized single gold nanorod at laser excitation wavelength of 480 nm

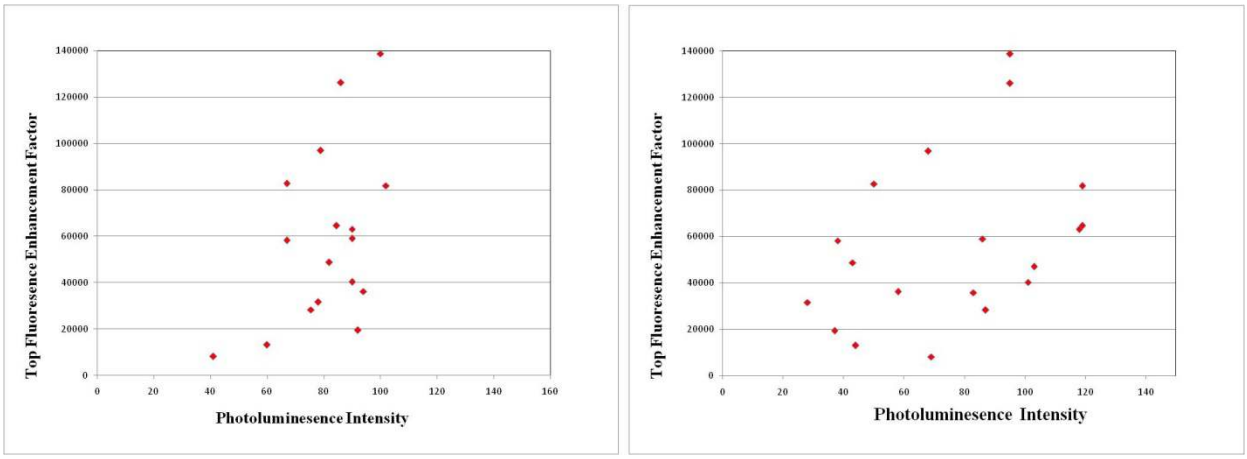

Figure B.10 Top fluorescence enhancement factor versus the photoluminescence intensity of single gold nanorods excited at 480 nm (left graph) and excited at 640 nm (right graph.

4 AUT functionalized single gold naorods-TPPS

4.1 The LSPR and FWHM of the glass immobilized gold nanoparticles excited at laser wavelength of 480 nm in PBS (Table B.17) and after functionalization with AUT in PBS solution (100 nM) (Table B.18)

B.17

Data file:	WL_max (nm)	FWHM	WL_max (meV)	FWHM
1	653.0	38.8	1.9	112.7
2	631.2	37.3	2.0	115.9
3	652.4	40.3	1.9	117.2
4	668.6	40.4	1.9	112.0
5	648.5	38.1	1.9	112.2
6	611.6	38.0	2.0	126.0
7	678.0	40.4	1.8	108.9
8	626.4	38.4	2.0	121.1
9	638.0	35.3	1.9	107.4
10	629.2	37.3	2.0	116.7
11	659.0	44.6	1.9	127.2
12	615.2	37.6	2.0	123.1
13	619.9	39.4	2.0	127.0
14	646.6	38.6	1.9	114.2
15	663.1	40.4	1.9	113.7
16	684.3	40.2	1.8	106.2
17	652.5	40.0	1.9	116.3
18	639.6	38.9	1.9	117.7
19	648.1	37.9	1.9	111.7
20	655.7	39.7	1.9	114.2
21	645.5	38.9	1.9	115.6
22	657.7	39.5	1.9	113.2
23	626.6	35.8	2.0	112.9
24	636.5	36.6	1.9	112.0
25	677.3	42.6	1.8	115.1
26	634.1	39.2	2.0	120.7
27	661.1	40.9	1.9	116.0
28	670.2	40.6	1.9	112.0
29	654.6	33.1	1.9	95.8
30	686.4	40.8	1.8	107.3
	averages		SD	
WL_max	649.0	+/-	19.8	
FWHM	114.5	+/-	6.5	

B.18

Data file:	WL_max (nm)	FWHM	WL_max (meV)	FWHM	ΔWL_max (AUT-PBS)
1	655.5	42.8	1.9	123.3	2.5
2	634.9	40.4	2.0	124.0	3.7
3	656.7	40.9	1.9	117.5	4.3
4	672.6	43.4	1.8	118.8	4.0
5	651.2	40.3	1.9	117.6	2.7
6	615.0	38.7	2.0	126.8	3.4
7	680.9	41.9	1.8	112.0	2.9
8	629.7	42.2	2.0	131.7	3.3
9	642.3	37.5	1.9	112.6	4.2
10	632.7	42.7	2.0	132.2	3.5
11	663.2	47.1	1.9	132.8	4.2
12	617.4	39.3	2.0	127.8	2.2
13	623.1	42.8	2.0	136.6	3.3
14	651.9	40.9	1.9	119.2	5.3
15	667.2	42.2	1.9	117.3	4.1
16	688.8	41.2	1.8	107.7	4.5
17	657.8	41.0	1.9	117.4	5.3
18	643.6	42.1	1.9	125.9	4.1
19	651.9	40.4	1.9	117.8	3.8
20	660.2	43.1	1.9	122.5	4.5
21	649.8	40.8	1.9	119.7	4.3
22	661.1	40.1	1.9	113.7	3.4
23	629.8	38.9	2.0	121.6	3.1
24	640.8	37.4	1.9	112.8	4.2
25	680.7	43.7	1.8	116.9	3.4
26	637.6	42.7	1.9	130.0	3.4
27	664.8	41.3	1.9	115.8	3.7
28	673.6	42.4	1.8	115.7	3.4
29	655.7	39.5	1.9	113.9	1.1
30	687.2	42.5	1.8	111.4	0.8
	averages				**averages**
WL_max	652.6	+/-	19.9		**3.6**
FWHM	120.4	+/-	7.3		**1.0**

4.2 Top Fluorescence Enhancement Factor and Fluorescence Enhanced Figure of Merit of ds-AUT functionalized single GNRs in TPPS solution (10 nM) and their Plasmonic resonance wavelength have shown in Table B.19.

B.19

Particles No.	max_counts	size_max_burst (max.counts)-(Average+2*sigma)	Top Enhanc. Factor (Siz.max.burst)/(A)	Fluor. Enhanc. Figure of Merit (Top Enhancement Factor)/(B)	λ max
1	25	8.8	3271.4	327.1	655.5
4	28	10.2	3791.8	379.2	672.6
7	21	9	3345.7	334.6	680.9
9	9	2.4	892.2	89.2	642.3
10	21	12	4461.0	446.1	632.7
17	27	11.2	4163.6	416.4	657.8
18	20	10	3717.5	371.7	643.6
22	16	7.8	2899.6	290.0	661.1
23	15	10.4	3866.2	386.6	629.8
26	48	37.6	13977.7	1397.8	637.6
27	30	11.4	4237.9	423.8	664.8
28	17	7.8	2899.6	290.0	673.6
29	16	7.1	2639.4	263.9	655.7
30	21	6.6	2453.5	245.4	687.2
		Average	**4.04E+03**	**4.04E+02**	**656.8**
		SD	**2.89E+03**	**2.89E+02**	**17.3**

4.3 Top Fluorescence Enhancement Factor and Fluorescence Enhanced Figure of Merit of ds-AUT functionalized single GNRs in TPPS solution (100 nM) and their Plasmonic resonance wavelength have shown in Table B.20.

B.20

Particles No.	max_counts	size_max_burst (max.counts)-(Average+2*sigma)	Top Enhanc. Factor (Siz.max.burst)/(A)	Fluor. Enhanc. Figure of Merit (Top Enhancement Factor)/(B)	λ max
1	40	24.1	8959.1	895.9	655.5
4	50	28.4	10557.6	1055.8	672.6
7	32	17.4	6468.4	646.8	680.9
9	22	14.12	5249.1	524.9	642.3
10	23	12.5	4646.8	464.7	632.7
12	34	28.9	10743.5	1074.3	617.4
17	107	89.6	33308.6	3330.9	657.8
18	45	32.7	12156.1	1215.6	643.6
26	28	15.9	5910.8	591.1	637.6
27	48	27.9	10371.7	1037.2	664.8
28	53	42.6	15836.4	1583.6	673.6
22	23	12.5	4646.8	464.7	661.1
23	33	18.1	6728.6	672.9	629.8
29	43	33.2	12342.0	1234.2	655.7
30	27	11.4	4237.9	423.8	687.2
		Average	**1.01E+04**	**1.01E+03**	**654.2**
		SD	**7.03E+03**	**7.03E+02**	**19.4**

4.4 Photluminescence Intensity single GNRs in at laser excitation wavelength 480 nm and 640 nm (Table B.21)

B.21

Particles No.	Fluor. Enhanc. Figure of Merit (Top Enhancement Factor)/(B)	λ max	Photoluminesence Inensity λ Excitation =480 nm	Photoluminesence Inensity λ Excitation =640 nm
1	8959.1	655.5	65	58
4	10557.6	672.6	94	63
7	6468.4	680.9	82	39
9	5249.1	642.3	53	15
10	4646.8	632.7	65	25
12	10743.5	617.4	51	
17	33308.6	657.8	92	64
18	12156.1	643.6	68	30
26	5910.8	637.6	72	26
27	10371.7	664.8	89	65
28	15836.4	673.6	67	24
22	4646.8	661.1	58	34
23	6728.6	629.8	50.5	
29	12342.0	655.7	72	28
30	4237.9	687.2		54
	1.01E+04	**Average**	**69.9**	**40.4**
	7.03E+03	**SD**	**14.2**	**17.2**

5. Calculation of maximum fluorescence enhancement of TMPyP-GNR

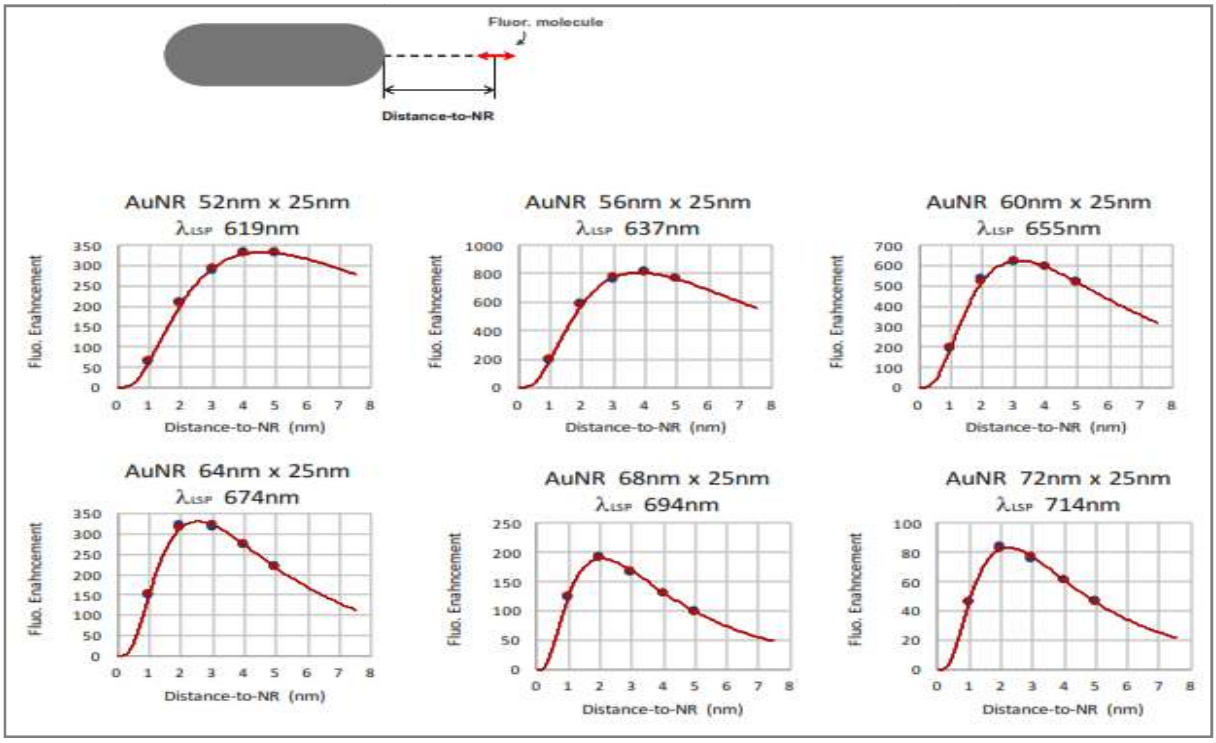

Figure B.11 The calculated maximum fluorescence enhancement of TMPyP molecule as a dipole at optimum distance in tip area of single gold nanords with different length and different LSPR

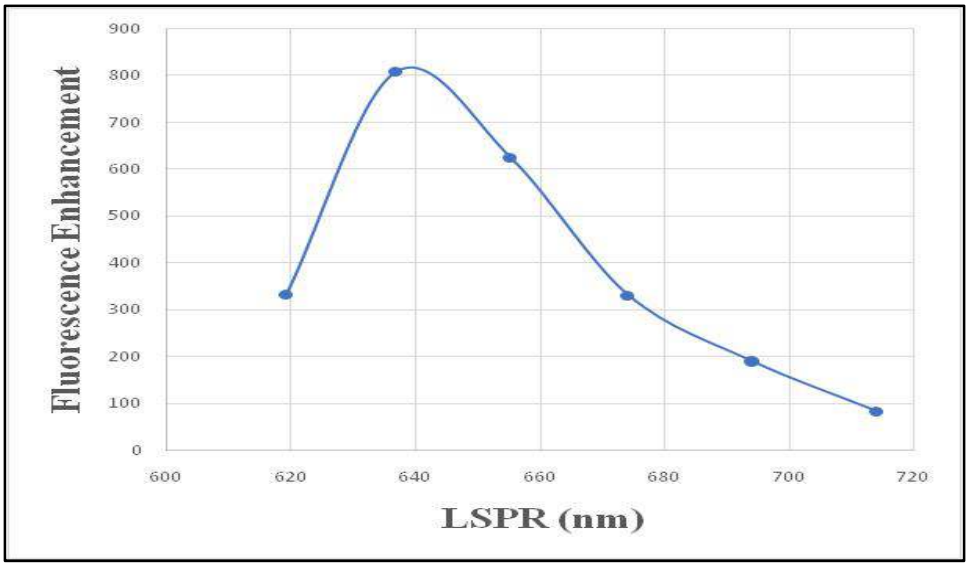

Figure B.12 The calculated maximum fluorescence enhancement for single gold nanorods-TMPyP system versus the LSPR wavelength based DDA simulation